

ATOMS: ALMA Three-millimeter Observations of Massive Star-forming regions – X. Chemical differentiation among the massive cores in G9.62+0.19

Yaping Peng,^{1,2*} Tie Liu,^{3†} Sheng-Li Qin,² Tapas Baug,⁴ Hong-Li Liu,² Ke Wang,⁵ Guido Garay,⁶ Chao Zhang,⁷ Long-Fei Chen,⁸ Chang Won Lee,^{9,10} Mika Juvela,¹¹ Dalei Li,¹² Ken’ichi Tatematsu,¹³ Xun-Chuan Liu,³ Jeong-Eun Lee,¹⁴ Gan Luo,¹⁵ Lokesh Dewangan,¹⁶ Yue-Fang Wu,¹⁷ Li Zhang,² Leonardo Bronfman,⁶ Jixing Ge,¹⁸ Mengyao Tang,^{2,19} Yong Zhang,^{20,21,22} Feng-Wei Xu,¹⁷ Yao Wang,²³ and Bing Zhou^{1,2}

Affiliations are listed at the end of the paper

Accepted XXX. Received YYY; in original form ZZZ

ABSTRACT

Investigating the physical and chemical structures of massive star-forming regions is critical for understanding the formation and the early evolution of massive stars. We performed a detailed line survey toward six dense cores named as MM1, MM4, MM6, MM7, MM8, and MM11 in G9.62+0.19 star-forming region resolved in ALMA band 3 observations. Toward these cores, about 172 transitions have been identified and attributed to 16 species including organic Oxygen-, Nitrogen-, Sulfur-bearing molecules and their isotopologues. Four dense cores MM7, MM8, MM4, and MM11 are line rich sources. Modeling of these spectral lines reveals the rotational temperature in a range of 72–115 K, 100–163 K, 102–204 K, and 84–123 K for the MM7, MM8, MM4, and MM11, respectively. The molecular column densities are $1.6 \times 10^{15} – 9.2 \times 10^{17}$ cm⁻² toward the four cores. The cores MM8 and MM4 show chemical difference between Oxygen- and Nitrogen-bearing species, i.e., MM4 is rich in oxygen-bearing molecules while nitrogen-bearing molecules especially vibrationally excited HC₃N lines are mainly observed in MM8. The distinct initial temperature at accretion phase may lead to this N/O differentiation. Through analyzing column densities and spatial distributions of O-bearing Complex Organic Molecules (COMs), we found that C₂H₅OH and CH₃OCH₃ might have a common precursor, CH₃OH. CH₃OCHO and CH₃OCH₃ are likely chemically linked. In addition, the observed variation in HC₃N and HC₅N emission may indicate that their different formation mechanism at hot and cold regions.

Key words: ISM:abundances – ISM:individual (G9.62+0.19) – ISM:molecules – radio lines:ISM – star:formation

1 INTRODUCTION

High-mass stars play a major role in the evolution of the galaxies. They affect the formation and evolution of planets, stars, and galaxies (Kennicutt 1998; Bally et al. 2005). But the formation process of high-mass star remains much less understood because of their comparatively larger distances and shorter lifetimes than low-mass star. In addition, high-mass stars are usually born in complicated cluster environments. The process of star formation will inevitably be influenced by nearby protostars (Krumholz et al. 2014), which complicates the physical and chemical structures of high-mass star formation. During the earliest phases high-mass stars remain embedded in their natal molecular clouds. Observationally, their embedded phases can generally be subdivided into four different evolutionary stages: massive dense cores (including starless cores), high-mass protostellar objects (HMPOs), hot molecular cores (HMCs), and Hyper/ultra compact H_{II} regions (H/UC H_{II}) (e.g., Kurtz et al. 2000; Hoare et al. 2007; Beltrán et al. 2009; Tan et al. 2013; Liu et

al. 2021). Investigating the physical and chemical properties of high-mass star forming cores at different evolutionary stages is important for understanding the formation and early evolution of massive stars.

G9.62+0.19 is a well known high-mass star forming region at a distance of 5.2 kpc (Sanna et al. 2009), which hosts several massive cores at different evolutionary phases (e.g., Testi et al. 1998; Hofner et al. 1994, 2001; Liu et al. 2017). Multi-wavelength VLA observations identified nine radio continuum sources (denoted as A–I) in this region (Garay et al. 1993; Testi et al. 2000). The extended H_{II} region “A”, cometary-shaped H_{II} region “B” and compact H_{II} region “C” are three evolved H_{II} regions (Kurtz et al. 1994). The JCMT/SCUBA 450 μm observations found that new generations of high-mass young stellar objects (“G9.62 clump”) are forming in the region which is located to the east of the evolved H_{II} regions (Liu et al. 2011, 2017). Twelve dense cores (MM1-MM12) have been identified in this clump through 1.3 mm observations with ALMA (Liu et al. 2017). Recent ALMA observations at 1 mm wavelength (band 7) with higher resolution further resolved “G9.62 clump” into 23 dense cores (Dall’Olio et al. 2019). Among of them, MM4, MM7, MM8, and MM11 are associated with radio sources “E”, “G”, “F”, and “D”, respectively. Five cores (MM4/E, MM6, MM7/G, MM8/F

* E-mail: pyp893@163.com

† E-mail: liutie@shao.ac.cn

and MM11/D) are considered as high-mass protostars. Based on observations of CH_3OH $v_t = 1$ line and the existence of the outflow, Liu et al. (2017) further classified their evolutionary sequence as following: MM6 (HMPO), MM7 (early HMC), MM8 (HMC), MM4 (late HMC or HC HII), and MM11 (UC HII). Presence of collimated SiO (5-4) and CO (2-1) outflows and absence of CH_3OH $v_t = 1$ emission in MM6 are indicative of it to be at HMPO stage. MM7 and MM8 are associated with centimeter continuum emission (Testi et al. 2000), outflows, and strong CH_3OH $v_t = 1$ line emission, and are thus at comparatively more evolved stage than MM6. CH_3OCHO $v_t = 1$ was detected toward the MM8 while not for MM7, indicating that MM8 is hotter and older than MM7. MM4 has centimeter continuum counterpart (Testi et al. 2000), while no outflows implying MM4 to be at a more evolved phase. Weaker CH_3OH $v_t = 1$ emission toward MM11 than MM4 suggest that MM11 should be at a more evolved phase, since the abundance of CH_3OH should be close to maximum at hot core stage and decrease in the UC HII phase (Gerner et al. 2014). The other seven cores (MM1, MM2, MM3, MM5, MM9, MM10, and MM12) are considered to be starless core as they do not show any signature of outflows. They only show the signature of rare interstellar molecules, especially complex organic molecules (COMs). Su et al. (2005) reported that many molecular lines including Nitrogen-bearing molecules and organic molecules have been detected toward the source F(MM8) and E(MM4) in G9.62+0.19 by Submillimeter Array (SMA) observations (345 GHz). In general, G9.62+0.19 contains different evolutionary types of dense cores, and harbours rich chemistry indicating that it is an ideal object to explore the distinct chemical properties of cores at different evolutionary stages.

Interstellar molecules especially the COMs are useful diagnosis to study the interstellar environments and evolutionary stages of various astronomical sources since they usually exist in special physical environments. COMs have been detected in warm regions including hot cores in high-mass star-forming regions such as SgrB2(N) (e.g., Belloche et al. 2013, 2016, 2017; Bonfand et al. 2019), G31.41+0.31 (e.g., Rivilla et al. 2017b; Mininni et al. 2020; Colzi et al. 2021), AFGL 4176 (Bøgelund et al. 2019), NGC 6334I (e.g., Zernickel et al. 2012; Bøgelund et al. 2018; Ligterink et al. 2020), W51 e2 (Remijan et al. 2004a; Rivilla et al. 2017a), G34.3+0.2 (Lykke et al. 2015), Orion KL (e.g., Crockett et al. 2014; Cernicharo et al. 2016; Tercero et al. 2018), G331.512-0.103 (Hervías-Caimapo et al. 2019; Duronea et al. 2019) and hot corinos in low-mass star-forming regions such as NGC 1333-IRAS 2A and -IRAS 4A (Taquet et al. 2015), IRAS 16293-2422 (Jørgensen et al. 2012; Richard et al. 2013), and in cold environments such as dark clouds (TMC-1 (e.g., McGuire et al. 2018; Agúndez et al. 2021) and L134N (Dickens et al. 2000)), starless cores (e.g., Bacmann et al. 2012; Vastel et al. 2014; Jiménez-Serra et al. 2016; Molet et al. 2019), and cold outer envelopes of protostars (e.g., Öberg et al. 2010; Bergner et al. 2017), Galactic Center molecular clouds such as G-0.02-0.07, G-0.11-0.08, and G+0.693-0.027 (Requena-Torres et al. 2006, 2008; Zeng et al. 2018; Rodríguez-Almeida et al. 2021), and the disk of an outbursting young star, V883 Ori (Lee et al. 2019). The chemistry in different interstellar environments, and the formation of COMs in these environments are complex and long-standing quest that has been explored by many researches in the past several years (e.g., Herbst & van Dishoeck 2009; Laas et al. 2011; Bacmann et al. 2012; Woods et al. 2013; Vasyunin & Herbst. 2013; Ruaud et al. 2015; Abplanalp et al. 2016; Skouteris et al. 2018; Shingledecker et al. 2019). Yet, there remain huge challenges for revealing a clearer picture of COMs formation. Fundamentally, the chemistry is the result of interactions of different physical and chemical parameters that are tangled with each other, with the former includes but not limited to the tempera-

ture, density and evolutionary stages of the cores, and the later primarily depends on the elemental content, grain mantle compositions and reaction network that represents the chemical contents of the cores. Thus, when the physical properties of the core are well constrained, the observational results, such as the column density and abundance of individual molecule and the correlations between different molecules, could be used to retrieve the intrinsic chemical properties.

Here we preform a detailed analysis of the physical and chemical conditions (e.g., temperature, density, and possible chemical formation routes of COMs) of dense cores in G9.62+0.19 through ALMA band 3 observations. The paper is organized as follows. In Sect. 2 we describe the observations and the data reduction. The results for continuum and line survey are presented in Sect. 3. We model the spectral lines and calculate the parameters under the LTE assumption in Sect. 4. A general discussion about properties of each core and chemical differentiation among these cores is presented in Sect. 5. In Sect. 6 we give our summary, with a possibility of future investigations of massive star formation at different evolutionary stages.

2 OBSERVATIONS

G9.62+0.19 was observed with ALMA in band 3 (Project ID: 2019.1.00685.S; PI: Tie Liu), as part of the ATOMS survey, which was conducted towards 146 IRAS clumps (Liu et al. 2020a,b, 2021). The Atacama Compact 7-m Array (ACA) observations of G9.62+0.19 were conducted on 1st and 13th October, 2019 with two executions, and the 12-m array observations were conducted on 31th October, 2019. The phase center in both ACA and 12-m array observations is R.A.(J2000)= $18^{\text{h}}06^{\text{m}}14^{\text{s}}.99$ and Decl.(J2000)= $-20^{\circ}31'35''.4$. The spectral windows (SPWs) 1–6 at the lower sideband have a bandwidth of 58.59 MHz, which cover dense gas tracers such as J=1-0 transition of HCO^+ , H^{13}CO^+ , HCN , and H^{13}CN , shock tracer SiO J=2-1 and photodissociation region tracer CCH J=1-0. The other two wide SPWs 7–8 at the upper sideband covering frequency range of 97.530–101.341 GHz, each with a bandwidth of 1875 MHz, which are used for continuum emission and line survey. The spectral resolution is $\sim 0.2 \text{ km s}^{-1}$, $\sim 0.1 \text{ km s}^{-1}$, and $\sim 1.5 \text{ km s}^{-1}$ for SPWs 1–4, SPWs 5–6, and SPWs 7–8, respectively (Liu et al. 2021).

The calibrated UV data and images were processed using the Common Astronomy Software Applications (CASA). All images are primary beam corrected. The calibration uncertainty on the flux density is $\sim 10\%$. Continuum image was constructed from line-free channels. The synthesized beam size and 1σ rms noise level for the continuum image from the 12-m array are $1.56'' \times 1.38''$ ($\sim 8112 \times 7176$ au at a distance of 5.2 kpc, P.A.= 87.62°) and $0.4 \text{ mJy beam}^{-1}$, respectively. For spectral images, their synthesized beam size is approximately $1.9'' \times 1.7''$ ($\sim 9880 \times 8840$ au) at the lower band (SPWs 1–6), and $\sim 1.6'' \times 1.4''$ ($\sim 8320 \times 7280$ au) at the upper band (SPWs 7–8). The 1σ rms noise is about 8 mJy beam^{-1} per channel, 10 mJy beam^{-1} per channel, and 3 mJy beam^{-1} per channel for SPWs 1–4, 5–6, and 7–8, respectively. The 12-m+ACA combined continuum image of G9.62+0.19 has a beam size of $2.3'' \times 1.7''$ (P.A.= 85.14°), and a sensitivity of $\sim 0.5 \text{ mJy beam}^{-1}$. For spectral lines, combined SiO (2-1), HCO^+ (1-0) and CS (2-1) are utilized to probe the kinematics of this source. The synthesized beams for SiO , HCO^+ , and CS are $2.7'' \times 2.1''$, $2.5'' \times 1.9''$, and $2.3'' \times 1.7''$, respectively, and the sensitivity levels are ~ 13 , 60, and 48 mJy beam^{-1} per channel, respectively.

3 RESULTS

3.1 ALMA 3 mm continuum emission

Figure 1 shows the 3 mm continuum emission of G9.62+0.19 observed by the 12-m array alone and 12-m+ACA combined data. Six dense cores (MM1, MM4, MM6, MM7, MM8, and MM11) that have been previously observed by 1.3 mm continuum emission with higher angular resolution ($0.94'' \times 0.71''$) (Liu et al. 2017) in G9.62 clump are also resolved in our 3 mm data. The positions of MM2, MM3, MM5, MM9, and MM10 are marked in Figure 1. However, these cores are not resolved in 3 mm map possibly because of the relatively lower spatial resolution of our observations. The expanding cometary-like H α region "B" is observed to the west of the G9.62 clump (see Figure 2). The positions, sizes, peak flux density (I_{peak}) and total flux density (S_{ν}) of six dense cores obtained by two dimensional Gaussian fitting are listed in Table 1. We found that the size, I_{peak} and S_{ν} of each core observed from combined data are larger than those from 12-m observations alone, since 12-m array observations are affected by missing flux, then extended emission is not sampled completely. The observations of 12-m array missed $\sim 5\%$ of extended emissions compared to the observations of 12-m + ACA combined data. More information on continuum emission also can be found in Liu et al. (2020a).

3.2 Molecular lines identification

We identified spectral line transitions using the eXtended CASA Line Analysis Software Suite (XCCLASS¹; Möller et al. 2017). The molecular spectroscopic parameters in XCCLASS are obtained from Cologne Database for Molecular Spectroscopy (CDMS²; Müller et al. 2001, 2005) and Jet Propulsion Laboratory (JPL³; Pickett et al. 1998) molecular databases. The software includes myXCCLASS program, which is used to model data by solving the radiative transfer equation. Under the assumption of local thermodynamical equilibrium (LTE), XCCLASS takes the beam dilution, dust attenuation, the line opacity, and line blending into account (Möller et al. 2017). A few constraints are set for proper identification of the molecular species. The rest frequency must be consistent with the value from laboratory measurement; for a certain species, all detected transitions from the same source must have a similar LSR velocity; and transitions for a specific species should have similar spatial distribution owing to that they are excited by similar conditions (Peng et al. 2017). Furthermore, all lines above the 3σ "detection level" are available in our identification and follow-up analyses. The spectrum from 12-m array observations are used for line identification and following data modeling. In the Appendix A, we make a comparison between 12-m array and combined data, suggesting there is no difference when using them to study the hot core chemistry.

3.2.1 Molecular lines from different cores

We identified 16 species toward 6 dense cores of G9.62+0.19. Since each of the dense core is at different evolutionary stage, the emission of molecules have diverse characteristics in species and intensity. Figure 3 presents the species and transition numbers in each core. Figure 4 and Figure B1 display the full-band beam-averaged spectra at the six continuum peaks. Transitions with intensity higher than 3σ

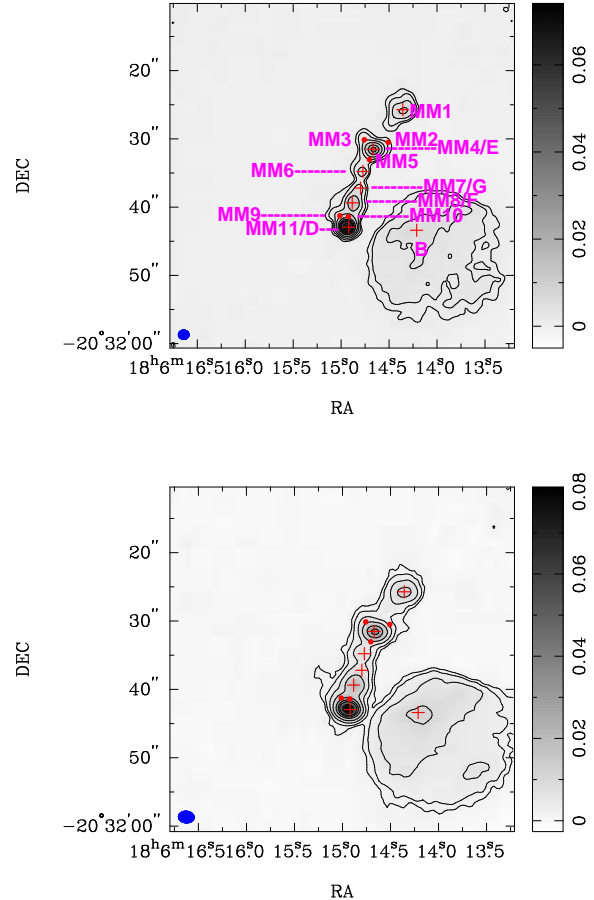


Figure 1. Upper panel: the 3 mm continuum emission of G9.62+0.19 from 12-m array observations. Lower panel: the 3 mm continuum emission of G9.62+0.19 from 12-m+ACA combined observations. The synthesized beam size is shown in the bottom left corner. The contour levels are $(3, 5, 10, 20, 40, 60, 80, 100, 140, 180) \times 0.4 \text{ mJy beam}^{-1}$, and $(3, 5, 10, 20, 40, 60, 80, 120, 140) \times 0.5 \text{ mJy beam}^{-1}$ for 12-m and 12-m+ACA combined data, respectively. The cross symbols mark the 3 mm continuum peaks of MM1, MM4, MM6, MM7, MM8, MM11, and H α region "B". The filled circles indicate the 1.3 mm continuum peaks (MM2, MM3, MM5, MM9, and MM10) (Liu et al. 2017). The unit of the gray scale bar on the right is in Jy/beam.

are listed in Table B1. The rest frequencies, quantum numbers, the line strength (S_{μ}^2), and the upper-level energy (E_u) of each transitions are given in Columns 1 to 4 in the Table. Estimated 1σ RMS is 0.13 K, 0.12 K, 0.13 K, 0.14 K, 0.12 K, and 0.12 K for MM1, MM6, MM7, MM8, MM4, and MM11, respectively. The noise level σ in each spectrum is computed in line-free channels.

Below we discuss the line identification toward each core:

MM1: Simple molecular transitions CS J=2-1 and SO 3(2)-2(1), and a dense gas tracer HC₃N J=11-10 are detected in this region. The ionized gas tracer H₄₀ α line is also detected in this core.

MM4: This is a line-rich source, in which a number of molecules have been detected. Line identification results showed that O-bearing COMs (e.g., CH₃OH v=0, CH₃OH v_t=1, CH₃OCHO, CH₃OCHO v_t=1, CH₃OCH₃, CH₃COCH₃, and C₂H₅OH) are detected. The line strength of O-bearing COMs is higher toward the MM4 than the other cores. Additionally, a few lines of N-bearing

¹ <https://xclass.astro.uni-koeln.de>

² <http://cdms.de>

³ <http://spec.jpl.nasa.gov>

Table 1. Parameters of Continuum Sources

Name	R.A.(J2000)	Decl.(J2000)	12-m array			12-m and ACA combined data		
			size	I_{peak} (mJy beam $^{-1}$)	S_{ν} (mJy)	size	I_{peak} (mJy beam $^{-1}$)	S_{ν} (mJy)
MM1	18 ^h 06 ^m 14 ^s .357	-20°31'25".73	3.01" \times 2.09"	8.2 \pm 0.6	32.4 \pm 2.3	3.73" \times 2.54"	11.1 \pm 0.8	38.3 \pm 2.1
MM4	18 ^h 06 ^m 14 ^s .67	-20°31'31".52	1.32" \times 1.06"	25.2 \pm 1.9	41.4 \pm 2.1	1.97" \times 1.79"	30.1 \pm 2.0	56.9 \pm 5.3
MM6	18 ^h 06 ^m 14 ^s .772	-20°31'34".78	2.05" \times 0.88"	5.3 \pm 0.4	10.8 \pm 0.7	2.43" \times 1.95"	8.2 \pm 0.2	18.5 \pm 1.2
MM7 ^a	18 ^h 06 ^m 14 ^s .798	-20°31'37".21
MM8	18 ^h 06 ^m 14 ^s .884	-20°31'39".37	2.67" \times 1.23"	13.1 \pm 1.0	36.3 \pm 4.1	3.05" \times 1.58"	19.2 \pm 0.8	46.9 \pm 3.2
MM11	18 ^h 06 ^m 14 ^s .92	-20°31'42".95	1.05" \times 0.75"	71.4 \pm 3.7	99.1 \pm 4.3	1.40" \times 1.07"	77.5 \pm 3.3	109.7 \pm 4.6

^a The 2-D Gaussian fitting toward the MM7 suffered failed convergence due to this core is not well resolved by 3 mm continuum emission.

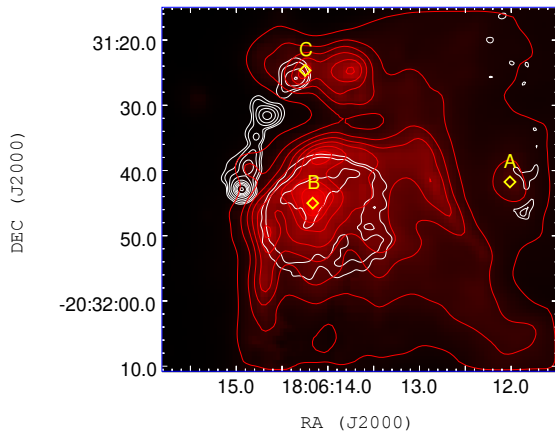


Figure 2. Three millimeter continuum emission (white contours) overlaid on 8 μm emission (red contours) with Spitzer/IRAC observation. The red contours are $(10\%, 20\%, 30\%, 40\%, 50\%, 60\%, 70\%, 80\%, 90\%, \text{ and } 100\%) \times 2648 \text{ MJy/sr}$. Three evolved HII regions A, B, and C are marked with yellow diamond shapes.

species (e.g., HC₃N $v_7=1$, HC₃N $v_7=2$, HC₅N, and C₂H₅CN) are detected toward MM4.

MM6: MM6 contains a few species such as H₂CO, CH₃OH with low E_u of 22 K, HC₃N $v=0$, CS, SO, and ³⁴SO, all of which cover only one transition. Other COMs are not detected.

MM7: O-bearing species containing H₂CO, H₂CCO, CH₃OH, CH₃OH $v_t=1$, CH₃CHO, CH₃OCHO, CH₃OCH₃, and C₂H₅OH, N-bearing molecules including HC₃N $v=0$ and its ¹³C isotopologues, HC₃N in vibrational states ($v_7=1$, $v_7=2$), HC₅N, C₂H₅CN, along with S-bearing species (CS, SO, ³⁴SO, SO₂) are identified in this core. CH₃OCHO $v_t=1$ is not excited toward this core.

MM8: MM8 is the richest in molecular species. Sixteen species are identified in this core including simple species such as H₂CO, CS, SO, and SO₂, N-, O-, and S-bearing COMs (e.g., CH₃OH, CH₃CHO, CH₃OCHO, CH₃OCH₃, CH₃COCH₃, C₂H₅OH, C₂H₅CN, and CH₃SH), with a few in torsionally excited state (CH₃OH $v_t=1$ and CH₃OCHO $v_t=1$). Cyanopolyyne species HC₃N in its vibrationally excited states $v_7=1$, $v_7=2$, $v_7=3$, and $v_6=1$ are observed in this core. We note that three transitions of HC₃N $v_7=3$ at 100.88044, 101.02780, and 101.16989 GHz are

blended with SO₂ at 100.87810 GHz, H₂CCO at 101.02447 GHz, and CH₃SH at 101.16830 GHz, respectively.

MM11: H_{40 α} , H_{50 β} and a few O-bearing COMs species such as CH₃OH, CH₃CHO, CH₃OCHO, CH₃OCH₃ and C₂H₅OH are detected toward this core. Cyanoacetylene and its ¹³C isotopologues in ground state and in vibrational state $v_7=1$ are also detected, while cyanoacetylene in higher vibrationally excited states and C₂H₅CN are not detected.

It is worth to mention that MM3 and MM9 have larger volume density ($6.1 \times 10^6 \text{ cm}^{-3}$ and $15.9 \times 10^6 \text{ cm}^{-3}$) than other four starless cores (1.9×10^6 , 2.2×10^6 , 2.8×10^6 , and $0.6 \times 10^6 \text{ cm}^{-3}$ for MM2, MM5, MM10, and MM12, respectively; see more details in Table 1 of Liu et al. 2017). Although MM3 and MM9 are not resolved in our 3 mm continuum emission, we extracted the spectra for the position of those cores which are shown in Figure C1. It shows that species such as CS, SO, H₂CO, CH₃OH $v=0$, HC₃N $v=0$, HC¹³CCN $v=0$, HCC¹³CN $v=0$, HC₃N $v_7=1$, and HC₅N are detected toward MM3; CS, SO, ³⁴SO, H₂CO, CH₃OH $v=0$, HC₃N $v=0$, HC¹³CCN $v=0$, HCC¹³CN $v=0$, and CH₃CHO are detected at MM9.

3.3 Spatial distributions

The integrated intensity maps of main transitions of Oxygen-, Nitrogen- and Sulphur-bearing species are shown in Figure 5–7. Analyzed the spatial distribution, we note that on the whole, transitions with low upper-level energy are expected to trace more extended and diffuse gas structures than with high upper-level energy. Three main results for emissions of O-, N-, and S-bearing species are as follows:

(i) Emission of CH₃OH $v=0$ covers extended parts, while emission of its torsional state CH₃OH $v_t=1$ with higher upper-level energy only distributes over the four dense cores MM4, MM7, MM8, and MM11. The spatial distributions of CH₃OCHO $v_t=1$ and C₂H₅OH concentrate on MM4 and MM8, the other O-bearing molecules primarily originate from MM4, MM7, MM8, and MM11 (see Figure 5). Meanwhile, the emission from MM4 is stronger than that from MM8 for O-bearing species except for CH₃CHO. The gas distributions of CH₃CHO extended to the eastern region, which is likely to be affected by an outflow.

(ii) Figure 6a shows the spatial distribution of HC₃N $v=0$, covering a large scale and extending to MM1 and MM11. In addition, an outflow originating from MM6 along the northeast-southwest direction is also traced by HC₃N $v=0$. Emission of its isotopologues HC¹³CCN $v=0$ peaks at MM4, MM7, and MM8, since isotopic molecules trace denser and more optically thin gas compare to its main species. HC₃N in vibrationally excited state $v_7=1$ peaks at MM4, MM7, and MM8, and higher energy $v_6=1$ (747 K) only

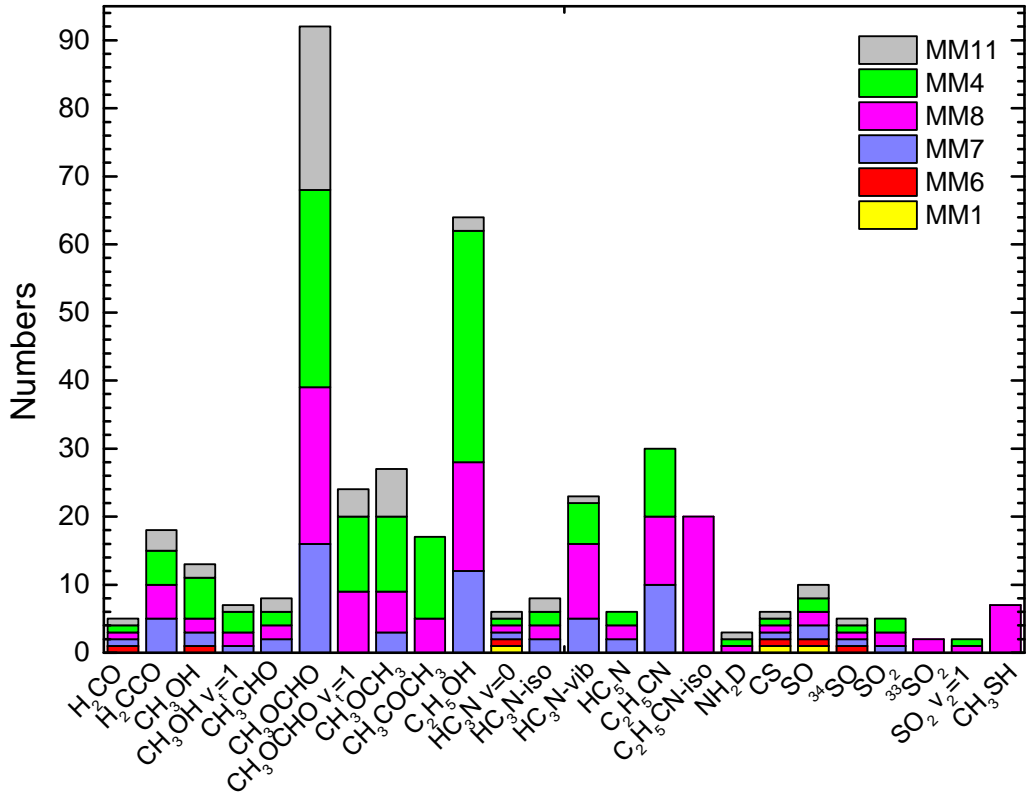


Figure 3. Molecules including O-bearing (H_2CO , H_2CCO , CH_3OH , CH_3OH $v_1=1$, CH_3CHO , CH_3OCHO , CH_3OCHO $v_1=1$, CH_3OCH_3 , CH_3COCH_3 , and $\text{C}_2\text{H}_5\text{OH}$), N-bearing (HC_3N , HC_5N , $\text{C}_2\text{H}_5\text{CN}$, and NH_2D), and S-bearing (CS , SO , ^{34}SO , SO_2 , $^{33}\text{SO}_2$, SO_2 $v_2=1$, and CH_3SH) molecules that have been identified toward the six cores. The numbers on the Y-axis indicate the detected molecular transition number of each core. X-axis presents the molecular name, in which the label "HC₃N-iso" indicates the HC₃N isotopologues HC¹³CCN and HCC¹³CN; "HC₃N-vib" means HC₃N in vibrationally excited states $v_7=1$, $v_7=2$, $v_7=3$, $v_6=1$, as well as HC¹³CCN $v_7=1$ and HCC¹³CN $v_7=1$; C₂H₅CN-iso contains $\text{CH}_3\text{CH}_2^{13}\text{CN}$, $\text{CH}_3^{13}\text{CH}_2\text{CN}$, and $^{13}\text{CH}_3\text{CH}_2\text{CN}$.

peaks toward the MM8, implying MM8 to have very warm environment. Nitrogen-bearing molecule C₂H₅CN has similar emission with those of HC¹³CCN $v=0$ and HC₃N $v_7=1$. Unlike the above Oxygen-bearing species that mainly peak at the position of MM4, the strongest emission of these N-bearing species is mostly located at MM8 with the exception of HC₅N for which the strongest emission is associated with MM4. Moreover, there is offset between its main emission peak and continuum emission peak MM4. A similar scenario is also seen for MM7 (see Figure 6e).

(iii) Similar to N-bearing species, S-bearing molecules mainly come from the MM4, MM7, and MM8. Observation shows that SO with low $E_u=9$ K and CS trace very extended regions. Furthermore, the collimated northeast-southwest outflow that comes from MM6 can be seen in CS and SO ($E_u = 9$ K) emission. The gas emission of SO₂ $v_2=1$ with E_u of 900 K is very compact and peaks at MM8. Emission of CH₃SH in low energy ($E_u = 14$ K) also comes from MM8, but it is not extremely compact.

4 LTE ANALYSES

In this section, we investigate the physical and chemical properties of six cores with sufficient number of molecular lines to derive

their physical parameters (rotational temperature, column density, and abundance) under LTE condition. All LTE modeled spectra are shown in Figure 4 and Figure B1.

4.1 LTE calculation

We model the observed spectra using the XCLASS suite. The software contains an interface for the model optimizer package MAGIX (Modeling and Analysis Generic Interface for eXternal numerical codes; Möller et al. 2013), which helps to optimize the fit, finds the best solutions of parameters, and provides corresponding error estimates by using different optimization algorithms or algorithm chain. In this work, three algorithm including Genetic, Levenberg–Marquardt, and Markov chain Monte Carlo were adopted. The main modeling parameters of XCLASS for each molecule are the source size, rotational temperature, column density, full width at half maximum of the observed line, and the velocity offset of the line with respect to the systemic velocity of the object. For the compact components, the source sizes is obtained by two-dimensional Gaussian fits to the line images. For extended components, the beam filling factor is always ~ 1 , we adopt very large source size. While for some species, the source size is comparable to the beam size, thus the source size is set as free parameters. The velocity offsets

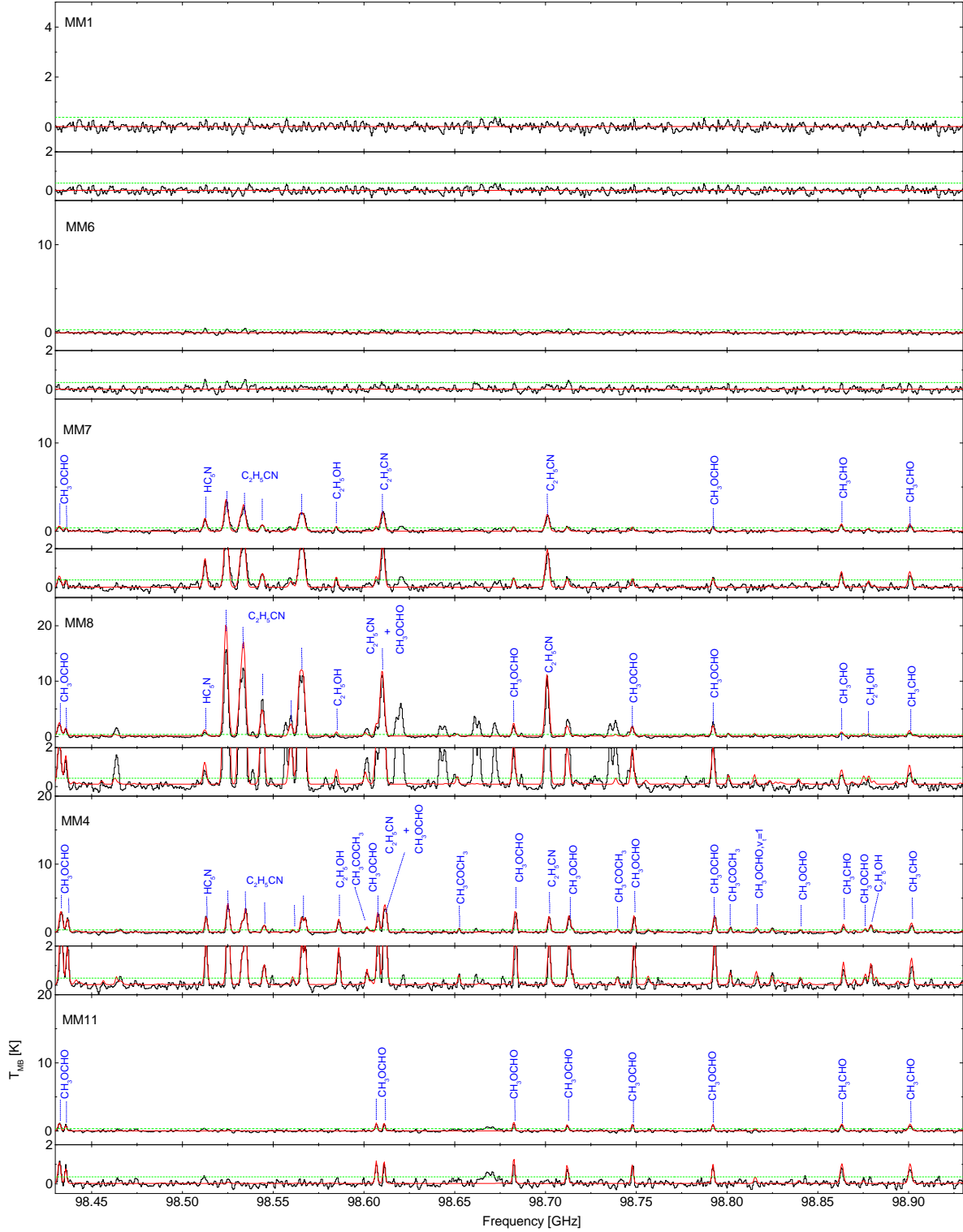


Figure 4. Beam-averaged spectra toward the MM1, MM6, MM7, MM8, MM4, and MM11. This segment covers frequency range from 98.43 to 98.93 GHz, the rest of other frequencies are showed in Figure B1. The frequency scale is in terms of rest frequency. The black curves are the observed spectra, and the red curves indicate the simulated LTE spectra. The horizontal green dashed line indicates the 3σ noise level in each core. The small panel below each spectrum shows the transitions that have been zoomed in.

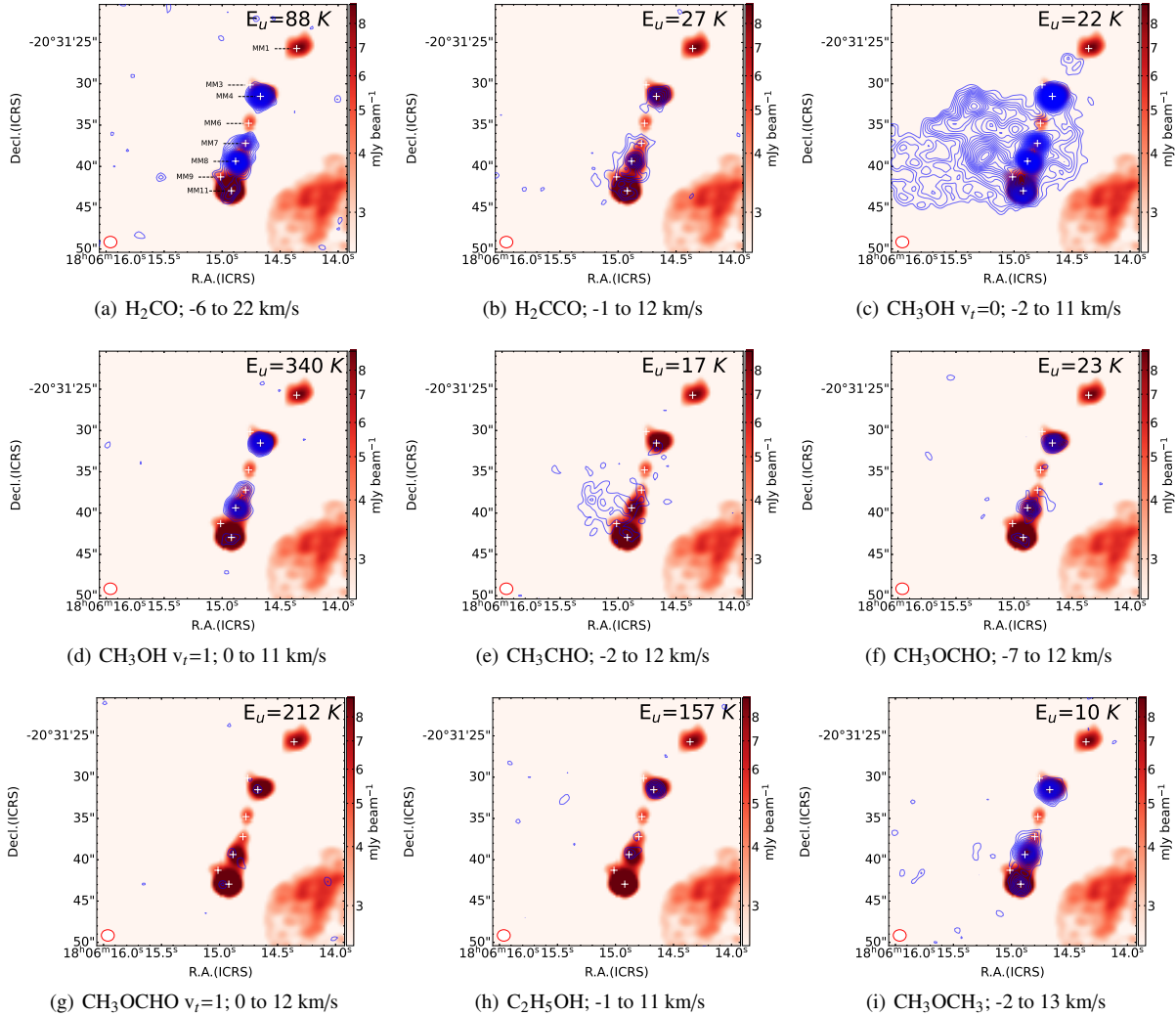


Figure 5. Spatial distributions of O-bearing molecules observed by 12-m array. The orange background shows the 12-m continuum emission at 3 mm. The synthetic beam for continuum is indicated in the bottom left corner by the open ellipse. Continuum peaks MM1, MM3, MM4, MM6, MM7, MM8, MM9, and MM11 are denoted by the white cross symbols. The blue contour levels show the line emission starting from 5σ to the maximum by 2σ , where σ is the rms noise. The 1σ of H_2CO , H_2CCO , $\text{CH}_3\text{OH } v_t=0$, $\text{CH}_3\text{OH } v_t=1$, CH_3CHO , CH_3OCHO , $\text{CH}_3\text{OCHO } v_t=1$, $\text{C}_2\text{H}_5\text{OH}$, and CH_3OCH_3 are 1.17, 0.81, 0.81, 0.77, 0.81, 0.95, 0.77, 0.77, and 0.85 K km/s, respectively. The value of upper-level energy E_u for each species is shown in the right-upper corner of each panel.

and line widths are derived from Gaussian fits to the spectral lines. The rest of the parameters are set as free parameters, mainly the rotational temperature and column density. Then MAGIX is used to minimizes the χ^2 in the given parameter space.

4.2 Rotational Temperatures and Column Densities

The molecular transitions that are unaffected by blending effect and cover a large upper-level energy E_u range, are most suitable for constraining the physical parameters. In our line survey SPW 7–8, molecular species with more than three detected transitions along with wide E_u range are used to evaluate the rotational temperature T_{rot} and source-averaged total column density N_T . Table 2 summarizes the best fitting results. All lines above 3σ noise level in the spectra are analyzed. For each detected line, the optical depth (τ^{line}) computed with XCLASS is listed in Table B1. The CS (2-1) transition in MM7 and MM8 has the highest optical depths of 1.32 and 1.17, respectively. The optical depth of the other molecular transi-

tions are lower than 1. The fitted rotational temperature and column density are discussed below.

Ketene (H_2CCO): Five unblended transitions of H_2CCO spanning E_u of 15–133 K are detected in MM7, MM8, and MM4. Toward the MM11, only three transitions are well detected with high S/N (> 3). The rotational temperatures of 72 ± 19 K, 102 ± 10 K, 102 ± 30 K and 84 ± 23 K, and column densities of $(1.6 \pm 0.7) \times 10^{15} \text{ cm}^{-2}$, $(5.5 \pm 0.1) \times 10^{15} \text{ cm}^{-2}$, $(5.0 \pm 1.7) \times 10^{15} \text{ cm}^{-2}$, and $(1.6 \pm 0.7) \times 10^{15} \text{ cm}^{-2}$ toward the MM7, MM8, MM4, and MM11, respectively, are derived by fitting those uncontaminated transitions (see Table 2).

Methanol (CH_3OH): Methanol is detected in ground state toward MM6, MM7, MM8, MM4, and MM11, and in torsionally excited state toward MM7, MM8, MM4, and MM11. The number of transitions over three are identified only toward MM4, allowing the determination of parameters. Transitions of $\text{CH}_3\text{OH } v_t=0$ cover a E_u range from 22 to 889 K and $\text{CH}_3\text{OH } v_t=1$ cover E_u range from 340 to 902 K. The excitation temperature and column density are 159 ± 8 K and $(7.5 \pm 0.3) \times 10^{17} \text{ cm}^{-2}$ for ground state, 204 ± 20 K and $(9.2 \pm 0.7) \times 10^{17} \text{ cm}^{-2}$ for torsional state.

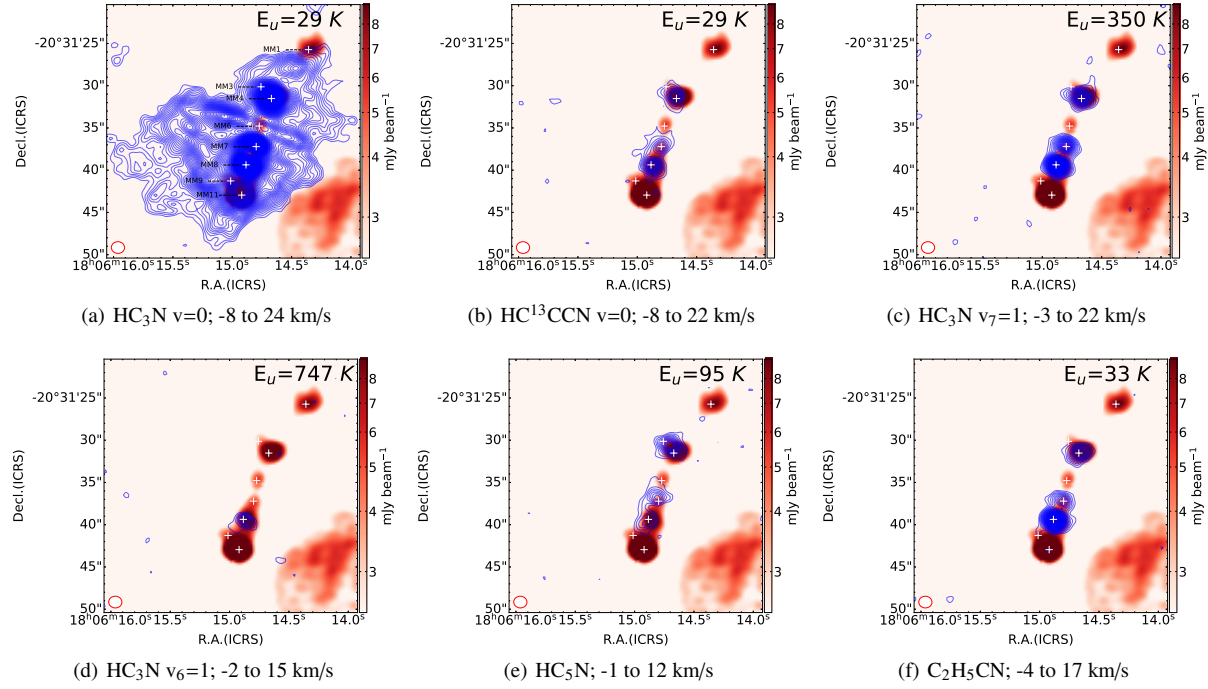


Figure 6. Spatial distributions of N-bearing molecules. See caption of Figure 5 for more details. The 1σ noise level of HC_3N $v=0$, HC^{13}CCN $v=0$, HC_3N $v_7=1$, HC_3N $v_6=1$, HC_5N , and $\text{C}_2\text{H}_5\text{CN}$ are 1.22, 1.17, 1.08, 0.92, 0.81, and 0.99 K km/s, respectively. The value of upper-level energy E_u for each species is shown in the right-upper corner of each panel.

Methyl Formate (CH_3OCHO): Methyl Formate in ground state is identified toward MM7, MM8, MM4, and MM11. Excluding lines with intensity lower than 3σ , the largest number of uncontaminated transitions (15–54 K) are detected toward MM4. The rotational temperatures of 108 ± 35 K, 152 ± 25 K, 146 ± 10 K, and 123 ± 23 K are obtained toward the MM7, MM8, MM4, and MM11, respectively. The largest column density of $(1.3\pm0.1)\times10^{17}$ cm $^{-2}$ is obtained toward MM4. Its first excited torsional states $v_t=1$ (210–225 K) are identified only toward MM8 and MM4. The fitting of CH_3OCHO $v_t=1$ transitions give higher rotational temperatures and column densities (MM8: 163 ± 35 K, $(9.1\pm0.6)\times10^{16}$ cm $^{-2}$; MM4: 150 ± 33 K, $(1.0\pm0.4)\times10^{17}$ cm $^{-2}$) than those derived from CH_3OCHO $v=0$.

Dimethyl ether (CH_3OCH_3): The largest number of transitions (10 transitions with E_u of 10–196 K) of CH_3OCH_3 are detected toward MM4, which have T_{rot} of 106 ± 13 K and N_T of $(6.6\pm0.6)\times10^{16}$ cm $^{-2}$. Six unblended transitions with E_u of 10–101 K, are identified toward MM8, resulting T_{rot} of 111 ± 30 K and N_T of $(4.8\pm0.3)\times10^{16}$ cm $^{-2}$. Seven transitions spanning 10–101 K give the values of T_{rot} of 95 ± 32 K and N_T of $(2.9\pm0.9)\times10^{16}$ cm $^{-2}$ toward MM11. For MM7, three transitions with E_u of 10 K are observed. Therefore, its temperatures and densities cannot be calculated due to lack of sufficient E_u range.

Acetone (CH_3COCH_3): Acetone is excited only toward MM8 and MM4, but all lines in our frequency range have relatively weak intensities. By modeling 5 transitions (E_u of 14–81 K) toward the MM8 and 12 transitions (E_u of 14–111 K) toward MM4, we obtain the rotational temperatures and column densities are 100 ± 38 K, $(1.0\pm0.5)\times10^{16}$ cm $^{-2}$ for MM8, and 113 ± 31 K, $(1.1\pm0.2)\times10^{16}$ cm $^{-2}$ for MM4.

Ethanol ($\text{C}_2\text{H}_5\text{OH}$): Ethanol is the isomer of dimethyl ether. Thirty transitions of gauche-Ethanol and 4 transitions of trans-Ethanol toward MM4 cover a wide E_u range (35–444 K). A smaller

number of lines are detected toward MM7 and MM8 (MM7: 12; MM8: 16). Many spectral lines are below 3σ in these two cores. The rotational temperature is 149 ± 32 K toward MM8, slightly lower value of 131 ± 4 K toward MM4, and 99 ± 28 K toward MM7. Among the three cores, the highest column density of $(4.6\pm0.3)\times10^{16}$ cm $^{-2}$ is estimated for MM4. Only two lines are slightly stronger than 3σ toward MM11.

Ethyl Cyanide ($\text{C}_2\text{H}_5\text{CN}$): Ethyl Cyanide is detected toward MM7, MM8, and MM4. Ten lines of $\text{C}_2\text{H}_5\text{CN}$ with E_u ranging from 33 to 118 K are used for model fitting. The best fit parameters are $T_{\text{rot}}=115\pm26$ K and $N_T=(4.4\pm0.9)\times10^{15}$ cm $^{-2}$ toward MM7, 140 ± 21 K and $(3.4\pm0.7)\times10^{16}$ cm $^{-2}$ toward MM8, 114 ± 14 K and $(4.3\pm0.3)\times10^{15}$ cm $^{-2}$ toward MM4. Additionally, within the observed bandwidth we detected 20 unblended lines of $\text{C}_2\text{H}_5\text{CN}$ isotopologues (10 $\text{CH}_3\text{CH}_2^{13}\text{CN}$ lines, 9 $\text{CH}_3^{13}\text{CH}_2\text{CN}$ and 1 $^{13}\text{CH}_3\text{CH}_2\text{CN}$ line) toward MM8. The column densities of $(1.4\pm0.5)\times10^{15}$ cm $^{-2}$ have been estimated by fixing the rotational temperature similar to that found from main isotopologue $\text{C}_2\text{H}_5\text{CN}$. Therefore, $^{12}\text{C}/^{13}\text{C}$ ratio of 24 ± 8 is derived (see Section 4.4 for more details).

Methyl Mercaptan (CH_3SH): Methyl Mercaptan with E_u covering from 17 K to 53 K are identified toward MM8. T_{rot} and N_T are 156 ± 21 K and $(3.7\pm0.9)\times10^{16}$ cm $^{-2}$, respectively.

Parameters from molecules with one or two identified transitions: As mentioned above, some molecules (e.g., methanol, acetaldehyde, dimethyl ether, etc) are observed with only one or two detected transitions. In this case, we fix the rotational temperature, then get the column densities for those species. Assuming the gas temperature of each core is equal to the average value of rotational temperatures derived from spectral fits, we use 99 K, 134 K, 137 K, and 100 K as the gas temperatures toward MM7, MM8, MM4, and MM11. The derived column densities are listed in Table 2. For CH_3CHO , four

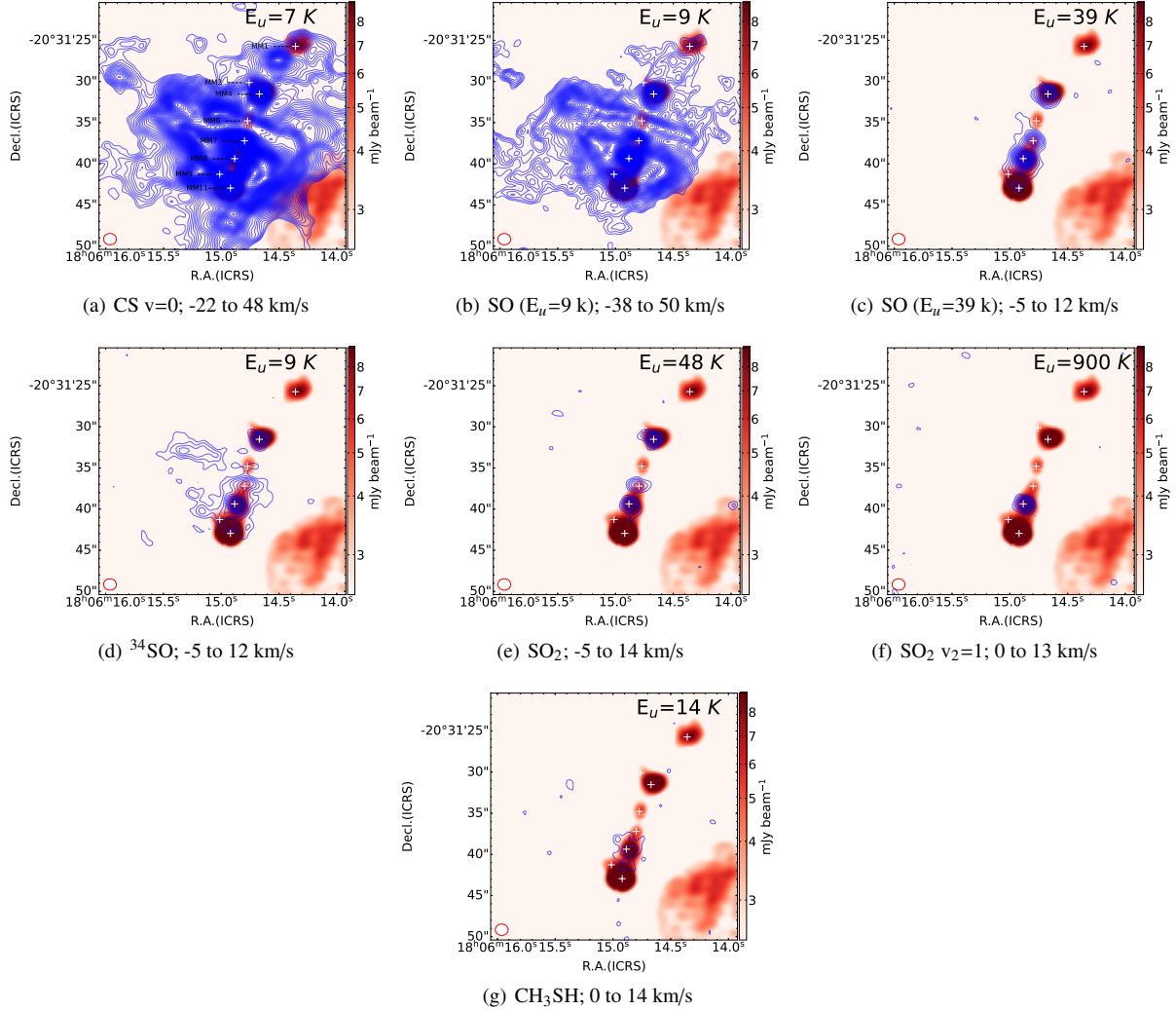


Figure 7. Spatial distributions of S-bearing molecules. See caption of Figure 5 for more details. The 1σ noise level of CS $v=0$, SO ($E_u=9$ K), ^{34}SO , SO_2 , SO_2 $v_2=1$, and CH_3SH are 1.77, 1.51, 0.88, 0.92, 0.85, 0.95, 0.81, and 0.85 K km/s, respectively. The value of upper-level energy E_u for each species is shown in the right-upper corner of each panel.

cores have N_T ranging from $3.4 \times 10^{15} \text{ cm}^{-2}$ to $5.3 \times 10^{15} \text{ cm}^{-2}$. The column densities of CH_3OH toward MM7, MM8, and MM11 are $3.0 \times 10^{17} \text{ cm}^{-2}$, $4.0 \times 10^{17} \text{ cm}^{-2}$, and $2.0 \times 10^{17} \text{ cm}^{-2}$, respectively. The value of $1.8 \times 10^{16} \text{ cm}^{-2}$ for CH_3OCH_3 at MM7, and $9.0 \times 10^{15} \text{ cm}^{-2}$ for $\text{C}_2\text{H}_5\text{OH}$ at MM11 have been estimated. Two lines of HC_5N and two lines of ^{13}C isotopic of HC_3N $v=0$ (HC^{13}CCN and HCC^{13}CN) are identified toward MM7, MM8, and MM4, with molecular column densities of $\sim 10^{14} \text{ cm}^{-2}$.

Table 2. Model fitting results of detected molecules.

Molecular name	MM7			MM8			MM4			MM11		
	T_{rot} (K)	N_{T} (10^{16}cm^{-2})	χ (10^{-8})	T_{rot} (K)	N_{T} (10^{16}cm^{-2})	χ (10^{-8})	T_{rot} (K)	N_{T} (10^{16}cm^{-2})	χ (10^{-8})	T_{rot} (K)	N_{T} (10^{16}cm^{-2})	χ (10^{-8})
H ₂ CCO	72±19	0.16±0.07	0.7±0.3	102±10	0.55±0.01	1.5±0.1	102±30	0.50±0.17	1.5±0.6	84±23	0.16±0.07	0.6±0.3
CH ₃ OH	99	30	130.0±11.3	134	40	105.0±8.3	159±8	75.0±3.2	227.0±29.2	100	20	71.4±5.1
CH ₃ OH $v_f=1$	204±20	92.3±6.5	280.0±39.2
CH ₃ CHO	99	0.34	1.5±0.1	134	0.50	1.3±0.1	137	0.53	1.6±0.2	100	0.38	1.4±0.1
C ₂ H ₅ OH	99±28	1.1±0.2	4.8±1.0	149±32	2.1±0.7	5.5±1.9	131±4	4.6±0.3	13.9±1.9	100	0.9	3.2±0.2
CH ₃ OCHO	108±35	1.1±0.5	4.8±2.2	152±25	5.9±0.5	15.5±1.8	146±10	13.0±1.0	39.4±5.7	123±23	3.1±0.8	11.1±3.0
CH ₃ OCHO $v_f=1$	163±35	9.1±0.6	23.9±2.5	150±33	10.5±4.2	31.8±13.3
CH ₃ OCH ₃	99	1.8	7.8±0.7	111±30	4.8±0.3	12.6±1.3	106±13	6.6±0.6	20.0±3.0	95±31	2.9±0.9	10.4±3.3
CH ₃ COCH ₃	100±34	1.0±0.5	2.6±1.3	113±31	1.1±0.2	3.3±0.7
C ₂ H ₅ CN	115±26	0.44±0.09	1.9±0.4	140±21	3.35±0.69	9.0±2.0	124±14	0.43±0.03	1.3±0.2
CH ₃ CH ₂ ¹³ CN	140	0.14±0.05	0.37±0.14
CH ₃ ¹³ CH ₂ CN	140	0.14±0.04	0.37±0.14
CH ₃ SH	156±21	3.7±0.9	9.7±2.5
HC ¹³ CCN $v=0$	99	0.019	0.082±0.007	134	0.056	0.15±0.01	137	0.035	0.10±0.01
HCC ¹³ CN $v=0$	99	0.022	0.096±0.008	134	0.060	0.16±0.01	137	0.035	0.10±0.01
HC ₅ N	99	0.030	0.13±0.01	134	0.026	0.070±0.006	137	0.060	0.18±0.02

Notes. For some species, their fitting errors of column densities are not given because detected transitions are below three. The column densities are derived by assuming the fixed T_{rot} of 99 K, 134 K, 137 K, and 100 K toward MM7, MM8, MM4, and MM11, respectively. The "..." means no molecular lines were detected. χ is abundance of specific molecule relative to H₂.

4.3 Molecular abundance

The fractional abundance of a certain molecule relative to H₂ ($\chi = N_T/N_{H_2}$) can be estimated from the source-averaged total column density of the certain molecule and that of the molecular hydrogen. With assumption of optically thin emission from dust, the column density of H₂ can be derived by using the following equation (e.g., Frau et al. 2010; Bonfand et al. 2019; Gieser et al. 2021):

$$N_{H_2} = \frac{S_\nu \eta}{\mu m_H \Omega \kappa_\nu B_\nu(T_d)}, \quad (1)$$

where S_ν is the total integrated flux of the continuum, $\eta = 100$ is gas-to-dust mass ratio (Lis et al. 1991; Hasegawa et al. 1992), $\mu = 2.8$ is the mean molecular mass per H₂ molecule (Kauffmann et al. 2008), m_H is the mass of the hydrogen atom, Ω is the solid angle subtended by the source, κ_ν is the dust absorption coefficient per unit density, and $B_\nu(T_d)$ is the Planck function at the dust temperature T_d .

The dust temperature should equal to the rotation temperature of the core derived from COMs, since gas and dust are expected to be thermally coupled well at density higher than 10⁶ cm⁻³ (Goldsmith 2001). In our case, the H₂ densities at four cores are larger than 10⁶ cm⁻³ (see Table 3). We use the dust continuum emission to estimate the column density of H₂. However, at 3 mm observations, free-free emission from ionized gas could contribute to the continuum emission (detailed analyses are provided in Liu et al. 2020a, 2021), which will overestimate the column density of H₂. Instead, we use 1.3 mm continuum data from Liu et al. (2017), and smooth it to the same spatial resolution as that of 3 mm continuum data. κ_ν of 0.899 cm² g⁻¹ at 1.3 mm for dust grains with thin ice mantles at a gas density of 10⁶ cm⁻³ is adopted (Ossenkopf & Henning 1994). The N_{H_2} derived from 1.3 mm continuum emission are: (2.3±0.2) × 10²³ cm⁻² for MM7, (3.8±0.3) × 10²³ cm⁻² for MM8, (3.3±0.4) × 10²³ cm⁻² for MM4 and (2.8±0.2) × 10²³ cm⁻² for MM11. The mean optical depth of continuum can be calculated by (e.g., Frau et al. 2010; Gieser et al. 2021)

$$\tau_\nu = -\ln\left(1 - \frac{S_\nu}{\Omega B_\nu(T_d)}\right). \quad (2)$$

The derived τ_ν toward four cores are on the order of 10⁻², guaranteeing reliable H₂ column density. Toward four cores, the deconvolved sizes, dust temperatures, total flux densities, values of optical depth, column densities of H₂, and volume densities of H₂ are listed in Table 3.

The fractional abundances of different species at each position are given in Table 2. Toward four cores (MM4, MM7, MM8 and MM11), H₂CCO has the lowest abundance, compared with other O-bearing molecules. The abundances of O-bearing COMs such as CH₃OH, CH₃OCHO, C₂H₅OH and CH₃OCH₃ toward MM4 are higher than that toward MM8, while the abundance of C₂H₅CN is largest toward MM8.

4.4 Carbon Isotopic Ratio

A large number of studies toward molecular clouds in the Galaxy showed that ¹²C/¹³C ratio is a function of Galactocentric distance D_{GC} (Langer & Penzias 1990, 1993). Recently, Yan et al. (2019) has reported a linear fit by observing H₂CO and H₂¹³CO from 112 sources:

$$^{12}\text{C}/^{13}\text{C} = (5.08 \pm 1.10) \text{kpc}^{-1} \times D_{GC} + (11.86 \pm 6.60), \quad (3)$$

At a Galactocentric distances of 3.4 kpc, the ¹²C/¹³C ratio is 29±8. We have estimated the ¹²C/¹³C ratio from HC₃N, C₂H₅CN and their

¹³C isotopologues, which are shown in Table 4. The ratios between HC₃N v=0 and its isotopologues are underestimated by a factor of six, which may due to the large optical depth and possible missing-flux of HC₃N v=0. Other five values are in the range of 23.9–25.6, which is in good agreement with the value derived from equation 3.

5 DISCUSSIONS

5.1 Physical parameters of individual molecule

In this section we mainly discuss the physical parameters of detected H₂CCO, HC₃N and other complex molecules. We also compare molecular abundances with respect to H₂ and CH₃OH derived in our work with those derived in other sources including high-mass star forming regions (HMSFRs), low-mass star forming regions (LMSFRs) and Galactic Center molecular clouds (GCMCs). Molecular abundances for individual source and corresponding references can be found in Table 5. Figure 8 shows the molecular abundance with respect to H₂ toward the sources in Table 5. On average, H₂CCO, CH₃CHO, and CH₃COCH₃, which have mean abundances of 8.8×10⁻⁹ – 3.4×10⁻⁸ (see Table 5), are relatively less abundant than other six COMs in HMSFRs, while CH₃OH, C₂H₅OH, CH₃OCH₃, CH₃OCHO and C₂H₅CN are usually rich in these sources. They are 1.2×10⁻⁷ – 3.4×10⁻⁶ in molecular abundances. In addition, averaged abundances of C₂H₅OH, CH₃OCH₃, CH₃OCHO, C₂H₅CN and CH₃SH from HMSFRs are higher than those from LMSFRs and GCMCs by almost 1-3 orders of magnitude. The following is the detailed discussion for each species:

Ketene (H₂CCO): When compared the rotational temperatures T_{rot} (72–102 K) and abundance χ ((6.0–15.0) × 10⁻⁹) of H₂CCO with those of other O-bearing species, H₂CCO has the lowest T_{rot} and χ in the four cores (MM4, MM7, MM8, and MM11). It suggests that this molecule is not produced in very hot and compact regions, but rather in warm envelopes compared to other species. Previous observations show that H₂CCO has been detected in massive star-forming regions such as Sgr B2 (e.g., Turner 1977; Nummelin et al. 2000) and Orion KL (Johansson et al. 1984; Crockett et al. 2014), cold dark cloud TMC-1 (Ohishi et al. 1991), and several deeply embedded protostars like NGC 6334I and NGC 7538 I1 (Ruiterkamp et al. 2007). Furthermore, these observations reveal that H₂CCO has abundances of ∼ 10⁻¹⁰ relative to H₂, which is slightly lower than the values of the four cores (MM7, MM8, MM4, and MM11) of 9.62±0.19. Previous observations also shown that H₂CCO is more abundant in the cooler and extended region (Maity et al. 2014).

Acetaldehyde (CH₃CHO): Under the assumption of fixed temperature, relatively lower column densities ((3.4–5.3) × 10¹⁵ cm⁻²) and abundances ((1.3–1.6) × 10⁻⁸) of CH₃CHO are obtained toward four cores than that for other species. Moreover, the spatial distribution of CH₃CHO is not well coincident with the positions of MM4, MM8, and MM11. It might imply that CH₃CHO tend to trace more externally extended gas.

Methanol (CH₃OH): CH₃OH v=0 has high abundances between 7.1×10⁻⁷ and 2.3×10⁻⁶ toward four cores. This species is efficiently formed in molecular clouds from early to evolved stage. The gas distributions cover a more extended region. The much higher temperature (204 K) and abundance (2.8×10⁻⁶) for CH₃OH in the first excited torsional state ($v_t=1$) derived toward MM4. CH₃OH $v_t=1$ with very high excitation energy should originate from a very warm and compact region.

Ethanol (C₂H₅OH): The abundances toward MM7 ((4.8±1.0)×10⁻⁸), MM8 ((5.5±1.9)×10⁻⁸), and MM11 ((

Table 3. Properties of four dense cores derived by 1.3 mm smooth data.

Position	source size ^a	T_d ^b (K)	I_{peak} mJy beam ⁻¹	S_v ^a (mJy)	τ_v (10^{-2})	N_{H_2} (10^{23}cm^{-2})	n_{H_2} (10^6cm^{-3})
MM7	$2.3'' \times 1.3''$	99	16.8 ± 0.9	109.7 ± 0.6	0.96	2.3 ± 0.2	~ 1.7
MM8	$2.6'' \times 1.4''$	134	45.2 ± 1.8	305 ± 15	1.60	3.8 ± 0.3	~ 2.6
MM4	$2.1'' \times 1.8''$	137	40.4 ± 1.9	266 ± 14	1.38	3.3 ± 0.4	~ 3.6
MM11	$2.8'' \times 1.8''$	100	26.0 ± 1.1	229 ± 11	1.18	2.8 ± 0.2	~ 1.6

Notes. ^a The deconvolved size and total flux density of each core are obtained from 2D Gaussian fitting to 1.3 mm continuum. ^b The dust temperatures for four dense cores are estimated from the average rotational temperature for detected species.

Table 4. Isotopologue Ratios.

Ratio	MM8
$\text{HC}_3\text{N } v=0/\text{HC}^{13}\text{CCN } v=0$	~ 4.2
$\text{HC}_3\text{N } v=0/\text{HCC}^{13}\text{CN } v=0$	~ 4.0
$\text{HC}_3\text{N } v_7=1/\text{HC}^{13}\text{CCN } v_7=1$	~ 25.6
$\text{HC}_3\text{N } v_7=1/\text{HCC}^{13}\text{CN } v_7=1$	~ 24.2
$\text{CH}_3\text{CH}_2\text{CN}/\text{CH}_3\text{CH}_2^{13}\text{CN}$	23.9 ± 9.8
$\text{CH}_3\text{CH}_2\text{CN}/\text{CH}_3^{13}\text{CH}_2\text{CN}$	23.9 ± 8.4
$\text{CH}_3\text{CH}_2\text{CN}/^{13}\text{CH}_3\text{CH}_2\text{CN}$	23.9

Notes. Detected spectral lines of $\text{HC}_3\text{N } v=0$, $\text{HC}_3\text{N } v_7=1$, and their ^{13}C isotopologues are below three, the column densities of these species are modelled by assuming the rotational temperatures is equal to $\text{C}_2\text{H}_5\text{CN}$.

$(3.2 \pm 0.2) \times 10^{-8}$) do not present obvious differences. The abundance increases to $(1.4 \pm 0.2) \times 10^{-7}$ toward MM4. The derived temperature are 149 ± 32 K for MM8 and 131 ± 4 K for MM4, which is consistent with the understanding that $\text{C}_2\text{H}_5\text{OH}$ usually has rotational temperature higher than 100 K in massive hot cores (e.g., [Bisschop et al. 2007](#)). Column density ratios between $\text{C}_2\text{H}_5\text{OH}$ and CH_3OH in four dense cores range from 0.037 to 0.061 (see Table 5), which consistent with the mean value $0.064^{+0.066}_{-0.041}$ measured from several HMSFRs ([Taquet et al. 2015](#)).

Dimethyl ether (CH_3OCH_3): CH_3OCH_3 is an isomer of $\text{C}_2\text{H}_5\text{OH}$. It has a lower temperature (MM8: 111 ± 30 K, MM4: 106 ± 13 K) than $\text{C}_2\text{H}_5\text{OH}$. The $\text{CH}_3\text{OCH}_3/\text{C}_2\text{H}_5\text{OH}$ abundance ratios are ~ 1.6 , 2.3, 1.4, and 3.2 toward MM7, MM8, MM4, and MM11, respectively, indicating that CH_3OCH_3 is more abundant than $\text{C}_2\text{H}_5\text{OH}$ in dense cores. Meanwhile, it can be seen from Figure 8 that abundances of CH_3OCH_3 are generally higher than those of $\text{C}_2\text{H}_5\text{OH}$ in HMSFRs. Also, the averaged abundance ratio between CH_3OCH_3 and $\text{C}_2\text{H}_5\text{OH}$ for those regions is around 2.5. The abundances of two species are nearly same for three LMSFRs IRAS 16293-2422B, NGC 1333-IRAS 2A, and NGC 1333-IRAS 4A. The formation efficiency of these two isomers in various environments may be different.

Methyl Formate (CH_3OCHO): For the G9.62+0.19, its temperatures are between 108 K and 152 K. The abundance increases by an order of magnitude from MM7 (4.8×10^{-8}) to MM4 (3.9×10^{-7}). The rotational temperatures of ground state and first torsional excited state are similar considering the uncertainties. This is consistent with the findings of [Favre et al. \(2011\)](#), who obtained similar temperatures between $\text{CH}_3\text{OCHO } v=0$ and $\text{CH}_3\text{OCHO } v_7=1$ in Orion KL region. [Taquet et al. \(2015\)](#) gives an averaged CH_3OCHO abundance with respect to CH_3OH of $0.14^{+0.18}_{-0.06}$ for HMSFRs. The

abundances in our three cores MM4, MM8, and MM11 are 0.17, 0.15, and 0.16, respectively, which are consistent with $0.14^{+0.18}_{-0.06}$. However, the abundance of 0.037 toward MM7 are lower than the mean value derived in other HMSFRs.

Acetone (CH_3COCH_3): CH_3COCH_3 shows low temperature (100 – 113 K) and abundance (2.6×10^{-8} – 3.3×10^{-8}) in MM8 and MM4. The abundances are larger than those derived from Orion KL hot core and compact ridge regions ($\sim 10^{-9}$ for Orion KL; see Table 5).

Ethyl Cyanide ($\text{C}_2\text{H}_5\text{CN}$): $\text{C}_2\text{H}_5\text{CN}$ is usually used as a hot core tracer because of its high rotational temperature. We found that the temperatures are 115 ± 26 K, 140 ± 21 K and 124 ± 21 K for the MM7, MM8 and MM4, respectively. It may be destroyed by UV radiation in the MM11 region. Its abundance is larger by nearly one order of magnitude toward MM8 than that toward MM7 and MM4. Furthermore, $\text{C}_2\text{H}_5\text{CN}$ abundances toward HMSFRs (average value of $\sim 10^{-7}$) are obviously higher than those toward LMSFRs and GMCs ($\sim 10^{-10}$) (see Table 5).

Cyanobutadiyne (HC_5N): Because fewer than three lines were detected, T_{rot} and N_T could not be obtained from spectral line fits. We derived column densities and abundances of $\text{HC}_5\text{N } v=0$ toward three cores with the assumption of $T_{\text{rot}} = 99$ K, 134 K, and 137 K for MM7, MM8, and MM4, respectively. The derived HC_5N abundance in the range of $(7.0$ – $18) \times 10^{-10}$ are slightly lower than that in other four hot cores G10.30-0.15, G12.89+0.49, G16.86-2.16 and G28.28-0.36 (6.3×10^{-10} – 4.2×10^{-9}) ([Taniguchi et al. 2017](#)) and in Galactic Center molecular cloud G+0.693-0.027 (1.9×10^{-9}) ([Zeng et al. 2018](#)), and slightly higher than the value measured from L1527 (WCCC) ($(1.2 \pm 0.3) \times 10^{-10}$) ([Jørgensen et al. 2002](#); [Sakai & Yamamoto 2013](#)). A very low HC_5N abundance, 1.1×10^{-11} has been measured toward the outer cold envelope of IRAS 16293 ([Jaber et al. 2017](#)). The peaks of the gas emission are not well associated with the continuum peaks MM4, MM7 and MM8. Such results seem to imply that HC_5N is not excited in the densest part of three dense cores, especially for MM4 and MM7. [Fontani et al. \(2017\)](#) also found that the emission of HC_5N in the protocluster OMC-2 FIR4 is not associated with continuum emission.

Methyl Mercaptan (CH_3SH): Few S-bearing COMs has been detected in the ISM so far. As one of the simplest S-bearing COMs, CH_3SH has been detected in a few high-mass star-forming regions like Sgr B2(N) ([Müller et al. 2016](#)), Orion KL ([Kolesniková 2014](#)), G327.3-6 ([Gibb et al. 2000](#)) and G31.41+0.31 ([Gorai et al. 2021](#)), low-mass protostar IRAS 16293-2422 ([Majumdar et al. 2016](#)), and Galactic Center molecular cloud G+0.693-0.027 ([Rodríguez-Almeida et al. 2021](#)). In these sources, CH_3SH has the temperature range ~ 68 – 200 K and abundance from 1.0×10^{-9} to 9.4×10^{-8} for above hot cores, but lower temperature (32 K) and abundance (5.0×10^{-10}) for solar-type protostar IRAS 16293-2422, a much

lower temperatures of 8.5–14.9 K and abundance of 4.8×10^{-9} for G+0.693-0.027. Our observations give the rotational temperature of 156 ± 21 K and abundance of $(9.7 \pm 2.5) \times 10^{-8}$ toward MM8, which is consistent with the upper limit of the parameter range derived from other hot cores.

Table 5. Molecular abundances relative to CH₃OH and H₂ obtained in G9.62+0.19 and other regions.

Source	[H ₂ CCO] /[CH ₃ OH] /[H ₂]		[CH ₃ OH] /[CH ₃ OH] /[H ₂]		[CH ₃ CHO] /[CH ₃ OH] /[H ₂]		[C ₂ H ₅ OH] /[CH ₃ OH] /[H ₂]		[CH ₃ OCH ₃] /[CH ₃ OH] /[H ₂]		[CH ₃ OCHO] /[CH ₃ OH] /[H ₂]		[CH ₃ COCH ₃] /[CH ₃ OH] /[H ₂]		[C ₂ H ₅ CN] /[CH ₃ OH] /[H ₂]		[CH ₃ SH] /[CH ₃ OH] /[H ₂]		Reference
High-mass star forming regions																			
G9.62+0.19 (MM4)	6.7(-3)	1.5(-8)	1	2.3(-6)	7.1(-3)	1.6(-8)	6.1(-2)	1.4(-7)	8.8(-2)	2.0(-7)	1.7(-1)	3.9(-7)	1.5(-2)	3.3(-8)	5.7(-3)	1.3(-8)	—	—	this work
G9.62+0.19 (MM7)	5.3(-3)	7.0(-9)	1	1.3(-6)	1.1(-2)	1.5(-8)	3.7(-2)	4.8(-8)	6.0(-2)	7.8(-8)	3.7(-2)	4.8(-8)	—	—	1.5(-2)	1.9(-8)	—	—	this work
G9.62+0.19 (MM8)	1.4(-2)	1.5(-8)	1	1.1(-6)	1.3(-2)	1.3(-8)	5.3(-2)	5.5(-8)	1.2(-1)	1.3(-7)	1.5(-1)	1.6(-7)	2.5(-2)	2.6(-8)	8.5(-2)	9.0(-8)	9.3(-2)	9.7(-8)	this work
G9.62+0.19 (MM11)	8.0(-3)	5.7(-9)	1	7.1(-7)	1.9(-2)	1.4(-8)	4.5(-2)	3.2(-8)	1.5(-1)	1.0(-7)	1.6(-1)	1.1(-7)	—	—	—	—	—	—	this work
Orion KL (HC) ^a	—	—	1	1.8(-6)	—	—	2.0(-2)	3.6(-8)	3.4(-2)	6.1(-8)	7.4(-2)	1.3(-7)	1.5(-3)	2.8(-9)	—	—	—	—	1
Orion KL (CR) ^b	—	—	1	1.3(-6)	—	—	4.6(-3)	4.9(-9)	9.3(-2)	1.2(-7)	2.2(-1)	2.9(-7)	4.6(-4)	1.0(-10)	—	—	—	—	1
Orion KL (HC)	—	—	1	2.2(-6)	—	—	—	3.1(-2)	6.8(-8)	—	—	—	—	4.1(-2)	8.9(-8)	—	—	2	
Orion KL (CR)	—	—	1	1.2(-6)	—	—	—	1.4(-1)	1.7(-7)	2.8(-1)	3.3(-7)	—	—	—	—	—	—	2	
Orion KL (HC)	3.3(-3)	6.9(-10)	1	2.1(-7)	2.8(-2)	5.8(-9)	3.0(-2)	6.3(-9)	6.3(-1)	1.3(-7)	1.1(-1)	2.3(-8)	2.1(-2)	4.5(-9)	4.5(-2)	9.6(-9)	—	—	3
Orion KL (CR) ^c	2.9(-3)	1.3(-9)	1	4.3(-7)	4.5(-2)	1.9(-8)	2.0(-2)	8.6(-9)	6.9(-1)	2.9(-7)	3.4(-1)	1.5(-7)	2.9(-3)	1.2(-9)	7.7(-3)	3.3(-9)	—	—	3
Sgr B2(N1)	3.4(-2)	1.3(-8)	1	3.9(-7)	8.1(-3)	3.2(-9)	5.2(-2)	2.0(-8)	1.1(-1)	4.3(-8)	2.5(-2)	9.6(-9)	—	—	1.1(-1)	4.1(-8)	1.7(-3)	6.5(-10)	4
Sgr B2(N2)	6.8(-2)	2.1(-8)	1	3.0(-7)	1.8(-2)	5.5(-9)	9.1(-2)	2.8(-8)	2.1(-1)	6.5(-8)	3.3(-2)	1.0(-8)	—	—	4.9(-1)	1.5(-7)	4.6(-3)	1.4(-9)	4
Sgr B2(M)	7.0(-2)	8.0(-9)	1	1.1(-7)	1.0(-4)	1.2(-11)	3.7(-3)	4.3(-10)	1.3(-3)	1.5(-10)	4.0(-3)	4.6(-10)	—	—	1.8(-3)	2.0(-10)	1.8(-3)	2.1(-10)	4
Sgr B2(N2)	8.3(-3)	—	1	2.4(-5)	1.1(-2)	2.6(-7)	5.0(-2)	1.2(-6)	5.5(-2)	1.3(-6)	3.0(-2)	7.3(-7)	1.0(-2)	—	1.6(-1)	3.8(-6)	8.5(-3)	2.1(-7)	5, 12
Sgr B2(N3)	—	—	1	8.3(-6)	1.1(-2)	9.4(-8)	4.1(-2)	3.4(-7)	1.3(-1)	1.1(-6)	2.3(-1)	1.9(-6)	—	—	4.3(-2)	3.6(-7)	1.1(-2)	9.4(-8)	5
Sgr B2(N4)	—	—	1	9.8(-8)	4.0(-2)	3.9(-9)	1.0(-1)	9.8(-9)	3.6(-1)	3.5(-8)	4.4(-1)	4.3(-8)	—	—	5.6(-2)	5.5(-9)	3.8(-2)	3.7(-9)	5
Sgr B2(N5)	—	—	1	2.2(-6)	1.3(-2)	2.8(-8)	5.0(-2)	1.1(-7)	2.3(-1)	5.0(-7)	1.2(-1)	2.7(-7)	—	—	3.4(-2)	7.6(-8)	1.8(-2)	3.9(-8)	5
AFGL 4176	1.2(-3)	1.6(-8)	1	1.4(-5)	2.7(-3)	3.8(-8)	1.4(-2)	1.9(-7)	2.4(-2)	2.5(-8)	3.1(-2)	4.3(-7)	4.2(-3)	5.8(-8)	1.0(-3)	1.4(-8)	—	—	6
NGC 6334I	4.3(-4)	2.0(-9)	1	4.7(-6)	—	—	1.0(-2)	4.7(-8)	2.1(-1)	1.0(-6)	5.1(-2)	2.4(-7)	—	—	—	—	—	—	7
G31.41+0.31	—	—	—	—	—	—	—	8.4(-9)	—	8.4(-8)	—	4.2(-8)	—	—	—	—	2.3(-2)	2.7(-8)	8, 9
7 high-mass YSOs ^d	1.7(-4)	3.2(-10)	1	1.9(-6)	2.9(-5)	5.6(-11)	1.9(-2)	3.6(-8)	4.1(-1)	7.7(-7)	8.9(-2)	1.7(-7)	—	—	8.9(-3)	1.7(-8)	—	—	10
Average	—	8.8(-9)	—	3.4(-6)	—	3.4(-8)	—	1.2(-7)	—	3.0(-7)	—	2.7(-7)	—	1.8(-8)	—	3.1(-7)	—	5.3(-8)	—
Low-mass star forming regions																			
IRAS 16293-2422B ^e	4.8(-3)	4.0(-9)	1	8.3(-7)	1.2(-2)	1.0(-8)	2.3(-2)	1.9(-8)	2.4(-2)	2.0(-8)	2.6(-2)	2.2(-8)	1.7(-3)	—	3.6(-4)	3.0(-10)	4.8(-4)	4.0(-10)	11, 12, 13
NGC 1333-IRAS 2A	1.4(-3)	1.4(-9)	1	1.0(-6)	—	—	1.6(-2)	1.6(-8)	1.0(-2)	1.0(-8)	1.6(-2)	1.6(-8)	—	—	3.0(-4)	3.0(-10)	—	—	14
NGC 1333-IRAS 4A	2.1(-3)	9.2(-10)	1	4.3(-7)	—	—	1.0(-2)	4.3(-9)	1.0(-2)	4.3(-9)	3.1(-2)	1.4(-8)	—	—	4.0(-4)	1.7(-10)	—	—	14
Galactic Center molecular clouds																			
G+0.693 ^f	1.6(-2)	7.0(-9)	1	4.5(-7)	5.7(-2)	3.6(-8)	6.9(-2)	3.1(-8)	6.0(-2)	2.7(-8)	1.0(-1)	4.7(-8)	—	—	—	—	—	—	15, 16
G+0.693 ^f	—	—	1	1.1(-7)	—	—	4.2(-2)	4.6(-9)	—	—	—	—	—	—	3.0(-10)	4.3(-2)	4.8(-9)	17, 18	
G-0.02	6.4(-3)	2.0(-9)	1	3.0(-7)	3.5(-2)	1.0(-8)	—	—	—	3.4(-2)	1.0(-8)	—	—	—	—	—	—	16	
G-0.11	1.5(-2)	1.6(-8)	1	1.1(-6)	2.7(-2)	3.0(-8)	—	—	—	7.1(-2)	7.8(-8)	—	—	—	—	—	—	16	

Notes. X(Y) means $X \times 10^Y$. ^a Correspond to "ET peak" in Fig. 1 of Tercero *et al.* (2018). ^b Correspond to "MF peak" in Fig. 1 of Tercero *et al.* (2018). ^c Correspond to "mm3b" in Feng *et al.* (2015). ^d The abundance for each molecule is the average value from 7 high-mass YSOs including AFGL 2591, G24.78, G75.78, NGC 6334 IRS1, NGC 7538 IRS1, W 3(H₂O), and W 33A. ^e The abundances relative to H₂ are derived by using the lower limit of H₂ column density ($1.2 \times 10^{25} \text{ cm}^{-2}$) from Jørgensen *et al.* (2016). Thus the abundances relative to H₂ from this source should be upper limits. ^f Requena-Torres *et al.* (2006) and Requena-Torres *et al.* (2008) used H₂ column density of $4.1 \times 10^{22} \text{ cm}^{-2}$ for abundance calculations, while Rodríguez-Almeida *et al.* (2021) and Zeng *et al.* (2018) used the value of $1.35 \times 10^{23} \text{ cm}^{-2}$.

References. (1) Tercero *et al.* (2018); (2) Crockett *et al.* (2014); (3) Feng *et al.* (2015); (4) Belloche *et al.* (2013); (5) Bonfand *et al.* (2019); (6) Bøgelund *et al.* (2019); (7) Zernickel *et al.* (2012); (8) Rivilla *et al.* (2017b); (9) Gorai *et al.* (2021); (10) Bisschop *et al.* (2007); (11) Jørgensen *et al.* (2018); (12) Jørgensen *et al.* (2020); (13) Drozdovskaya *et al.* (2019); (14) Taquet *et al.* (2015); (15) Requena-Torres *et al.* (2006); (16) Requena-Torres *et al.* (2008); (17) Rodríguez-Almeida *et al.* (2021); (18) Zeng *et al.* (2018).

5.2 Evolution of dense cores

In order to study the variations of temperatures and molecular abundance with the evolutionary sequence of the dense cores, the stage of each core need to be evaluated. According to the detected molecular species, molecular abundance, and line kinematic properties (e.g., outflow) of each core, the stage of the cores are classified as listed in Table 6. The general criteria for determining the relative evolutionary stage of the cores are summarized as follows.

Starless core/prestellar core should not drive an outflow. Spectra of this kind of core appears line-poor. MM3 and MM9 were not observed by centimeter continuum (Testi et al. 2000) and do not have outflow activities. They also do not excite abundant molecular lines (see Figure C1). Those lines (e.g., CS, SO, ^{34}SO , H_2CO , CH_3OH $v=0$, HC_3N $v=0$, etc.) detected in MM3 and MM9 are probably remnant emission from MM4 and MM11, respectively. MM3 and MM9 are considered as massive starless core candidates.

MM6 is more evolved, in which a collimated outflow is seen through CS (2–1), SO (3₂–2₁) and SiO (2–1) (see Figure 7 and Figure 9) emission. SiO (5–4) emission with ALMA 1.3 mm data presented by Liu et al. (2017) also showed this bar-like structure associated with MM6, which is very collimated and dominated by blueshifted emission. A small population of molecules such as CH_3OH are excited in this stage.

MM7, MM8, and MM4 may evolved into HMC phase. HMCs should have outflows, but this kind of outflows are not as highly collimated as from HMPOs. The significant feature of HMCs is that rich complex organic molecules and even in vibrationally and torsionally excited states (e.g., HC_3N $v_7=1$, HC_3N $v_6=1$, CH_3OH $v_t=1$, and CH_3OCHO $v_t=1$) exist in this phase. The vibrationally and torsionally excited states of molecules have higher upper energy levels and should be excited at a higher kinetic temperature. It suggests that molecules with higher E_u are good indicators for a more evolved region (Gieser et al. 2021). CH_3OCHO $v_t=1$ is not detected toward MM7, suggesting MM7 is less evolved than MM8 and MM4. For MM8 and MM4, we note that CH_3OH $v=0$ with 889 K and CH_3OH $v_t=1$ with 771 K are excited at MM4 but absent at MM8. Gas emission of outflow tracers (CS, SO, and SiO, see Figure 7 and 9), along with the spectra of HCO^+ , SiO, and CS lines (Figure 10) which show broader wing structure in the MM8 compared to MM4. All tracers do not show any signature of molecular outflows in MM4. So maybe MM4 is older than MM8.

$\text{H}_{40\alpha}$ recombination line toward MM1 and MM11 indicating that they evolved into an H/UC H II stage. In this phase, molecules are hard to be detected since they are destroyed by UV radiation. Meanwhile hydrogen recombination lines emerge. MM1 is line-poor with only a few simple molecules like CS, SO, and HC_3N $v=0$ detected and is not associated with outflows. However, ionized gas tracer $\text{H}_{40\alpha}$ is observed in this core. MM1 lies $\sim 0.8''$ to the south-east of the H II region C, it is likely that $\text{H}_{40\alpha}$ line is from the envelope of the H II region C. A few COMs emission still exist in the MM11 region, meanwhile $\text{H}_{40\alpha}$ and $\text{H}_{50\beta}$ lines are excited.

In spite of different phases presenting different physical conditions, it should be noted that during the star-forming process, different evolutionary stages show a vague boundary, and they are not fully separable.

Figure 11 shows that the rotational temperatures T_{rot} and molecular abundances (CH_3OH , CH_3OCHO , $\text{C}_2\text{H}_5\text{OH}$, $\text{C}_2\text{H}_5\text{CN}$, CH_2CO , CH_3OCH_3 , CH_3COCH_3 , and CH_3SH) vary with evolutionary stage. This figure only present those parameters that have been derived via LTE fitting to uncontaminated molecules. The mean values of the two parameters are: $T_{\text{rot}} = 99 \pm 28$ K, $\chi = (3.0 \pm 1.2) \times 10^{-8}$ for

MM7, $T_{\text{rot}} = 134 \pm 27$ K, $\chi = (1.0 \pm 0.2) \times 10^{-7}$ for MM8, $T_{\text{rot}} = 137 \pm 21$ K, $\chi = (6.9 \pm 1.7) \times 10^{-7}$ for MM4, and $T_{\text{rot}} = 100 \pm 18$ K, $\chi = (7.4 \pm 2.6) \times 10^{-8}$ for MM11. The data points of molecules (e.g., CH_3CHO and CH_3OCH_3 in MM7) for which column density is derived under the fixed rotational temperature are excluded from the figure. The molecular excitation temperature was adopted to be the gas temperature for each core. Among the four regions, the temperature of MM8/hot-core is similar to MM4/evolved-hot-core, which is higher than those of MM7/early-hot-core and MM11/UC H II . MM7 should not have a comparatively hotter environment because it has not evolved into typical hot core phase. Methanol in torsional state was observed toward MM4 containing three transition lines with E_u up to 340–902 K, which trace very hot and dense region. So the highest temperature appears toward the MM4. MM11/UC H II is slightly colder than MM8 and MM4, which is due to the colder and outer part of the gas components traced by CH_3OCHO , CH_3OCH_3 and H_2CCO . From the Figure 11 and Table 2, one can see that MM4/evolved-hot-core has higher abundances of O-bearing species than other regions, while the highest abundance of $\text{C}_2\text{H}_5\text{CN}$ is seen in MM8. Methanol in ground and torsional states has high abundance $\sim 2.5 \times 10^{-6}$, making the mean value of abundance of MM4 to be seven times higher than those of MM8. In brief, molecular abundance increases with increasing age, except in the last phase MM11 which shows a decrease in abundance probably due to the destruction of molecules by the UV radiation. The molecular abundances increasing with evolution were also found by Gerner et al. (2014) and Coletta et al. (2020).

5.3 Chemical differentiation

5.3.1 Chemical Differentiation between Nitrogen-bearing and Oxygen-bearing species

Chemical differentiation between N-bearing and O-bearing species was found both in high-mass star-forming regions such as Orion KL (Friedel & Snyder 2008; Wang et al. 2009; Crockett et al. 2015), W3(OH) (Wyrowski et al. 1999; Qin et al. 2015), W75N (Remijan et al. 2004b), and G19.61-0.23 (Qin et al. 2010), and in low-mass star-forming regions such as IRAS 16293–2422 (Kuan et al. 2004). These results imply that N-bearing and O-bearing molecules mainly exist in different environments. Our spectral line survey further revealed that the chemical difference between N-bearing and O-bearing molecules also exists in G9.62+0.19. While O-bearing molecules such as CH_3OH , CH_3OCHO , $\text{C}_2\text{H}_5\text{OH}$, and CH_3OCH_3 mostly associated with MM4 (see Figure 5), the strongest emission peaks of N-bearing species $\text{C}_2\text{H}_5\text{CN}$ and HC_3N are located toward the MM8 (see Figure 6). The derived abundances shows that MM4 is an O-rich source, while MM8 is rich in N-bearing species. This result is consistent with the previous interferometric observations that $\text{C}_2\text{H}_5\text{CN}$ emission is the strongest toward the region F (MM8) whereas CH_3OCHO and CH_3OCH_3 are the brightest toward the region E (MM4) (Su et al. 2005).

The N- and O-bearing difference may arise because of different physical properties (initial temperature) during the gravitational collapse phase (Caselli et al. 1993; Yamamoto 2017). As predicted by chemical models, the relatively low initial temperature (lower than 20 K) at molecular accretion phase could keep CO for a long duration on the grain surface and thus may produce O-bearing molecules by the hydrogenation of CO. In contrast, if the temperature at this phase is as high as 40 K (Caselli et al. 1993), grain surface CO could be easily desorbed to the gas phase, leading to the formation of more N-bearing COMs compared to the O-bearing species. Furthermore,

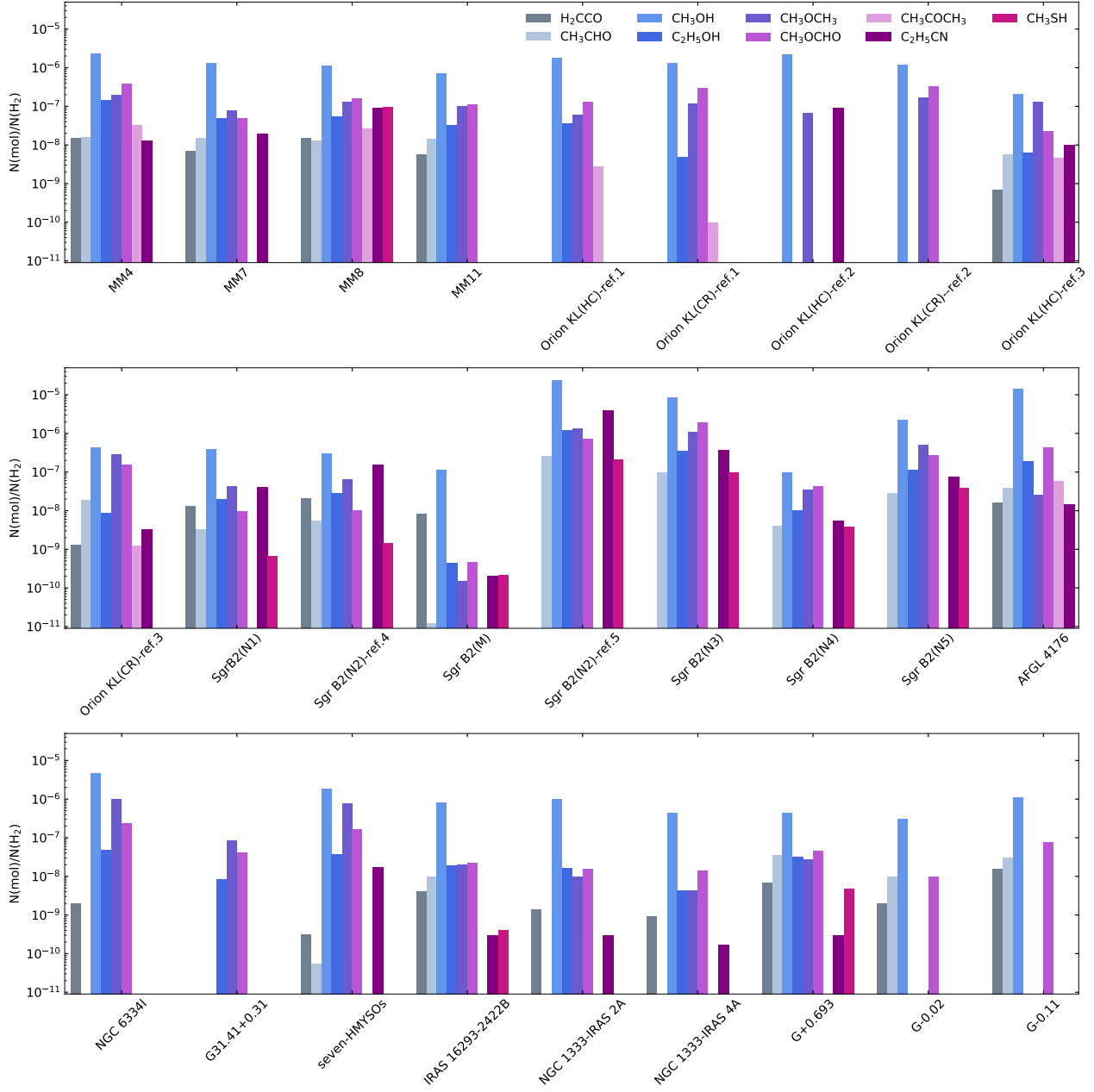


Figure 8. Abundances of COMs relative to H₂ toward four dense cores of G9.62+0.19 and other sources listed in Table 5. The sources labeled as Orion KL (HC)-ref.1 and Orion KL (CR)-ref.1 refer to that the observed results are from Reference 1 in Table 5. Same for Orion KL (HC)-ref.2, Orion KL (CR)-ref.2, Orion KL (HC)-ref.3, Orion KL (CR)-ref.3, Sgr B2(N2)-ref.4 and Sgr B2(N2)-ref.5.

apart from the desorption of CO, a more important process is that atomic hydrogen is quickly desorbed from the dust grain surface. This hinders the formation of O-bearing species. In contrast, atoms C and N easily migrate on dust grain surface, forming C_nN and thus initiate the N-bearing COM chemistry. A consistent findings from recent work (Wang et al., in preparation) also presented that the initial temperature of 15 K and 23 K at collapse phase can produce abundant O-bearing and N-bearing species, respectively. Considering that the MM8 region could be externally heated at the gravitationally collapse phase due to its proximity to H II "B", its initial temperature at accretion phase is likely to be higher than that of

MM4. The N/O variation seen in MM8 and MM4 is very likely to be caused by the different initial environments of these two cores.

5.3.2 Chemical relationships of Oxygen-bearing molecules

Chuang et al. (2021) suggest that COMs described by the formula C₂H_nO₂ (n=4 and 6) may have similar formation routes. COMs with formula C₂H_nO (n=2, 4 and 6) are also chemical links through hydrogenation reaction on interstellar grains: H₂CCO $\xrightarrow{2\text{H}}$ CH₃CHO $\xrightarrow{2\text{H}}$ C₂H₅OH (Charnley & Rodgers 2005). In our work, C₂H_nO family such as H₂CCO, CH₃CHO, C₂H₅OH, and CH₃OCH₃, C₂H_nO₂ family like CH₃OCHO, and CH₃OH which is

Table 6. Evolutionary stage for each core.

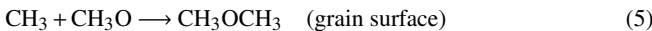
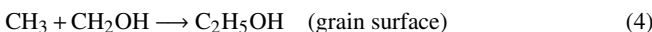
Position	Molecular species or continuum emission	Line kinematic property	Stage
MM6	simple molecules; COMs (only one CH ₃ OH transition)	collimated outflow	HMPOs
MM7	rich COMs; no vibrationally or torsionally excited states of molecules	molecular outflows	early HMCs
MM8	rich COMs; vibrationally excited state of H ₃ CN, torsionally excited states of CH ₃ OH and CH ₃ OCHO	molecular outflows	HMCs
MM4	rich COMs; CH ₃ OH v=0 and CH ₃ OH v ₁ =1 with higher upper energy level; centimeter continuum emission ^a	no molecular outflows	evolved HMCs
MM11	H _{40α} , H _{50β} ; a few COMs; centimeter continuum emission ^a	no molecular outflows	HMCs/UC HII region
MM1	line-poor; H _{40α}	no molecular outflows	evolved HII region

Notes. ^a Testi et al. (2000)

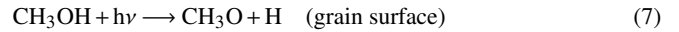
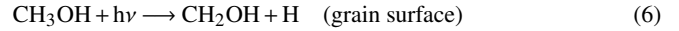
considered as the precursor of some larger O-bearing COMs (e.g., C₂H₅OH, CH₃OCH₃, and CH₃OCHO) (Blake et al. 1987; Öberg et al. 2009; Maity et al. 2015; Bergantini, Maksyutenko & Kaiser. 2017) are simultaneously detected. In order to explore possible chemical links among O-bearing molecules, we compare the column density of several molecules (see Figure 12), as the formation process of COMs can be tested by investigating how their abundances/column densities are related.

Moreover, comparisons of the very limited sample can not testify the potential chemical link among species well. We included more observing results from HMSFRs, to LMSFRs and GCMCs as listed in Table 5. Since column densities of these O-bearing COMs have been derived from various observational equipments with different spatial resolution and spectral setup, comparison of column density is not very helpful to derive sound conclusions for chemical links among O-bearing COMs. It is more reliable to compare the abundance of COMs relative to CH₃OH. The column density ratios between O-bearing species and CH₃OH from other types of sources in Table 5 are plotted in Figure 13. By the analyses of the molecular relationship in our four dense cores (see Figure 12), together with molecules from literature (see Figure 13), the main points for possible chemical correlations between specific molecules are discussed as follows:

(1) **CH₃OH/C₂H₅OH, CH₃OH/CH₃OCH₃:** The preliminary results from Figure 12 reveal that there is a tight positive correlation between CH₃OH and C₂H₅OH, and also the positive correlation between CH₃OH and CH₃OCH₃, is suggestive of similar formation route for both the species. Here, the synthesis of C₂H₆O isomers ethanol (C₂H₅OH) and dimethyl ether (CH₃OCH₃) has great potential via radical-radical recombination that the hydroxymethyl radical (CH₂OH) and methoxy radical (CH₃O) react with methyl radical (CH₃) (Maity et al. 2015).

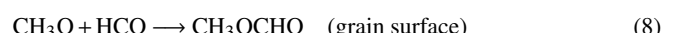


The productions of hydroxymethyl radical (CH₂OH) and methoxy radical (CH₃O) through unimolecular decomposition of methanol have been identified in Bennett & Kaiser (2007); Bennett et al. (2007). Then the main path to produce the radical CH₃O and CH₂OH would likely be the photodissociation process as follows:



The spatial distributions of CH₃OH, CH₃OCH₃, and C₂H₅OH that are mainly shown toward the MM4, MM7, MM8, and MM11, suggest that C₂H₅OH and CH₃OCH₃ might have a common precursor, CH₃OH. Correlation coefficient of 0.89 for CH₃OH/CH₃OCH₃ toward G10.6-0.4 (Law et al. 2021) and 0.86 for CH₃OH/CH₃OCH₃ and CH₃OH/C₂H₅OH toward seven high-mass hot cores (Bisschop et al. 2007) also support that C₂H₅OH and CH₃OCH₃ are tightly correlated with CH₃OH.

(2) **CH₃OCHO and CH₃OCH₃:** Column densities between CH₃OCHO and CH₃OCH₃, from each type of core, are also correlated (see Figure 12). Moreover, abundances of CH₃OCHO and CH₃OCH₃ relative to CH₃OH (see Figure 13) from three kinds of objects present the positive correlation. The tight correlation of CH₃OCHO and CH₃OCH₃ was presented from Bisschop et al. (2007); Brouillet et al. (2013); Coletta et al. (2020) as well. The molecular abundance ratio between CH₃OCHO and CH₃OCH₃ is found to be ~1 in different type of source including high-mass star-forming regions (e.g., Bisschop et al. 2007; Brouillet et al. 2013; Rivilla et al. 2017b; Law et al. 2021), intermediate-mass star-forming regions (Ospina-Zamudio et al. 2018), hot corinos (Taquet et al. 2015), Galactic centre clouds (Requena-Torres et al. 2006) and protostellar shock region (Lefloch et al. 2017). However, the ratio is reported to be ~2 for prestellar cores (Jiménez-Serra et al. 2016) and Comets (Biver & Bockelée-Morvan 2019). In our work, ratios are estimated to be 0.6±0.3, 1.3±0.1, 2.0±0.3, and 1.1±0.5 toward the MM7, MM8, MM4, and MM11, respectively. In addition, our 3 mm observations showed that CH₃OCHO and CH₃OCH₃ have similar gas distributions. These observation results may imply a potential link between these two species, which shares common precursor methoxy radical (CH₃O) through reactions (8) and (9) (Garrod & Herbst. 2006; Garrod et al. 2008; Öberg et al. 2010), protonated methanol CH₃OH₂⁺ with reactions (10) and (11) (Blake et al. 1987), or production of CH₃OCHO from CH₃OCH₃ via the sequence (12) (Balucani et al. 2015):



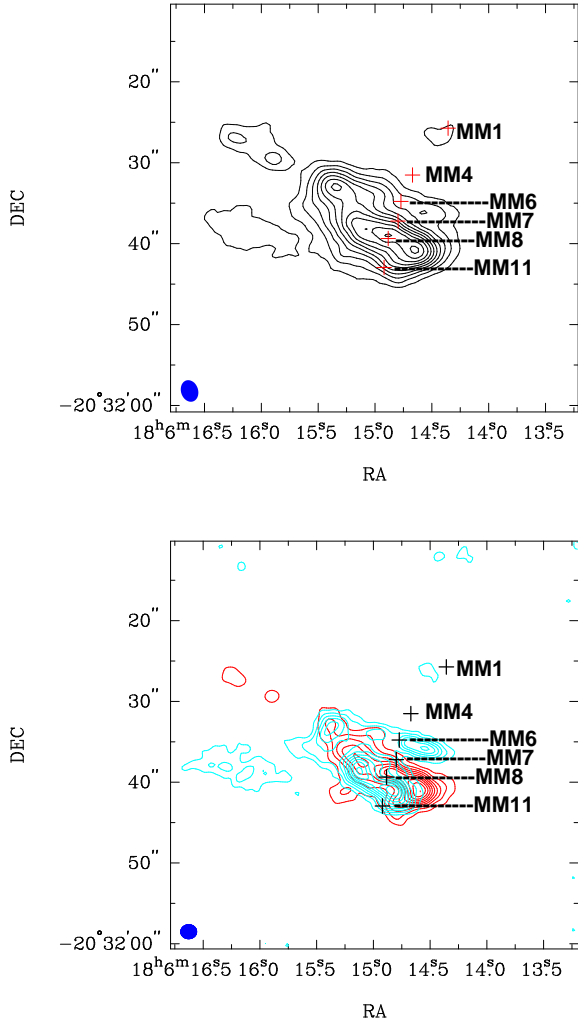
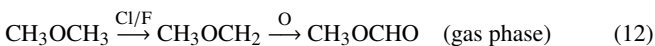
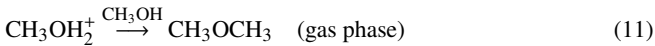
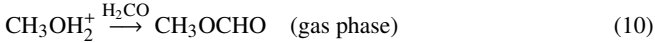


Figure 9. Upper panel: Integrated intensity (-15 to 45 km s^{-1}) of SiO (2–1) observed by ALMA 12-m+ACA combined data. The contours are $(10\%, 20\%, 30\%, 40\%, 50\%, 60\%, 70\%, 80\%, 90\%, 98\%) \times 5.3$ Jy/beam km s^{-1} . Lower panel: SiO outflow observed by 12-m array. The cyan contours represent blueshifted gas with LSR velocities ranging from -15 to -2 km s^{-1} . The red contours represent redshifted emission with velocities 12 to 43 km s^{-1} . The synthesized beam is shown in the bottom left corner. The contours are $(10\%, 20\%, 30\%, 40\%, 50\%, 60\%, 70\%, 80\%, 90\%, 100\%) \times 3.6$ Jy/beam km s^{-1} . The names of the six densest cores are labeled.



(3) $\text{C}_2\text{H}_n\text{O}_2$ family: The correlation plots (see Figure 12)

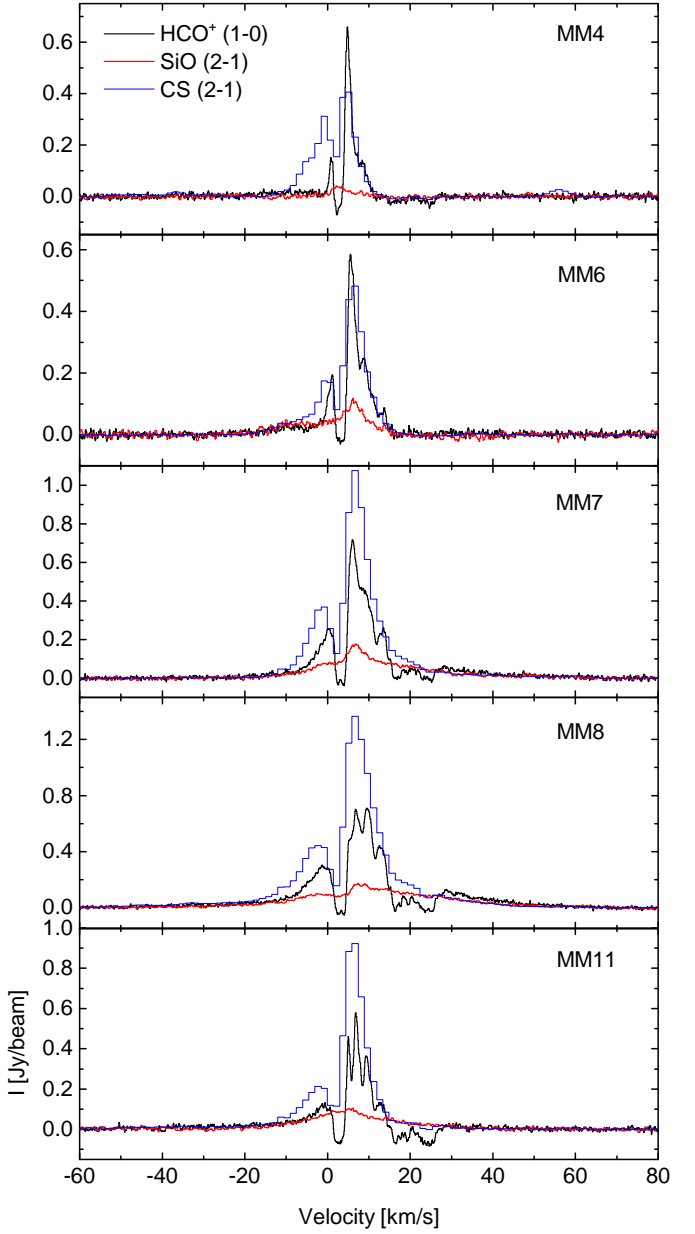


Figure 10. Beam-averaged spectra of HCO^+ (1–0), SiO (2–1), and CS (2–1) at five protostellar cores, observed by 12-m and ACA combined data.

for each pair of $\text{H}_2\text{CCO}/\text{CH}_3\text{CHO}$, $\text{H}_2\text{CCO}/\text{C}_2\text{H}_5\text{OH}$, and $\text{H}_2\text{CCO}/\text{CH}_3\text{OCH}_3$ showed that there is no clear relationship between H_2CCO and other $\text{C}_2\text{H}_n\text{O}$ group molecules. The gas distribution of CH_3CHO extend to east, which shows that the emission of CH_3CHO is not very similar to H_2CCO and $\text{C}_2\text{H}_5\text{OH}$. These results challenge the prediction that COMs in the formula of $\text{C}_2\text{H}_n\text{O}$ have chemical correlation. Figure 13 shows a positive correlations between $\text{N}(\text{H}_2\text{CCO})/\text{N}(\text{CH}_3\text{OH})$ and $\text{N}(\text{C}_2\text{H}_5\text{OH})/\text{N}(\text{CH}_3\text{OH})$, and weak correlation between $\text{N}(\text{H}_2\text{CCO})/\text{N}(\text{CH}_3\text{OH})$ and $\text{N}(\text{CH}_3\text{OCH}_3)/\text{N}(\text{CH}_3\text{OH})$. The chem-

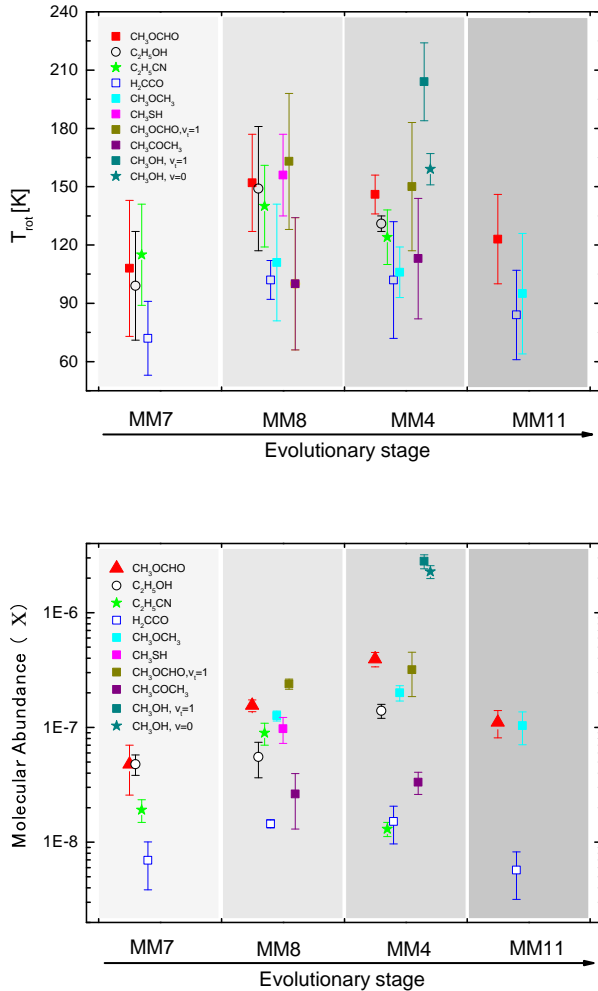


Figure 11. The rotational temperatures (upper) and molecular abundances (lower) of eight species (CH_3OH (in ground state ($v=0$) and torsionally excited state ($v_t=1$)), CH_3OCHO (in $v=0$ and $v_t=1$), $\text{C}_2\text{H}_5\text{OH}$, $\text{C}_2\text{H}_5\text{CN}$, H_2CCO , CH_3OCH_3 , CH_3COCH_3 , and CH_3SH) from four dense cores.

ical links among molecules in $\text{C}_2\text{H}_n\text{O}$ formula cannot be determined at the moment.

(4) CH_3OCHO and CH_3CHO : Although Figure 12 and Figure 13 showed another possible chemical link between CH_3OCHO and CH_3CHO , gas distributions of CH_3OCHO are considerably different from those of CH_3CHO . The chemical correlation between them should be further investigated.

To better characterize the chemical properties, more samples in various astrochemical environments and future chemical models are needed. In the near future, we are on track to study the chemistry of the COMs by considering more sources observed in the ATOMS project. In addition, these sources belong to different evolutionary stages so that we can draw a general picture on the properties of the COMs revealed from these sources. This will help us to set strong constraints on the chemical networks.

5.3.3 Chemical relationships of Nitrogen-bearing molecules

Hot core tracers (HC_3N and its vibrationally excited lines) found to be abundant with the evolution of the center protostar (Bergin et al. 1996; Taniguchi et al. 2019; Zhang et al. 2021). Earlier, longer chain cyanopolyyne HC_{2n+1}N ($n>2$) have been thought to be detected in the early stage of star formation and absent in protostellar cores (e.g., Suzuki et al. 1992; Hirota et al. 2009). Recent observations found that longer cyanopolyyne have been detected in hot cores (e.g., Belloche et al. 2013; Esplugues et al. 2013; Green et al. 2014; Taniguchi et al. 2017, 2018). Previous papers proposed that cyanopolyyne are efficiently formed via the neutral–neutral reaction " $\text{C}_{2n}\text{H}_2 + \text{CN} \rightarrow \text{HC}_{2n+1}\text{N} + \text{H}$ " in the warm region (e.g., Chapman et al. 2009; Taniguchi et al. 2019). HC_5N also can be formed via the reaction " $\text{CCH} + \text{HC}_3\text{N} \rightarrow \text{HC}_5\text{N} + \text{H}$ " in the gas phase (Taniguchi et al. 2019). At low temperature, the route " $\text{N} + \text{C}_{n+1}\text{H} \rightarrow \text{HC}_n\text{N} + \text{C}$ ", where $n = 3, 5, 7$, is thought to significantly contribute to the formation of cyanopolyyne. Recently, it has been suggested that $\text{HC}_5\text{N}/\text{HC}_3\text{N}$ abundance ratios in the cold objects are higher than those in massive hot cores (Jaber et al. 2017). So, there exists contradiction between HC_5N and HC_3N in production rates. The formation mechanism of cyanopolyyne is not fully understood by now.

In our work, Figure 6 shows the integrated intensity maps of HC_3N $v=0$, and its isotopes, and HC_3N in vibrationally excited state $v_t=1$ all peak at the position of the continuum peak. However, the distribution of HC_5N has its own unique characteristics which differ from the distributions of HC_3N . Therefore, it seems that HC_5N is not generated from HC_3N . Fontani et al. (2017) studied the intermediate mass protocluster OMC-2 FIR4, and found that the spatial distribution of HC_3N is not coincident with that of HC_5N , namely that HC_3N emission is associated with the continuum peak FIR4, HC_5N distributes over the eastern part of the continuum peak. They proposed that enhanced cosmic-ray ionisation rate will promote the production of HC_5N . For HC_5N in G9.62+0.19, the line intensity ratio between MM3 and MM4 is about 1.3, while for HC_3N the ratio is around 0.5. Additionally, MM3 and MM4 are supposed to be at starless core and evolved HMCs stage, respectively. This imply that the synthesis of HC_5N is different from HC_3N in the early stage. The neutral–neutral reaction between C_4H_2 and CN may not be the formation pathway of HC_5N in G9.62+0.19, which support the idea that formation mechanisms of HC_3N and HC_5N may differ in various interstellar environments (Taniguchi et al. 2019).

In addition, the distribution of $\text{C}_2\text{H}_5\text{CN}$ (see Figure 6) is almost identical to that of HC_3N , predicting that $\text{C}_2\text{H}_5\text{CN}$ is correlated with HC_3N in formation mechanism (e.g., hydrogenation of HC_3N on grain surface to form $\text{C}_2\text{H}_5\text{CN}$).

6 CONCLUSIONS

We have performed line survey using ALMA 3 mm observations toward the complex massive star-forming region. The detailed line modeling and analysis show that there exhibit chemical differentiation in this region. The main results are summarised as follows:

1. Six dense cores are detected in 3 mm continuum emission. The molecular richness, kinematics, and physical and chemical properties are different in these dense cores. MM1 is considered as an HII region because it shows $\text{H}_{40\alpha}$ emission. MM6 is at HMPOs with collimated outflow. MM7, MM8, and MM4 are line-rich regions, which are considered to be at HMCs phase. Among them, MM7 is at the earlier stage because of fewer detected molecules and MM4 is at a more evolved stage due to the

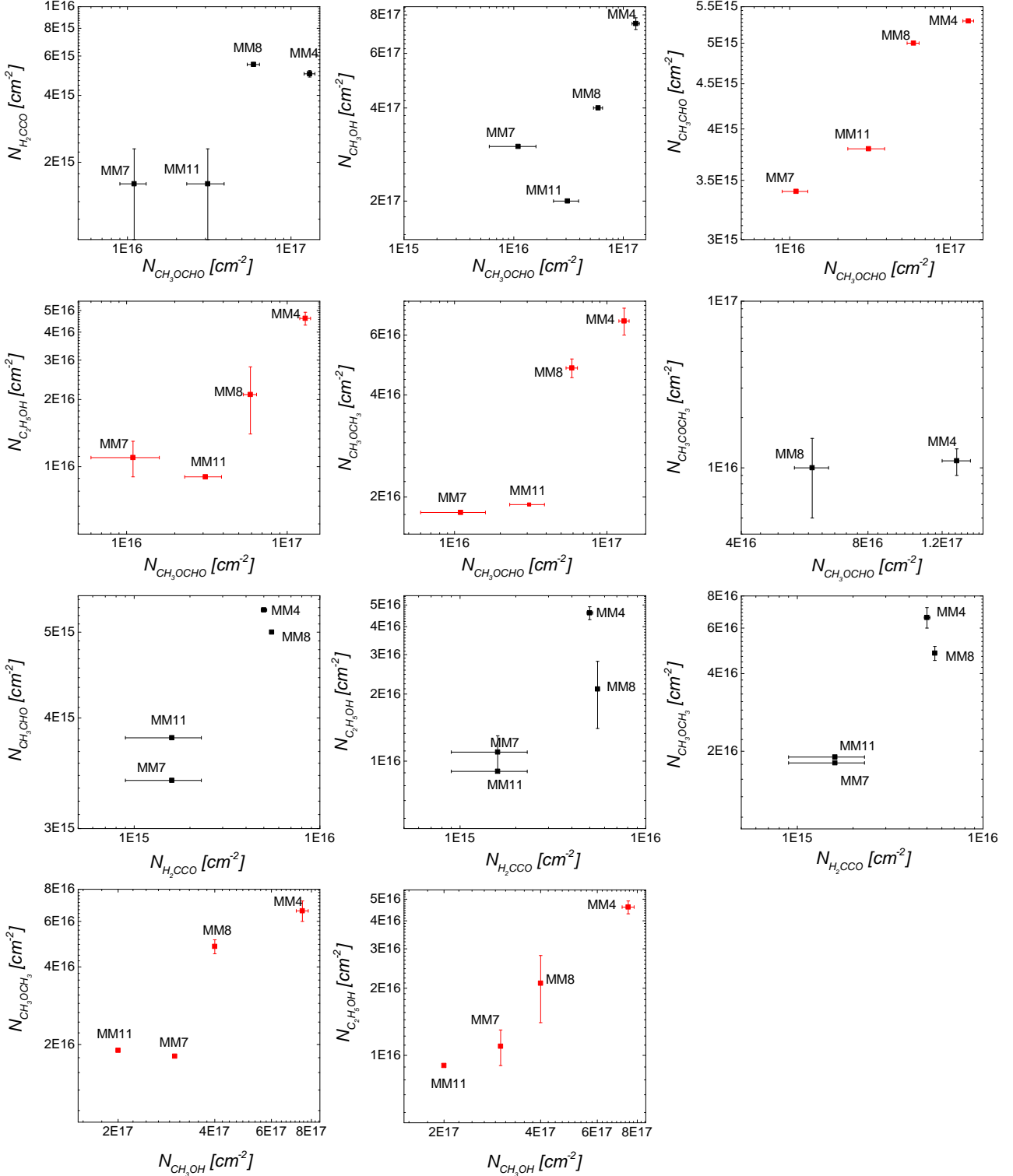


Figure 12. Comparison between the column densities of O-bearing species toward four cores MM7, MM8, MM4, and MM11. The point with error bar means that this value is obtained from model fitting, while one without error bar represents that the value derived by assuming a fixed rotational temperature and source size. The data points with red denote the possible chemical links between $\text{CH}_3\text{OCHO}/\text{CH}_3\text{CHO}$, $\text{CH}_3\text{OCHO}/\text{C}_2\text{H}_5\text{OH}$, $\text{CH}_3\text{OCHO}/\text{CH}_3\text{OCH}_3$, $\text{CH}_3\text{OH}/\text{CH}_3\text{OCH}_3$, and $\text{CH}_3\text{OH}/\text{C}_2\text{H}_5\text{OH}$.

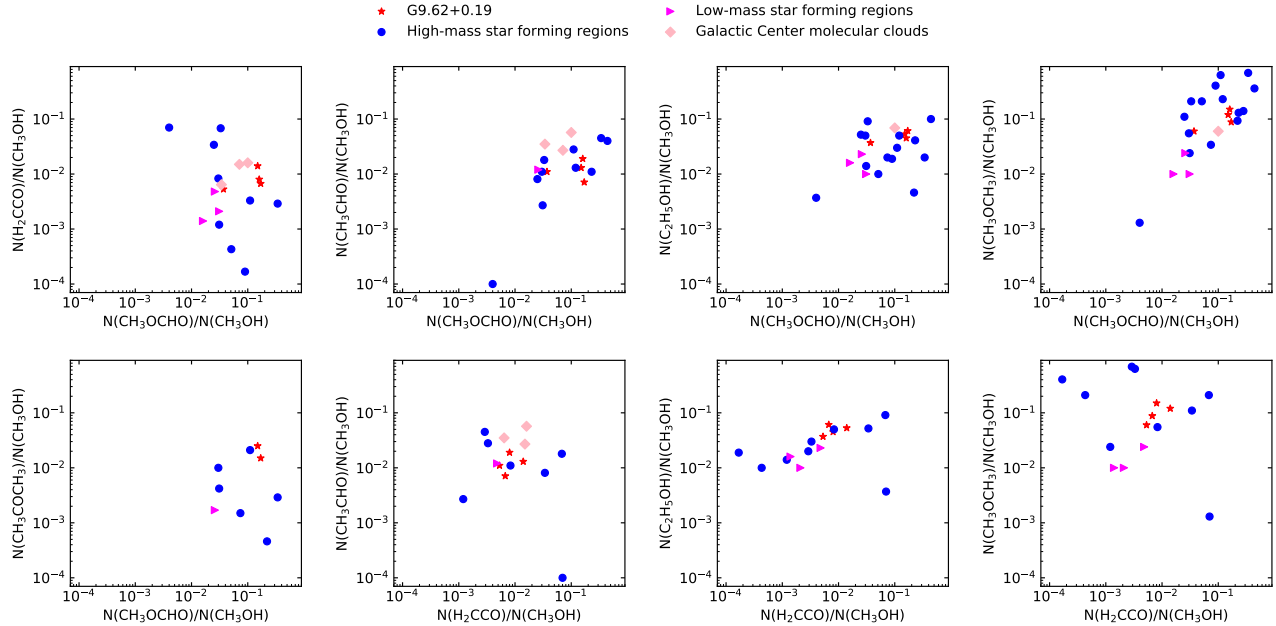


Figure 13. Comparison of the column density ratios with respect to CH_3OH between O-bearing species for the sources listed in Table 5.

absence of outflows. MM11 shows a combination of HMCs and UC H α region, as it has the detection of COMs (such as CH_3CHO , CH_3OCHO , CH_3OCH_3 , and $\text{C}_2\text{H}_5\text{OH}$), and hydrogen recombination lines such as $\text{H}_{40\alpha}$ and $\text{H}_{50\beta}$. In short, their evolutionary sequence is MM6 → MM7 → MM8 → MM4 → MM11 → MM1.

2. Modeling of the detected spectral lines, we have derived rotational temperatures from 72 to 115 K toward MM7, 100 to 163 K toward MM8, 102 to 204 K toward MM4, and 84 to 123 K toward MM11. Molecular column densities are on the orders of $10^{15} - 10^{16} \text{ cm}^{-2}$ toward MM7, MM8, and MM11, $10^{15} - 10^{17} \text{ cm}^{-2}$ toward MM4.

3. The emission of N-bearing and S-bearing molecules is strongest toward MM8, while emission of O-bearings is dominated by core MM4. Besides, the largest abundances of N-bearing and O-bearing molecules appear in MM8 and MM4, respectively. These all indicate clear chemical differentiation of N/O between MM8 and MM4. Such chemical differentiation might be affected by different initial temperature toward the MM8 and MM4 at their accretion phase.

4. We found tight correlations between the column density of molecular pairs $\text{CH}_3\text{OH}/\text{C}_2\text{H}_5\text{OH}$, $\text{CH}_3\text{OH}/\text{CH}_3\text{OCH}_3$, and $\text{CH}_3\text{OCHO}/\text{CH}_3\text{OCH}_3$. Furthermore, the similar spatial distribution between them is seen, indicating that each pair is likely chemically linked, and may share a common precursor. The gas distribution of CH_3CHO is less correlated to H_2CCO and $\text{C}_2\text{H}_5\text{OH}$. Their column density/abundance correlations are not very clear. It seems likely that the chemical link of O-bearing COMs in the formula $\text{C}_2\text{H}_n\text{O}$ is uncertain at present work.

5. The comparison of HC_3N and HC_5N suggests that they trace different gas structures, and the formation mechanisms of HC_3N and HC_5N may differ in hot and cold regions.

ACKNOWLEDGEMENTS

This paper makes use of the following ALMA data: ADS/JAO.ALMA#2019.1.00685.S. ALMA is a partnership of ESO (representing its member states), NSF (USA), and NINS (Japan), together with NRC (Canada), MOST and ASIAA (Taiwan), and KASI (Republic of Korea), in cooperation with the Republic of Chile. The Joint ALMA Observatory is operated by ESO, AUI/NRAO, and NAOJ. This work has been supported by the National Key R&D Program of China (No. 2017YFA0402701), by the National Natural Science Foundation of China (NSFC) under grant No.12033005 and No.11947064, and Yunnan Applied Basic Research Projects under grant No.202001AU070123. Tie Liu acknowledges the supports by National Natural Science Foundation of China (NSFC) through grants No.12073061 and No.12122307, the international partnership program of Chinese academy of sciences through grant No.114231KYSB20200009, and Shanghai Pujiang Program 20PJ1415500. H.-L. Liu is supported by NSFC through the grant No.12103045. G.G. and L.B. gratefully acknowledge support from ANID BASAL project FB210003. C.W.L is supported by the Basic Science Research Program (2019R1A2C1010851) through the National Research Foundation of Korea. D.L. Li acknowledges support from NSFC through grants No.12173075 and support from Youth Innovation Promotion Association CAS. K.T. was supported by JSPS KAKENHI Grant Number 20H05645. Mengyao Tang is supported by the scientific research fund project of Yunnan Provincial Education Department (No. 2022J0855). YZ thanks the National Science Foundation of China (NSFC, Grant No. 11973099) and the science research grants from the China Manned Space Project (NO. CMS-CSST-2021-A09 and CMS-CSST-2021-A10) for financial supports.

Best

Data availability

The data underlying this article are available in the ALMA archive.

REFERENCES

- Abplanalp, M. J., Gozem, S., & Krylov, A. I. 2016, *PNAS*, 113, 7727
- Agúndez, M., Marcelino, N., Tercero, B., Cabezas, C., de Vicente, P., Cernicharo, J. 2021, *A&A*, 649, 4
- Bacmann, A., Taquet, V., Faure, A., Kahane, C., & Ceccarelli, C. 2012, *A&A*, 541, L12
- Bally, J., Moeeckel, N., & Throop, H. Evolution of UV-Irradiated Protoplanetary Disks. Chondrites and the Protoplanetary Disk, ed. Alexander N. Krot, Edward R. D. Scott, & Bo Reipurth. ASP Conference. 2005, Ser. 341: 81
- Balucani, N., Ceccarelli, C., & Taquet, V. 2015, *MNRAS*, 449, L16
- Belloche, A., Müller, H. S. P., Menten, K. M., Schilke, P., & Comito, C. 2013, *A&A*, 559, A47
- Belloche, A., Müller, H. S. P., Garrod, R. T., Menten, K. M. 2016, *A&A*, 587, A91
- Belloche, A., Meshcheryakov, A. A., Garrod, R. T., Ilyushin, V. V., Alekseev, E. A., Motylenko, R. A., Margulés, L., Müller, H. S. P., et al. 2017, *A&A*, 601, A49
- Beltrán, M. T., Massi, F., López, R., Girart, J. M., & Estalella, R. 2009, *A&A*, 504, 97
- Bennett, Chris J., & Kaiser, Ralf I. 2007, *ApJ*, 661, 899
- Bennett, Chris J., Chen, Shih-Hua., Sun, Bing-Jian., et al. 2007, *ApJ*, 660, 1588
- Bergantini, Alexandre., Maksyutenko, Pavlo., Kaiser, Ralf I. 2017, *ApJ*, 841, 96
- Bergner, J. B., Oberg, K. I., & Rajappan, M. 2017, *ApJ*, 845, 29
- Bergin, E. A., Snell, R. L., & Goldsmith, P. F. 1996, *ApJ*, 460, 343
- Bisschop, S. E., Jørgensen, J. K., van Dishoeck, E. F., & de Wachter, E. B. M. 2007, *A&A*, 465, 913
- Biver, N. & Bockelée-Morvan, D. 2019, *ACS Earth and Space Chemistry*, 3, 1550
- Blake, Geoffrey A., Sutton, E. C., Masson, C. R., Phillips, T. G. 1987, *ApJ*, 315, 621
- Bøgelund, Eva G., McGuire, Brett A., Ligterink, Niels F. W. et al. 2018, *A&A*, 615, A88B
- Bøgelund, E. G., Barr, A. G., Taquet, V., et al. 2019, *A&A*, 628, A2
- Bonfand, M., Belloche, A., Garrod, R. T., et al. 2019, *A&A*, 628, 27
- Brouillet, N., Despois, D., Baudry, A., et al. 2013, *A&A*, 550, 46
- Caselli, P., Hasegawa, T. I., & Herbst, E. 1993, *ApJ*, 408, 548
- Cernicharo, J., Kisiel, Z., Tercero, B., et al. 2016, *A&A*, 587, 4
- Charnley, S. B., & Rodgers, S. D. 2005, *IAU Symp.*, 231, 237
- Chapman, J. F., Millar, T. J., Wardle, M., et al. 2009, *MNRAS*, 394, 221
- Chuang, K. -J., Fedoseev, G., Scirè, C., et al. 2021, *A&A*, 650, A85
- Coletta, A., Fontani, F., Rivilla, V. M., et al. 2020, *A&A*, 641, 54
- Colzi, L., Rivilla, V. M., Beltrán, M. T., et al. 2021, *A&A*, 653, A129
- Crockett, N. R., Bergin, E. A., Neill, J. L., et al. 2014, *ApJ*, 787, 112
- Crockett, N. R., Bergin, E. A., Neill, J. L., Favre, C., Blake, G. A., et al. 2015, *ApJ*, 806, 239
- Dall’Olio, D., Vlemmings, W. H. T., Persson, M.V., et al. 2019, *A&A*, 626, 36
- Dickens, J. E., Irvine, W. M., Snell, R. L., et al. 2000, *ApJ*, 542, 870
- Drozdovskaya, M. N., van Dishoeck, E. F., Rubin, M., Jørgensen, J. K., Altwegg, K. 2019, *MNRAS*, 490, 50
- Duronea, N. U., Bronfman, L., Mendoza, E., et al. 2019, *MNRAS*, 489, 1519
- Esplugues, G. B., Cernicharo, J., Viti, S., et al. 2013, *A&A*, 559, A51
- Favre, C., Despois, D., Brouillet, N., et al. 2011, *A&A*, 532, A32
- Feng, S., Beuther, H., Henning, T., et al. 2015, *A&A*, 581, A71
- Fontani, F., Ceccarelli, C., Favre, C., et al. 2017, *A&A*, 605, A57
- Frau, P., Girart, J. M., Beltrán, M. T., et al. 2010, *ApJ*, 723, 1665
- Friedel, D. N., & Snyder, L. E. 2008, *ApJ*, 672, 962
- Garay, G., Rodriguez, L. F., Moran, J. M., & Churchwell, E. 1993, *ApJ*, 418, 368
- Garrod, R. T., & Herbst, E. 2006, *A&A*, 457, 927
- Garrod, R. T., Weaver, S. L. W., & Herbst, E. 2008, *ApJ*, 682, 283
- Gerner, T., Beuther, H., Semenov, D., et al. 2014, *A&A*, 563, 97
- Gibb, E., Nummelin, A., Irvine, W. M., et al. 2000, *ApJ*, 545, 309
- Gieser, C., Beuther, H., Semenov, D., et al. 2021, *A&A*, 648, 66
- Goldsmith, Paul F. 2001, *ApJ*, 557, 736
- Gorai, Prasanta., Das, Ankan., Shimonishi, Takashi., et al. 2021, *ApJ*, 907, 108
- Green, C.-E., Green, J. A., Burton, M. G., et al. 2014, *MNRAS*, 443, 2252
- Hasegawa, T. I., Herbst, E., Leung, C. M. 1992, *ApJS*, 82, 167
- Herbst, E., & van Dishoeck, E. F. 2009, *ARA&A*, 47, 427
- Hervías-Caimapo, Carlos., Merello, Manuel., Bronfman, Leonardo., et al. 2019, *ApJ*, 872, 200
- Hirota, T., Ohishi, M., & Yamamoto, S. 2009, *ApJ*, 699, 585
- Hoare, M. G., Kurtz, S. E., Lizano, S., Keto, E., & Hofner, P. 2007, in Protostars and Planets V, ed. B. Reipurth, D. Jewitt, & K. Keil, 181
- Hofner, P., Churchwell, E., Kurtz, S., Cesaroni, R., & Walmsley, C. M. 1994, *ApJ*, 429, L85
- Hofner, P., Wiesemeyer, H., & Henning, T. 2001, *ApJ*, 549, 425
- Jaber, A. A., Ceccarelli, C., Kahane, C., et al. 2017, *A&A*, 597, A40
- Jiménez-Serra, I., Vasyunin, A. I., Caselli, P., et al. 2016, *ApJ*, 830, L6
- Johansson, L. E. B., Andersson, C., Elldér, J., et al. 1984, *A&A*, 130, 227
- Jørgensen, J. K., Schöier, F. L., & van Dishoeck, E. F. 2002, *A&A*, 389, 908
- Jørgensen, J. K., Favre, C., Bisschop, S. E., et al. 2012, *ApJ*, 757, L4
- Jørgensen, J. K., van der Wiel, M. H. D., Coutens, A., et al. 2016, *A&A*, 595, A117
- Jørgensen, J. K., Müller, H.S.P., Calcutt, H., Coutens, A., Drozdovskaya, M. N., et al. 2018, *A&A* 620, A170
- Jørgensen, J. K., Belloche, A., Garrod, R. T. 2020, *ARA&A*, 58, 727
- Kauffmann, J., Bertoldi, F., Bourke, T. L., Evans, N. J. I., & Lee, C. W. 2008, *A&A*, 487, 993
- Kennicutt, R. C. 1998, *ARA&A*, 36, 189
- Kolesniková, L., Tercero, B., Cernicharo, J., et al. 2014, *ApJ*, 784, L7
- Krumholz, M. R., Bate, M. R., Arce, H. G., et al., 2014, *Protostars and Planets VI*, Henrik Beuther, Ralf S. Klessen, Cornelis P. Dullemond, and Thomas Henning (eds.), University of Arizona Press, Tucson, 914pp., p.243-266
- Kuan, Yi-Jehng., Huang, Hui-Chun., Charnley., Steven B., et al. 2004, *ApJ*, 616, L27
- Kurtz, S., Cesaroni, R., Churchwell, E., Hofner, P., & Walmsley, C. M. 2000, in *Protostars and Planets IV*, ed. V. Mannings, A. P. Boss, & S. S. Russell, 299–326
- Kurtz, S., Churchwell, E., & Wood, D. O. S. 1994, *ApJS*, 91, 659
- Laas, J. C., Garrod, R. T., Herbst, E., & Widicus Weaver, S. L. 2011, *ApJ*, 728, 71
- Langer, W. D., & Penzias, A. A. 1990, *ApJ*, 357, 477
- Langer, W. D., & Penzias, A. A. 1993, *ApJ*, 408, 539
- Law, C. J., Zhang, Q., Öberg, K. I., et al. 2021, *ApJ*, 909, 214
- Lee, Jeong-Eun., Lee, Seokho., Baek, Giseon., et al. 2019, *Nature Astronomy*, 3, 314
- Lefloch, B., Ceccarelli, C., Codella, C., et al. 2017, *MNRAS*, 469, L73
- Ligterink, Niels F. W., El-Abd, Samer J., Brogan, Crystal L., Hunter, Todd R., Remijan, Anthony J., Garrod, Robin T., McGuire, Brett M. 2020, *ApJ*, 901, 37
- Lis, D. C., Carlstrom, J. E., & Keene, J. 1991, *ApJ*, 380, 429
- Liu, T., Wu, Y., Liu, S.-Y., et al. 2011, *ApJ*, 730, 102
- Liu, T., Lacy, J., Li, P. k., Wang, K., et al. 2017, *ApJ*, 849, 25
- Liu, Tie., Evans, Neal J., Kim, Kee-Tae., et al. 2020a, *MNRAS*, 496, 2790
- Liu, Tie., Evans, Neal J., Kim, Kee-Tae., et al. 2020b, *MNRAS*, 496, 2821
- Liu, Hong-Li., Liu, Tie., Evans, Neal J., et al. 2021, *MNRAS*, 505, 2801
- Lykke, J. M., Favre, C., Bergin, E. A., et al. 2015, *A&A*, 582, A64
- Maity, S., Kaiser, R. I., & Jones, B. M. 2014, *ApJ*, 789, 36
- Maity, S., Kaiser, R. I., & Jones, B. M. 2015, *PCCP*, 17, 3081
- Majumdar, L., Gratier, P., Vidal, T., et al. 2016, *MNRAS*, 458, 1859
- McGuire, Brett A., Burkhardt, Andrew M., Kalenskii, Sergei., Shingledecker, Christopher N., Remijan, Anthony J., Herbst, Eric., McCarthy, Michael C. 2018, *Science*, 359, 202
- Mininni, C., Beltrán, M. T., Rivilla, V. M., et al. 2020, *A&A*, 644, A84
- Molet, J., Brouillet, N., Nony, T., Gusdorf, A., Motte, F., et al. 2019, *A&A*, 626, A132
- Möller, T., Bernst, I., Panoglou, D., et al. 2013, *A&A*, 549, 21
- Möller, T., Endres, C., Schilke, P. 2017, *A&A*, 598, 7

- Müller, H. S. P., Thorwirth, S., Roth, D. A., & Winnewisser, G. 2001, *A&A*, 370, 49
- Müller, H. S. P., Schlöder, F., Stutzki, J., & Winnewisser, G. 2005, *Journal of Molecular Structure*, 742, 215
- Müller, H.S.P., Belloche, A., Xu, L. et al. 2016, *A&A*, 587, A92
- Nummelman, A., Bergman, P., Hjalmarson, A., et al. 2000, *ApJS*, 128, 213
- Ohishi, M., Kawaguchi, K., Kaifu, N., et al. 1991, in *ASP Conf. Ser.* 16, Atoms, Ions and Molecules: New Results in Spectral Line Astrophysics (San Francisco, CA: ASP), 387
- Öberg, K. I., Garrod, R. T.; van Dishoeck, E. F., Linnartz, H. 2009, *A&A*, 504, 891
- Öberg, K. I., Bottinelli, S., Jørgensen, J. K., & van Dishoeck, E. F. 2010, *ApJ*, 716, 825
- Ospina-Zamudio, J., Lefloch, B., Ceccarelli, C., et al. 2018, *A&A*, 618, A145
- Ossenkopf, V. & Henning, T. 1994, *A&A*, 291, 943
- Peng, Y. P., Qin, S. L., Schilke, P., et al. 2017, *ApJ*, 837, 49
- Pickett, H. M., Poynter, R. L., Cohen, E. A., et al. 1998, *Quant. Spectrosc. & Rad. Transfer*, 60, 883
- Qin, Sheng-Li., Wu, Yuefang., Huang, Maohai., et al. 2010, *ApJ*, 711, 399
- Qin, Sheng-Li., Schilke, Peter., Wu,Jingwen., et al. 2015, *ApJ*, 803, 39
- Requena-Torres, M. A., Martín-Pintado, J., Rodríguez-Franco, A., et al. 2006, *A&A*, 455, 971
- Requena-Torres, M. A., Martí-Pintado, J., Martí, S., & Morris, M. R. 2008, *ApJ*, 672, 352
- Remijan, A., Sutton, E. C., Snyder, L. E., Friedel, D. N., Liu, S. -Y., Pei, C. -C. 2004a, *ApJ*, 606, 917
- Remijan, A., Shiao, Y. S., Friedel, D. N., Meier, D. S., Snyder, L. E. 2004b, *ApJ*, 617, 384
- Richard, C., Margulès, L., Caux, E., et al. 2013, *A&A*, 552, A117
- Rivilla, V. M., Beltrán, M. T., Martín-Pintado, J., Fontani, F., Caselli, P., Cesaroni, R. 2017a, *A&A*, 599, A26
- Rivilla, V. M., Beltrán, M. T., Cesaroni, R., et al. 2017b, *A&A*, 598, A59
- Rodríguez-Almeida, Lucas F., Jiménez-Serra, I., Rivilla, V. M., et al. 2021, *ApJ*, 912, 11
- Ruaud, M., Loison, J. C., Hickson, K. M. et al. 2015, *MNRAS*, 447, 4004
- Ruiterkamp, R., Charnley, S. B., Butner, H. M., et al. 2007, *Ap&SS*, 310, 181
- Sakai, N., & Yamamoto, S. 2013, *ChRv*, 113, 8981
- Sanna, A., Reid, M. J., Moscadelli, L., et al. 2009, *ApJ*, 706, 464
- Shingledecker, C. N., Vasyunin, A., Herbst, E., & Caselli, P. 2019, *ApJ*, 876, 140
- Skouteris, D., Balucani, N., Ceccarelli, C., et al. 2018, *ApJ*, 854, 135
- Suzuki, H., Yamamoto, S., Ohishi, M., et al. 1992, *ApJ*, 392, 551
- Su, Y.-N., Liu, S.-Y., Lim, J., & Chen, H.-R. 2005, in *Conf. Proc. Protostars and Planets V, Submillimeter Observations of the High-mass Star Forming Complex G9.62+0.19 (HI: Waikoloa Village)*, 1286, 8336
- Tan, J. C., Kong, S., Butler, M. J., Caselli, P., & Fontani, F. 2013, *ApJ*, 779, 96
- Taniguchi, Kotomi., Saito, Masao., Hirota, Tomoya., et al. 2017, *ApJ*, 844, 68
- Taniguchi, K., Saito, M., Sridharan, T. K., & Minamidani, T. 2018, *ApJ*, 854, 133
- Taniguchi, K., Herbst, E., Caselli, P., et al. 2019, *ApJ*, 881, 57
- Taquet, V., López-Sepulcre, A., Ceccarelli, C., et al. 2015, *ApJ*, 804, 81
- Tercero, B., Cuadrado, S., López, A., Brouillet, N., Despois, D., Cernicharo, J. 2018, *A&A*, 620, 6
- Testi, Leonardo., Felli, Marcello., Persi, Paolo., & Roth, Miguel. 1998, *A&A*, 329, 233
- Testi, L., Hofner, P., Kurtz, S., & Rupen, M. 2000, *A&A*, 359, L5
- Turner, B. E. 1977, *ApJL*, 213, L75
- Vastel, C., Ceccarelli, C., Lefloch, B., & Bachiller, R. 2014, *ApJL*, 795, L2
- Vasyunin, A. I., & Herbst, E. 2013, *ApJ*, 762, 86
- Wang, K. S., Kuan, Y. J., Liu, S. Y., et al. 2009, *ASPC*, 420.
- Woods, P. M., Slater, B., Raza, Z., et al. 2013, *ApJ*, 777, 90
- Wyrowski, F., Schilke, P., Walmsley, C. M., Menten, K. M. 1999, *ApJ*, 514, 43
- Yamamoto, S. 2017, Introduction to Astrochemistry: Chemical Evolution from Interstellar Clouds to Star and Planet Formation (Berlin: Springer)
- Yan, Y. T., Zhang, J. S., Henkel, C., et al. 2019, *ApJ*, 877, 154
- Zeng, S., Jiménez-Serra, I., Rivilla, V. M., et al. 2018, *MNRAS*, 478, 2962
- Zernickel, A., Schilke, P., Schmiedeke, A., Lis, D. C., Brogan, C. L., et al. 2012, *A&A*, 546, A87
- Zhang, C., Wu, Y., Liu, X. -C., et al. 2021, *A&A*, 648, 83

APPENDIX A: SPECTRA FROM 12-M ARRAY AND 12-M + ACA COMBINED DATA.

Interferometric observations can filter out large scale structure. The combination data from interferometric and single-dish observations sample small-scale components and extended structures simultaneously. In this work, the spectra we used is from 12-m observations alone. We claim that this is safe for our data modeling, because the dense cores of G9.62+0.19 are very compact (see Table 1). The information from these cores are not lost. Figure A1 compare the spectrum of MM8 from 12-m with 12-m + ACA combined data. It exhibited that 2''-averaged spectrum from two observations are very similar in line intensity and line profile (see panel (a) and (b) in Figure A1). Spectrum extracted from 10''area showed that strong lines such as CS and HC₃N appeared minor difference in line intensity(see panel (c) and (d)). This implies that the structures smaller than 10'' are almost unaffected by missing flux, while larger scale structures may be affected. Therefore, 12-m array and combined data have no difference when using them to study the hot core chemistry, but 12-m array data have higher angular resolution for better investigating the compact cores.

APPENDIX B: DETECTED MOLECULAR LINES FROM SIX DENSE CORES.

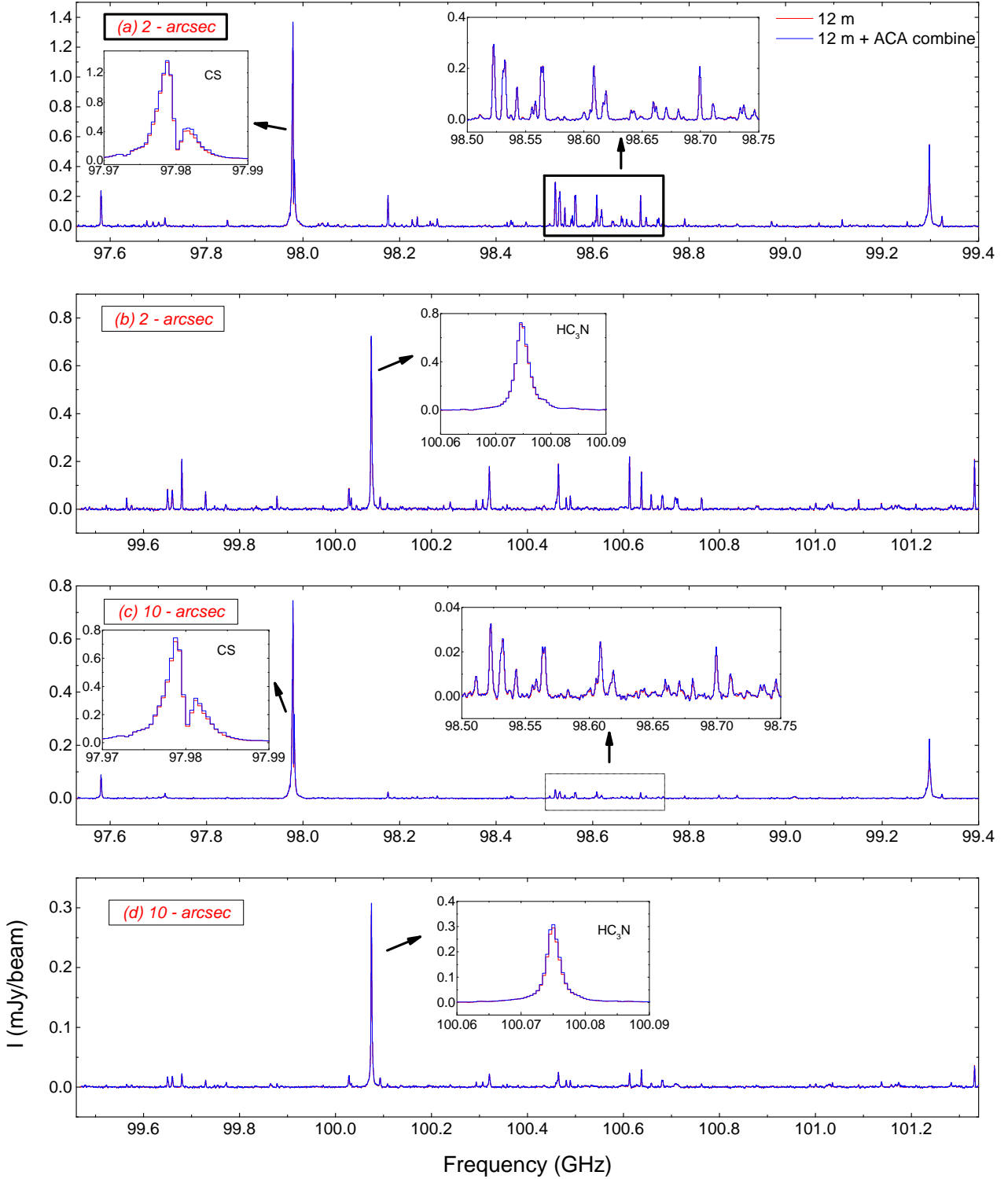


Figure A1. Spectra at the MM8 peak from 12-m array (red) and 12-m + ACA combined data (blue). Spectra in panel (a) and (b) are averaged over 2'' area. Panel (c) and (d) show the averaged spectra over 10''. The frequency range is 97.53 – 99.40 GHz for (a) and (c), while 99.46 – 101.34 GHz for (b) and (d). The zoom-in spectra of CS, HC_3N , and a part of relatively weak lines from 98.50 to 98.75 GHz are also showed.

Table B1: Transitions of detected molecules toward G9.62+0.19

Rest Frequency (GHz)	Quantum Numbers ^a	$S_{ij}\mu^2$ (Debye ²)	E _u (K)	Line Optical Depth(τ^{line})				
				MM1	MM6	MM7/G	MM8/F	MM4/E
Hydrogen Recombination Line								
99.02295	H(40) α	v ^b
99.22520	H(50) β	v
Formaldehyde (H₂CO)								
101.33299	$J(K_a, K_c) = 6(1, 5) - 6(1, 6)$	5.06	88	...	7.46(-1)	1.01(-1)	1.83(-1)	3.25(-1)
Ketene (H₂CCO)								
100.09451	$J(K_a, K_c) = 5(1, 5) - 4(1, 4)$	28.79	27	7.10(-3)	4.23(-2)	7.02(-2)
101.00245	5(3, 3) - 4(3, 2)	19.20	133	5.92(-3)	1.98(-2)	3.33(-2)
101.02447	5(2, 4) - 4(2, 3)	8.40	67	6.42(-3)	b	1.40(-2)
101.03223	5(2, 3) - 4(2, 2)	8.40	67	6.76(-3)	8.26(-3)	1.33(-2)
101.03671	5(0, 5) - 4(0, 4)	10	15	1.81(-2)	1.66(-2)	2.64(-2)
Methanol (CH₃OH v_t = 0)								
97.58279	$J(K_a, K_c) = 2(1, 1) - 1(1, 0)A$	4.85	22	...	2.46(-2)	2.33(-1)	2.09(-1)	3.05(-1)
97.67768	21(6, 16) - 22(5, 17)A	22.90	729	b ^d	2.42(-2)
97.67880	21(6, 15) - 22(5, 18)A	22.90	729	b	2.42(-2)
98.03064	24(6, 19) - 23(7, 16)A	6.4	889	1.33(-2)
98.03068	24(6, 18) - 23(7, 17)A	6.4	889	1.33(-2)
100.63887	13(-2, 12) - 12(-3, 10)E	15	234	8.87(-2)	1.45(-1)	2.63(-1)
101.18545	6(2, 4) - 6(-1, 5)E	0.09	75	b
101.29341	7(2, 5) - 7(-1, 6)E	0.19	91	b	...
(CH₃OH v_t = 1)								
99.37434	$J(K_a, K_c) = 15(6, 10) - 14(7, 8)E$	11.11	771	7.13(-3)
99.73094	6(-1, 6) - 5(-0, 5)E	12.56	340	1.60(-2)	3.62(-2)	6.82(-2)
99.77283	20(-3, 17) - 21(-4, 18)E	70.53	902	8.65(-3)	2.40(-2)
Acetaldehyde (CH₃CHO)								
98.86331	$J(K_a, K_c) = 5(1, 4) - 4(1, 3)E$	60.69	17	1.58(-2)	8.09(-3)	1.22(-2)
98.90094	5(1, 4) - 4(1, 3)A --	60.70	16	1.58(-2)	8.30(-3)	1.21(-2)
Methyl Formate (CH₃OCHO, v=0)								
97.65127	$J(K_a, K_c) = 10(4, 7) - 10(3, 8)E$	2.43	43	b
97.69426	10(4, 7) - 10(3, 8)A	2.45	43	6.52(-3)
98.18233	8(7, 1) - 7(7, 0)E	5	54	1.24(-2)
98.19065	8(7, 2) - 7(7, 1)A	5	54	1.22(-2)	3.25(-2)
98.19065	8(7, 1) - 7(7, 0)A	5	54	1.22(-2)	3.25(-2)
98.19146	8(7, 2) - 7(7, 1)E	5	54	1.22(-2)	3.25(-2)
98.27050	8(6, 2) - 7(6, 1)E	9.3	45	8.87(-3)	2.42(-2)
98.27892	8(6, 3) - 7(6, 2)E	9.3	45	4.49(-3)	2.34(-2)	6.21(-2)
98.27976	8(6, 3) - 7(6, 2)A	9.3	45	4.49(-3)	2.34(-2)	6.21(-2)
98.27976	8(6, 2) - 7(6, 1)A	9.3	45	4.49(-3)	2.34(-2)	6.21(-2)
98.42420	8(5, 3) - 7(5, 2)E	13	38	6.01(-3)	1.30(-2)	3.54(-2)
98.43180	8(5, 4) - 7(5, 3)E	13	38	9.69(-3)	2.18(-2)	5.71(-2)
98.43276	8(5, 4) - 7(5, 3)A	13	38	9.69(-3)	2.18(-2)	5.71(-2)
98.43580	8(5, 3) - 7(5, 2)A	13	38	7.43(-3)	1.32(-2)	3.61(-2)
98.60685	8(3, 6) - 7(3, 5)E	18.24	27	1.05(-2)	2.00(-2)	5.50(-2)
98.61116	8(3, 6) - 7(3, 5)A	18.27	27	b	b	b
98.68261	8(4, 5) - 7(4, 4)A	15.96	32	9.80(-3)	1.62(-2)	4.39(-2)
98.71200	8(4, 5) - 7(4, 4)E	15.43	32	9.22(-3)	b	4.42(-2)
98.74790	8(4, 4) - 7(4, 3)E	15.44	32	9.05(-3)	1.64(-2)	4.50(-2)
98.79228	8(4, 4) - 7(4, 3)A	15.96	32	9.74(-3)	1.70(-2)	4.64(-2)
98.83952	11(4, 8) - 11(3, 9)E	2.74	50	6.92(-3)
98.87522	11(4, 8) - 11(3, 9)A	2.75	50	7.01(-3)
99.13327	9(0, 9) - 8(1, 8)E	3.35	25	3.78(-3)	1.02(-2)
99.13576	9(0, 9) - 8(1, 8)A	3.35	25	3.76(-3)	1.02(-2)
100.07860	9(1, 9) - 8(1, 8)E	23.50	25	b	b	b
100.08054	9(1, 9) - 8(1, 8)A	23.51	25	b	b	3.32(-2)
100.29460	8(3, 5) - 7(3, 4)E	18.25	27	1.95(-2)	5.29(-2)
100.30817	8(3, 5) - 7(3, 4)A	18.28	27	1.98(-2)	5.40(-2)

Table B1: continued.

Rest Frequency (GHz)	Quantum Numbers ^a	$S_{ij}\mu^2$ (Debye ²)	E _u (K)	Line Optical Depth(τ^{line})					
				MM1	MM6	MM7/G	MM8/F	MM4/E	MM11/D
100.48224	8(1,7)–7(1,6) <i>E</i>	20.63	23	1.40(-2)	2.34(-2)	6.43(-2)	3.01(-2)
100.49068	8(1,7)–7(1,6) <i>A</i>	20.63	23	1.41(-2)	2.31(-2)	6.31(-2)	2.92(-2)
100.68154	9(0,9)–8(0,8) <i>E</i>	23.54	25	1.43(-2)	2.89(-2)	7.44(-2)	3.34(-2)
100.68336	9(0,9)–8(0,8) <i>A</i>	23.54	25	1.44(-2)	2.86(-2)	7.64(-2)	3.50(-2)
100.69466	5(3,3)–5(1,4) <i>E</i>	0.04	15	7.20(-3)	...
(CH ₃ OCHO, v=1)									
97.57730	<i>J</i> (<i>K_a, K_c</i>) = 8(5,3)–7(5,2) <i>E</i>	13.00	225	6.87(-3)	1.01(-2)	...
97.59716	8(3,6)–7(3,5) <i>A</i>	18.21	215	9.90(-3)	1.47(-2)	...
97.66140	8(4,5)–7(4,4) <i>A</i>	15.91	220	8.66(-3)	1.29(-2)	...
97.75288	8(4,4)–7(4,3) <i>A</i>	15.91	220	8.70(-3)	b	...
97.88566	8(5,4)–7(5,3) <i>E</i>	12.99	225	9.90(-3)	...
97.89711	8(4,4)–7(4,3) <i>E</i>	16.02	219	b	...
98.17629	8(4,5)–7(4,4) <i>E</i>	15.97	219	b	b	...
98.68242	8(3,6)–7(3,5) <i>E</i>	18.08	215	b	b	...
98.81529	8(3,5)–7(3,4) <i>E</i>	18.22	215	1.55(-2)	...
99.08951	8(3,5)–7(3,4) <i>A</i>	18.22	215	1.51(-2)	...
99.48905	9(1,9)–8(1,8) <i>A</i>	23.42	213	1.30(-2)	1.96(-2)	9.33(-3)
99.57554	8(1,7)–7(1,6) <i>A</i>	20.58	210	1.17(-2)	1.79(-2)	8.46(-3)
99.57741	9(1,9)–8(1,8) <i>E</i>	23.56	212	1.43(-2)	1.73(-2)	8.68(-3)
99.86910	8(1,7)–7(1,6) <i>E</i>	20.67	210	1.15(-2)	1.74(-2)	b
100.13691	9(0,9)–8(0,8) <i>A</i>	23.46	213	2.05(-2)	...
100.22668	9(0,9)–8(0,8) <i>E</i>	23.60	212	1.33(-2)	2.01(-2)	9.28(-3)
Dimethyl ether (CH ₃ OCH ₃)									
97.99062	<i>J</i> (<i>K_a, K_c</i>) = 16(3,14)–15(4,11) <i>AA</i>	38.07	137	7.30(-3)	...
97.99338	16(3,14)–15(4,11) <i>EE</i>	60.92	137	1.22(-2)	...
97.99617	16(3,14)–15(4,11) <i>AE</i>	22.84	137	b	...
99.18316	25(6,19)–24(7,18) <i>EE</i>	90.22	347	4.89(-3)	...
99.32436	4(1,4)–3(0,3) <i>AE</i>	26.18	10	1.48(-2)	4.79(-2)	7.45(-2)	4.19(-2)
99.32521	4(1,4)–3(0,3) <i>EE</i>	69.82	10	1.48(-2)	4.79(-2)	7.45(-2)	4.19(-2)
99.32607	4(1,4)–3(0,3) <i>AA</i>	43.63	10	1.48(-2)	4.79(-2)	7.45(-2)	4.19(-2)
99.83366	14(2,13)–13(3,10) <i>AA</i>	28.85	101	8.03(-3)	...
99.83645	14(2,13)–13(3,10) <i>EE</i>	46.17	101	8.93(-3)	1.32(-2)	6.81(-3)
99.83924	14(2,13)–13(3,10) <i>AE</i>	17.31	101	8.20(-3)	...
100.43416	22(5,18)–21(6,15) <i>AA</i>	50.94	266	b	...
100.43546	22(5,18)–21(6,15) <i>EE</i>	81.42	266	b	...
100.46043	6(2,5)–6(1,6) <i>AE</i>	28.84	25	b	1.61(-2)	2.85(-2)	1.58(-2)
100.46307	6(2,5)–6(1,6) <i>EE</i>	76.92	25	b	b	b	2.55(-2)
100.46572	6(2,5)–6(1,6) <i>AA</i>	48.07	25	b	b	b	1.54(-2)
100.94683	19(4,16)–18(5,13) <i>AA</i>	26.95	196
100.94900	19(4,16)–18(5,13) <i>EE</i>	71.88	196	6.03(-3)	8.49(-3)	...
100.95109	19(4,16)–18(5,13) <i>EA</i>	17.96	196
Acetone (CH ₃ COCH ₃)									
98.05239	<i>J</i> (<i>K_a, K_c</i>) = 17(6,11)–17(5,12) <i>EE</i>	872	111	b	8.25(-3)	...
98.05353	17(7,11)–17(6,12) <i>EE</i>	872	111	b	8.25(-3)	...
98.60072	16(5,11)–16(4,12) <i>EE</i>	736	96	b	1.30(-2)	...
98.60097	16(6,11)–16(5,12) <i>EE</i>	736	96	b	1.30(-2)	...
98.65151	5(5,1)–4(4,1) <i>EE</i>	496	14	b	8.96(-3)	...
98.73857	16(5,11)–16(4,12) <i>AA</i>	276	96	b	6.42(-3)	...
98.73883	16(6,11)–16(5,12) <i>AA</i>	461	96	b	6.42(-3)	...
98.80089	5(5,0)–4(4,0) <i>EE</i>	498	14	6.40(-3)	9.39(-3)	...
99.05250	15(4,11)–15(3,12) <i>EE</i>	598	81	9.17(-3)	1.18(-2)	...
99.05255	15(5,11)–15(4,12) <i>EE</i>	598	81	9.17(-3)	1.18(-2)	...
100.35030	8(2,6)–7(3,5) <i>EE</i>	694	25	8.60(-3)	1.21(-2)	...
100.50706	8(3,6)–7(2,5) <i>AA</i>	434	25	5.07(-3)	7.14(-3)	...
gauche-Ethanol (g-C ₂ H ₅ OH)									
97.53590	<i>J</i> (<i>K_a, K_c</i>) = 21(1,21)–21(0,21), <i>vt</i> = 1–0	26.06	246	9.23(-3)	1.49(-2)	3.73(-2)	...
97.53684	23(1,23)–23(0,23), <i>vt</i> = 1–0	28.49	282	9.36(-3)	1.17(-2)	3.55(-2)	...

Table B1: continued.

Rest Frequency (GHz)	Quantum Numbers ^a	$S_{ij}\mu^2$ (Debye ²)	E _u (K)	Line Optical Depth(τ^{line})					
				MM1	MM6	MM7/G	MM8/F	MM4/E	MM11/D
97.54687	29(1,28)–29(2,28), $vt = 1 - 0$	17.84	420	7.12(-3)	...
97.54969	26(0,26)–26(1,26), $vt = 1 - 0$	32.12	341	5.99(-3)	1.54(-2)	...
97.56281	24(1,24)–24(0,24), $vt = 1 - 0$	29.69	301	1.86(-2)	...
97.57400	20(1,20)–20(0,20), $vt = 1 - 0$	24.85	230	7.92(-3)	1.05(-2)	2.66(-2)	...
97.60039	25(1,25)–25(0,25), $vt = 1 - 0$	30.91	320	1.64(-2)	...
97.63132	27(0,27)–27(1,27), $vt = 1 - 0$	33.34	362	1.34(-2)	...
97.64950	19(1,19)–19(0,19), $vt = 1 - 0$	23.64	214	8.56(-3)	1.11(-2)	2.81(-2)	...
97.69853	27(1,27)–27(0,27), $vt = 1 - 0$	33.33	362	1.33(-2)	...
97.70888	28(0,28)–28(1,28), $vt = 1 - 0$	34.54	384	1.16(-2)	...
97.75561	28(1,28)–28(0,28), $vt = 1 - 0$	34.55	384	1.19(-2)	...
97.77430	18(1,18)–18(0,18), $vt = 1 - 0$	22.42	199	b	1.14(-2)	2.96(-2)	...
97.78411	29(0,29)–29(1,29), $vt = 1 - 0$	35.76	407	1.03(-2)	...
97.81598	29(1,29)–29(0,29), $vt = 1 - 0$	35.76	407	9.88(-3)	...
97.82895	30(1,29)–30(2,29), $vt = 1 - 0$	18.45	444	6.19(-3)	...
97.85747	30(0,30)–30(1,30), $vt = 1 - 0$	36.98	430	8.22(-3)	...
97.87745	51(4,48)–51(3,48), $vt = 1 - 0$	36.98	430	8.21(-3)	...
97.96283	17(1,17)–17(0,17), $vt = 1 - 0$	21.21	185	1.10(-2)	1.20(-2)	3.06(-2)	...
98.23031	16(1,16)–16(0,16), $vt = 1 - 0$	20	171	1.18(-2)	1.22(-2)	3.19(-2)	8.52(-3)
98.58509	15(1,15)–15(0,15), $vt = 1 - 0$	18.79	158	1.16(-2)	1.25(-2)	3.30(-2)	...
98.82369	29(2,28)–29(1,28), $vt = 1 - 0$	17.84	420	7.62(-3)	...
98.87828	13(1,13)–13(0,13), $vt = 1 - 0$	16.37	135	1.87(-2)	...
98.94626	28(2,27)–28(1,27), $vt = 1 - 0$	17.23	397	8.86(-3)	...
98.98354	14(1,14)–14(0,14), $vt = 1 - 0$	17.58	147	1.19(-2)	1.22(-2)	3.19(-2)	...
99.86441	25(2,24)–25(1,24), $vt = 1 - 0$	15.41	332	1.19(-2)	...
100.19432	6(1,6)–5(1,5), $vt = 0 - 0$	9.32	75	6.83(-3)	1.93(-2)
100.36505	6(1,6)–5(1,5), $vt = 1 - 1$	9.32	80	6.08(-3)	2.07(-2)
100.45207	24(2,23)–24(1,23), $vt = 1 - 0$	14.80	312	1.31(-2)	...
101.24363	23(2,22)–23(1,22), $vt = 1 - 0$	14.19	292	1.46(-2)	...
trans-Ethanol (t-C ₂ H ₅ OH)									
99.52409	$J(K_a, K_c) = 17(3,14) - 17(2,15)$	18.34	141	1.35(-2)	1.37(-2)	3.58(-2)	1.04(-2)
99.97588	18(3,15)–18(2,16)	19.42	157	1.30(-2)	1.28(-2)	3.41(-2)	...
100.35895	16(3,13)–16(2,14)	25.70	127	1.50(-2)	1.39(-2)	3.56(-2)	...
100.99010	8(2,7)–8(1,8)	8.83	35	1.00(-2)	7.55(-3)	2.09(-2)	...
Cyanoacetylene (HC ₃ N, v=0)									
100.07638	$J = 11 - 10$	152.56	29	4.87(-2)	2.44(-1)	2.69(-1)	2.53(-1)	2.50(-1)	2.23(-1)
		(HC ¹³ CN, v=0)							
99.65184	$J = 11 - 10, F = 11 - 10$	153.19	29	4.58(-2)	5.25(-2)	5.53(-2)	8.44(-3)
		(HCC ¹³ CN, v=0)							
99.66146	$J = 11 - 10, F = 11 - 10$	153.19	29	4.41(-2)	3.95(-2)	4.60(-2)	6.66(-3)
		(HC ₃ N, v7=1)							
100.32241	$J = 11 - 10, l = 1e$	151.18	350	4.90(-2)	1.43(-1)	1.00(-1)	5.94(-3)
100.46617	$J = 11 - 10, l = 1f$	151.15	350	4.86(-2)	1.44(-1)	9.79(-2)	b
		(HC ₃ N, v7=2)							
100.70878	$J = 11 - 10, l = 0$	151.73	671	9.46(-3)	4.28(-2)	9.01(-3)	...
100.71106	$J = 11 - 10, l = 2e$	146.72	674	9.37(-3)	4.16(-2)	8.52(-3)	...
100.71439	$J = 11 - 10, l = 2f$	146.71	674	7.65(-3)	3.19(-2)	8.28(-3)	...
		(HC ₃ N, v7=3)							
100.88044	$J = 11 - 10, l = 1e$	150.48	985	b
101.02780	$J = 11 - 10, l = 3$	140.45	991	b
101.16989	$J = 11 - 10, l = 1f$	150.48	985	b
		(HC ₃ N, v6=1)							
100.24058	$J = 11 - 10, l = 1e$	151.48	747	1.74(-2)
100.31938	$J = 11 - 10, l = 1f$	151.46	747	b	b	b	...
		(HC ¹³ CN, v7=1)							
99.88792	$J = 11 - 10, l = 1e$	151.17	345	1.06(-2)
100.03251	$J = 11 - 10, l = 1f$	151.17	345	b
		(HCC ¹³ CN, v7=1)							

Table B1: continued.

Rest Frequency (GHz)	Quantum Numbers ^a	$S_{ij}\mu^2$ (Debye ²)	E _u (K)	Line Optical Depth(τ^{line})					
				MM1	MM6	MM7/G	MM8/F	MM4/E	MM11/D
99.90177	$J = 11 - 10, l = 1e$	151.17	347	b
100.04531	$J = 11 - 10, l = 1f$	151.17	347	1.02(-2)
Cyanodiacetylene ($\text{HC}_5\text{N}, v=0$)									
98.51252	$J = 37 - 36$	2080.91	90	3.03(-2)	1.86(-2)	3.36(-2)	b
101.17467	$J = 38 - 37$	2137.61	95	3.10(-2)	1.85(-2)	3.52(-2)	...
Ethyl Cyanide ($\text{CH}_3\text{CH}_2\text{CN}$)									
97.84469	$J(K_a, K_c) = 19(3, 16) - 19(2, 17)$	18.91	92	b
97.87509	34(4, 31) - 33(5, 28)	8.22	274
98.17757	11(2, 10) - 10(2, 9)	157.60	33	4.19(-2)	2.09(-1)	4.61(-2)	...
98.52387	11(6, 5) - 10(6, 4)	114.54	68	7.25(-2)	3.79(-1)	7.75(-2)	...
98.52467	11(7, 4) - 10(7, 3)	97.02	83	6.57(-2)	3.71(-1)	5.80(-2)	...
98.53208	11(8, 3) - 10(8, 2)	76.81	99	6.00(-2)	3.03(-1)	5.74(-2)	...
98.53398	11(5, 6) - 10(5, 5)	129.36	56	5.78(-2)	3.11(-1)	6.59(-2)	...
98.54416	11(9, 2) - 10(9, 1)	53.90	118	1.37(-2)	b	1.59(-2)	...
98.55992	11(10, 1) - 10(10, 0)	28.30	139	b	b
98.56679	11(4, 7) - 10(4, 6)	141.49	46	4.08(-2)	2.07(-1)	3.95(-2)	...
98.61009	11(3, 9) - 10(3, 8)	150.93	38	3.84(-2)	1.93(-1)	b	...
98.70110	11(3, 8) - 10(3, 7)	150.93	38	3.85(-2)	1.93(-1)	4.19(-2)	...
99.07060	32(3, 29) - 32(2, 30)	37.29	240	b	b
99.25344	15(2, 14) - 15(1, 15)	8.83	56	b	b
99.68146	11(2, 9) - 10(2, 8)	157.63	33	b	2.12(-1)	4.86(-2)	...
100.03442	18(3, 15) - 18(2, 16)	17.34	84	b
100.61428	11(1, 10) - 10(1, 9)	161.58	30	4.13(-2)	2.18(-1)	5.16(-2)	...
101.09167	10(1, 10) - 9(0, 9)	9.77	24	b	b
$(\text{CH}_3\text{CH}_2)^{13}\text{CN}$									
97.69154	$J(K_a, K_c) = 11(2, 10) - 10(2, 9)$	154.84	33	b
98.03285	11(6, 6) - 10(6, 5)	112.51	68	1.69(-2)
98.03285	11(6, 5) - 10(6, 4)	112.51	68	1.69(-2)
98.04150	11(8, 4) - 10(8, 3)	75	99	1.84(-2)
98.04150	11(8, 3) - 10(8, 2)	75	99	1.84(-2)
98.05374	11(9, 3) - 10(9, 2)	52.96	118	b
98.07271	11(4, 8) - 10(4, 7)	138.99	46	9.25(-3)
98.07461	11(4, 7) - 10(4, 6)	139.02	46	9.59(-3)
98.11741	11(3, 9) - 10(3, 8)	148.26	38	1.04(-2)
98.20621	11(3, 8) - 10(3, 7)	148.27	38	1.01(-2)
99.17252	11(2, 9) - 10(2, 8)	154.88	33	1.16(-2)
100.10973	11(1, 10) - 10(1, 9)	158.73	40	1.11(-2)
$(\text{CH}_3)^{13}\text{CH}_2\text{CN}$									
97.67201	$J(K_a, K_c) = 11(2, 10) - 10(2, 9)$	154.84	33	1.13(-2)
98.03964	11(7, 5) - 10(7, 4)	95.31	81	1.77(-2)
98.04058	11(6, 6) - 10(6, 5)	112.52	67	1.74(-2)
98.04556	11(8, 4) - 10(8, 3)	75.45	98
98.05296	11(5, 6) - 10(5, 5)	127.09	55	1.58(-2)
98.08734	11(4, 8) - 10(4, 7)	139	46	9.14(-3)
98.08968	11(4, 7) - 10(4, 6)	138.99	46	9.06(-3)
98.13485	11(3, 9) - 10(3, 8)	148.26	38	1.02(-2)
98.23779	11(3, 8) - 10(3, 7)	148.26	38	b
99.27963	11(2, 9) - 10(2, 8)	154.89	33	1.13(-2)
100.15582	11(1, 10) - 10(1, 9)	158.73	30	1.15(-2)
$(^{13}\text{CH}_3\text{CH}_2\text{CN})$									
98.16534	$J(K_a, K_c) = 11(1, 10) - 10(1, 9)$	158.73	29	1.17(-2)
$(\text{C}_2\text{H}_5\text{C}^{15}\text{N})$									
97.72519	$J(K_a, K_c) = 11(1, 10) - 10(1, 9)$	161.60	29	✓	...
101.17615	12(1, 12) - 11(1, 11)	175.64	33	b	b	...
Ammonia (NH_2D)									
99.11881	$J(K_a, K_c) = 5(2, 4)0a - 5(1, 4)0s$	87	261	4.24(-2)	3.24(-2)	9.76(-3)

Table B1: continued.

Rest Frequency (GHz)	Quantum Numbers ^a	$S_{ij}\mu^2$ (Debye ²)	E _u (K)	Line Optical Depth(τ^{line})					
				MM1	MM6	MM7/G	MM8/F	MM4/E	MM11/D
Carbon Monosulfide (CS)									
97.98095	$J = 2 - 1$	8	7	2.33(-1)	4.62(-1)	1.32(0)	1.17(0)	3.28(-1)	6.55(-1)
Sulfur Monoxide (SO)									
99.29987	$J(N) = 3(2) - 2(1)$	6.91	9	5.06(-2)	1.05(-1)	4.12(-1)	4.51(-1)	3.55(-1)	1.94(-1)
100.02964	$4(5) - 4(4)$	0.84	39	3.79(-2)	4.11(-2)	2.89(-2)	1.72(-2)
(^{34}SO)									
97.71532	$J(N) = 3(2) - 2(1)$	6.91	9	...	1.12(-2)	3.81(-2)	6.35(-2)	4.46(-2)	1.26(-2)
Sulfur dioxide (SO_2, v=0)									
97.70233	$J(K_a, K_c) = 7(3, 5) - 8(2, 6)$	2.51	48	3.76(-2)	3.06(-2)	5.12(-2)	...
100.87810	$2(2, 0) - 3(1, 3)$	0.43	13	b	1.20(-2)	...
$(^{33}\text{SO}_2, v=0)$									
98.25793	$J(K_a, K_c) = 2(2, 0) - 3(1, 3), F = 7/2 - 7/2$	0.07	13	1.63(-2)
98.25810	$2(2, 0) - 3(1, 3), F = 5/2 - 7/2$	0.41	13	1.63(-2)
98.26062	$2(2, 0) - 3(1, 3), F = 3/2 - 5/2$	0.27	13
98.26089	$2(2, 0) - 3(1, 3), F = 5/2 - 5/2$	0.09	13
98.26380	$2(2, 0) - 3(1, 3), F = 7/2 - 9/2$	0.60	13	b
98.26623	$2(2, 0) - 3(1, 3), F = 1/2 - 3/2$	0.17	13	b
$(\text{SO}_2, v2=1)$									
98.26469	$J(K_a, K_c) = 16(2, 14) - 15(3, 13)$	8.20	900	2.35(-2)	5.60(-3)	...
99.17739	$27(3, 25) - 26(4, 22)$	8.74	1136
Methyl Mercaptan (CH_3SH)									
100.11021	$J(K_a, K_c) = 4(1, 3) - 3(1, 2)A$	6.23	17	b
101.02974	$4(-1, 4) - 3(-1, 3)E$	6.22	17	b
101.13915	$4(0, 4) - 3(0, 3)A$	6.64	12	1.21(-2)
101.13965	$4(0, 4) - 3(0, 3)E$	6.64	14	1.21(-2)
101.15687	$4(3, 1) - 3(3, 0)E$	2.91	51
101.15932	$4(-2, 3) - 3(-2, 2)A$	4.98	31	8.79(-3)
101.15999	$4(-3, 2) - 3(-3, 1)E$	2.91	52	8.79(-3)
101.16065	$4(3, 1) - 3(3, 0)A$	2.91	53	8.27(-3)
101.16069	$4(-3, 2) - 3(-3, 1)A$	2.91	53	8.27(-3)
101.16715	$4(-2, 3) - 3(-2, 2)E$	4.98	30	b
101.16830	$4(2, 2) - 3(2, 1)E$	4.98	30	b
101.17981	$4(2, 2) - 3(2, 1)A$	4.98	31
101.28436	$4(1, 3) - 3(1, 2)E$	6.22	18	5.71(-3)

For the line optical depth, X(Y) means $X \times 10^Y$.

^a Quantum numbers of the upper and lower levels. For each species, the levels are labelled at the first transition. A and E refer to symmetry state.

^b "✓" indicates that the transition of $\text{H}(40)_\alpha$ is detected.

^c "..." indicates that the transition is not detected, or the line intensity of transition is below 3σ .

^d "b" indicates that the transition is blended with other molecules.

**APPENDIX C: LINE SPECTRA AT EIGHT DENSE CORES
OF G9.62+0.19.**

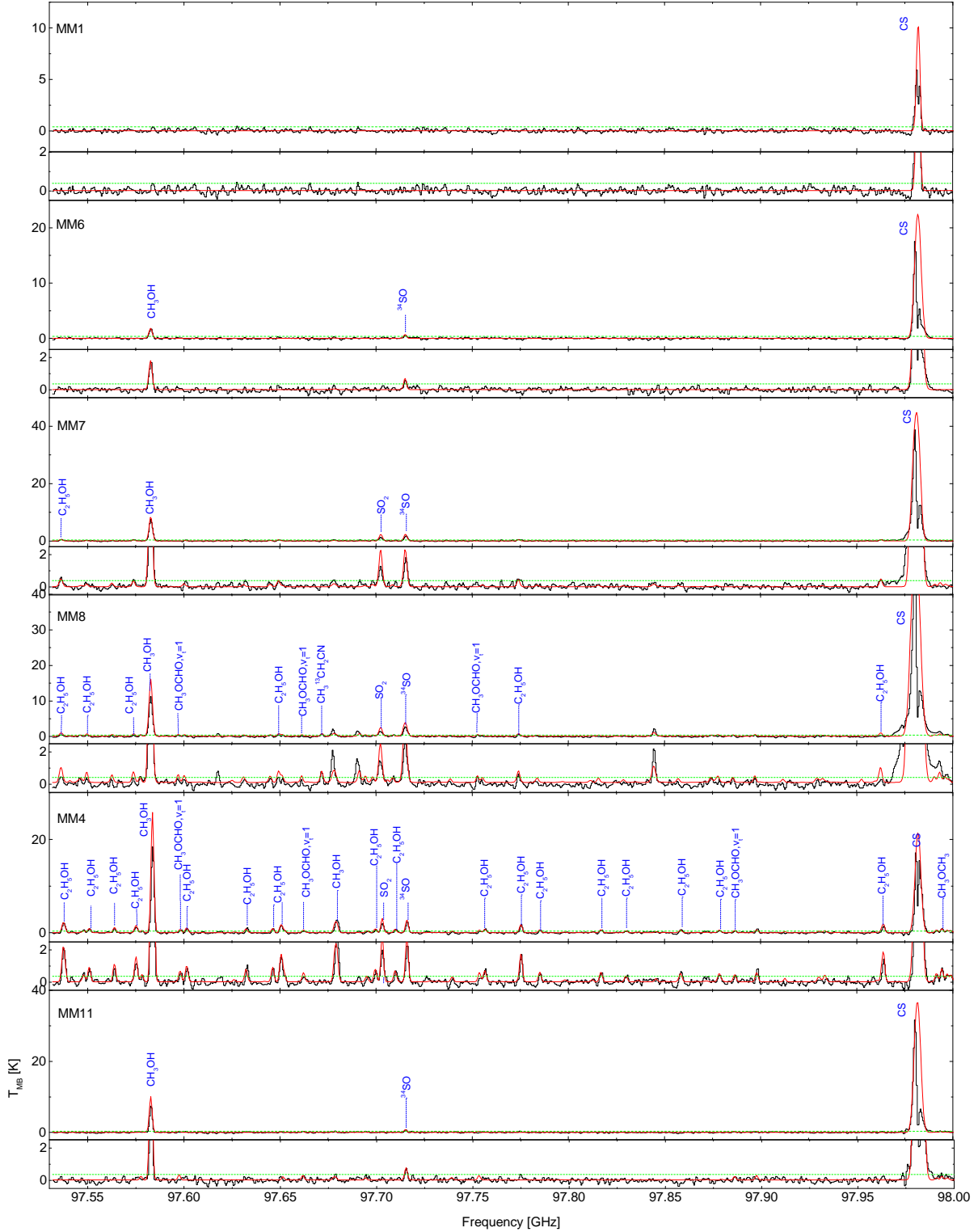


Figure B1. Same as Figure 4, but for frequency range from 97.53 to 98.00 GHz. The black curves are the observed spectra, and the red curves indicate the simulated LTE spectra. The horizontal green dashed line indicates the 3σ noise level in each core.

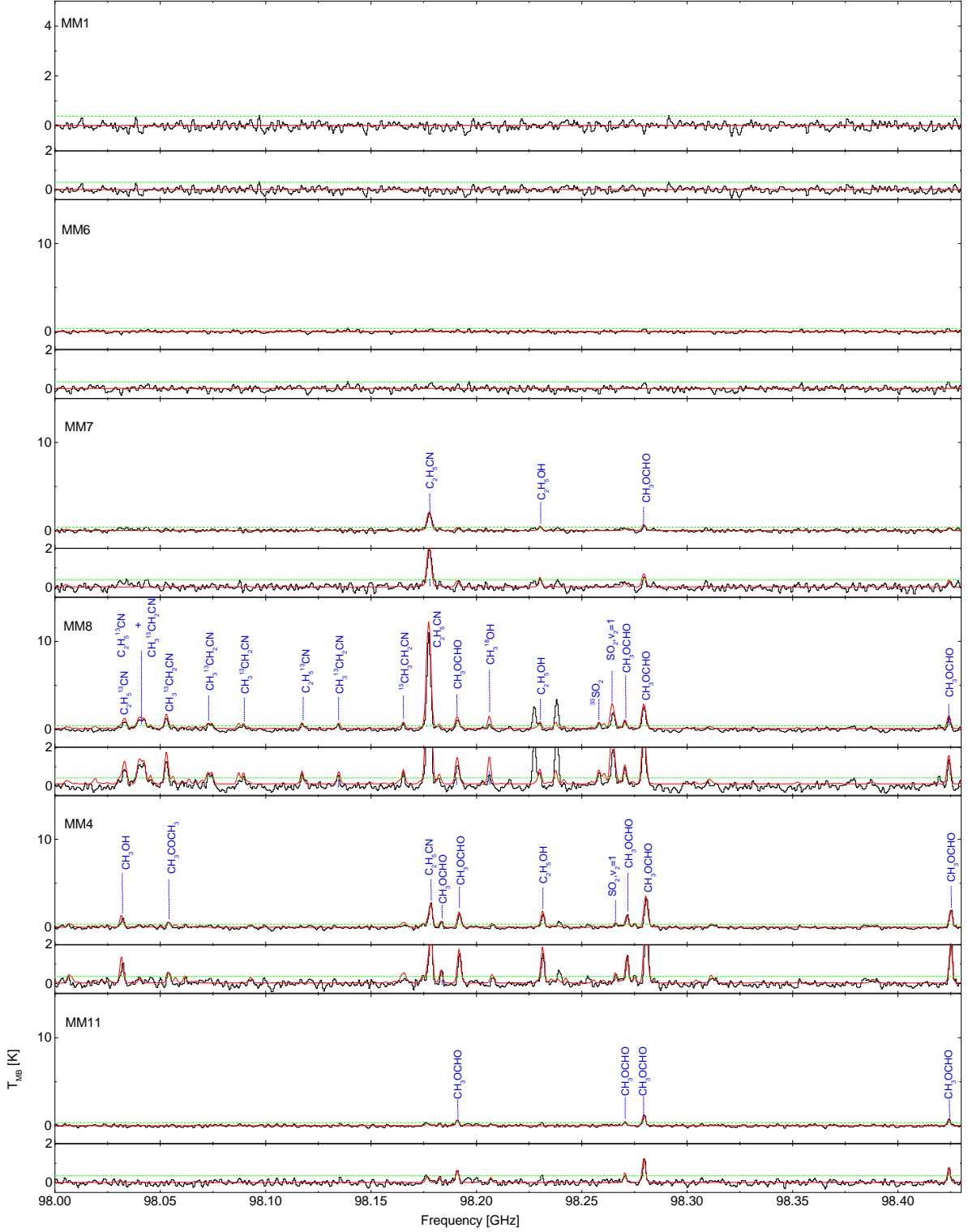


Figure B1. Continued. Frequency range from 98.00 to 98.43 GHz.

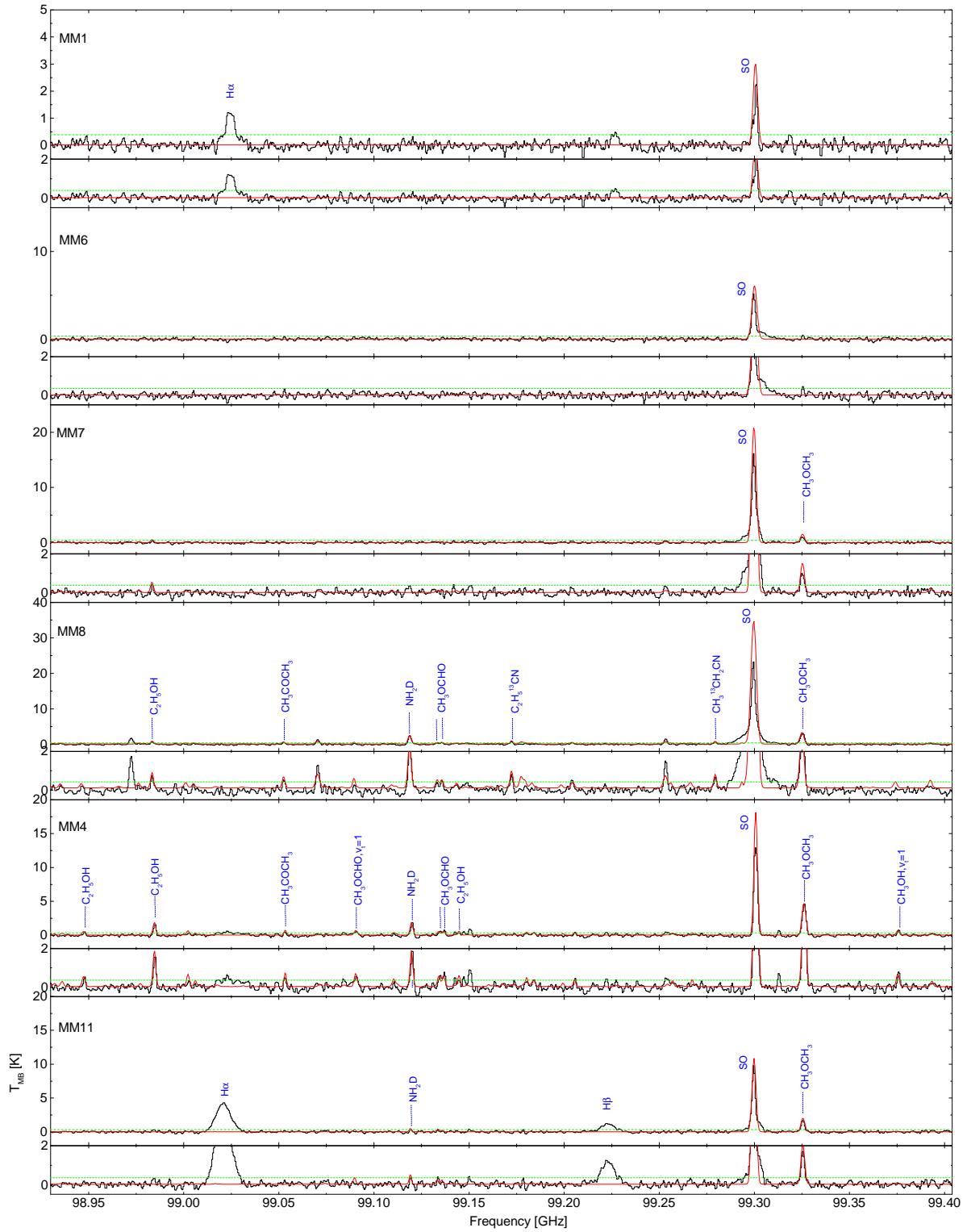
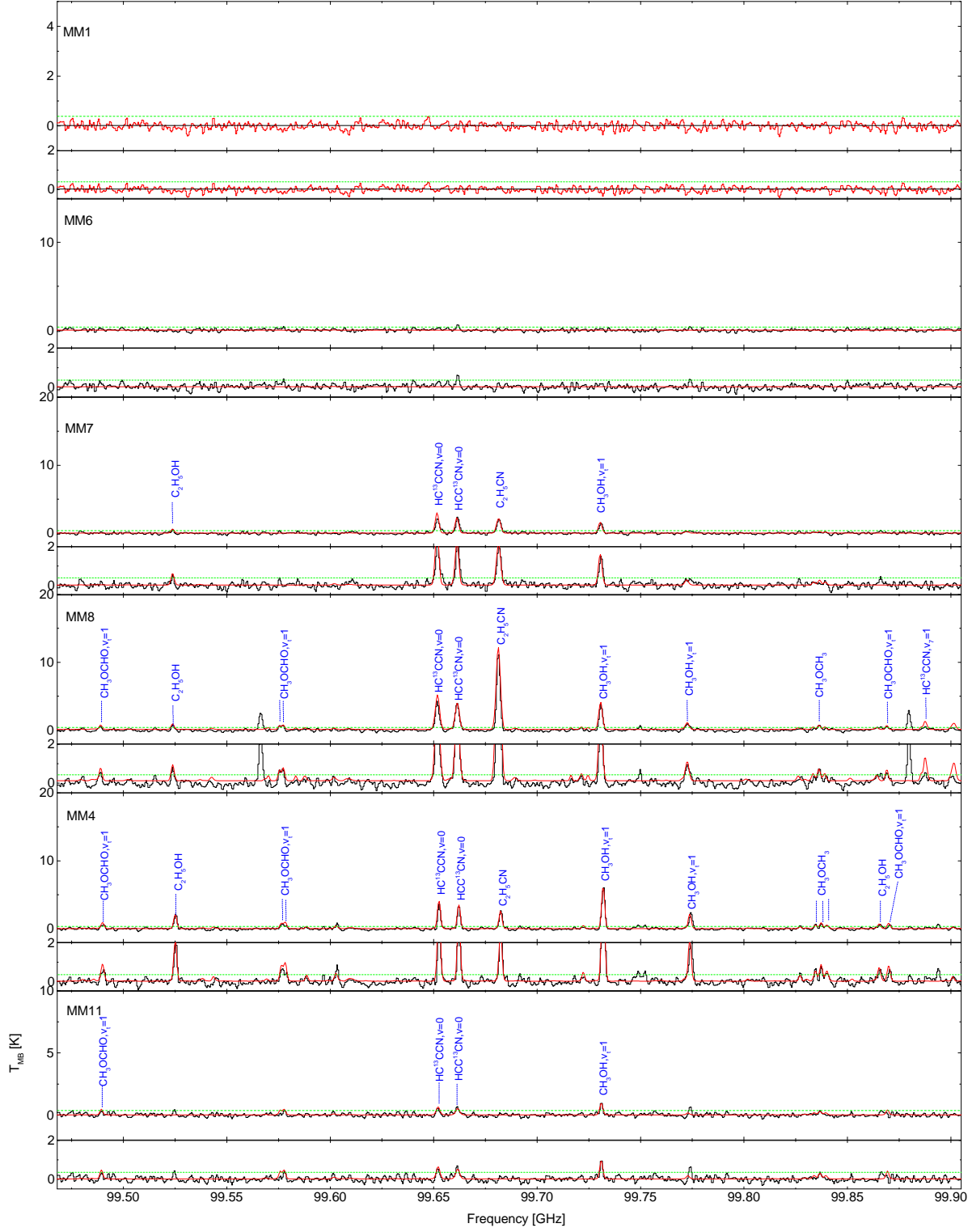


Figure B1. Continued. Frequency range from 98.93 to 99.404 GHz.

**Figure B1.** Continued. Frequency range from 99.458 to 99.905 GHz.

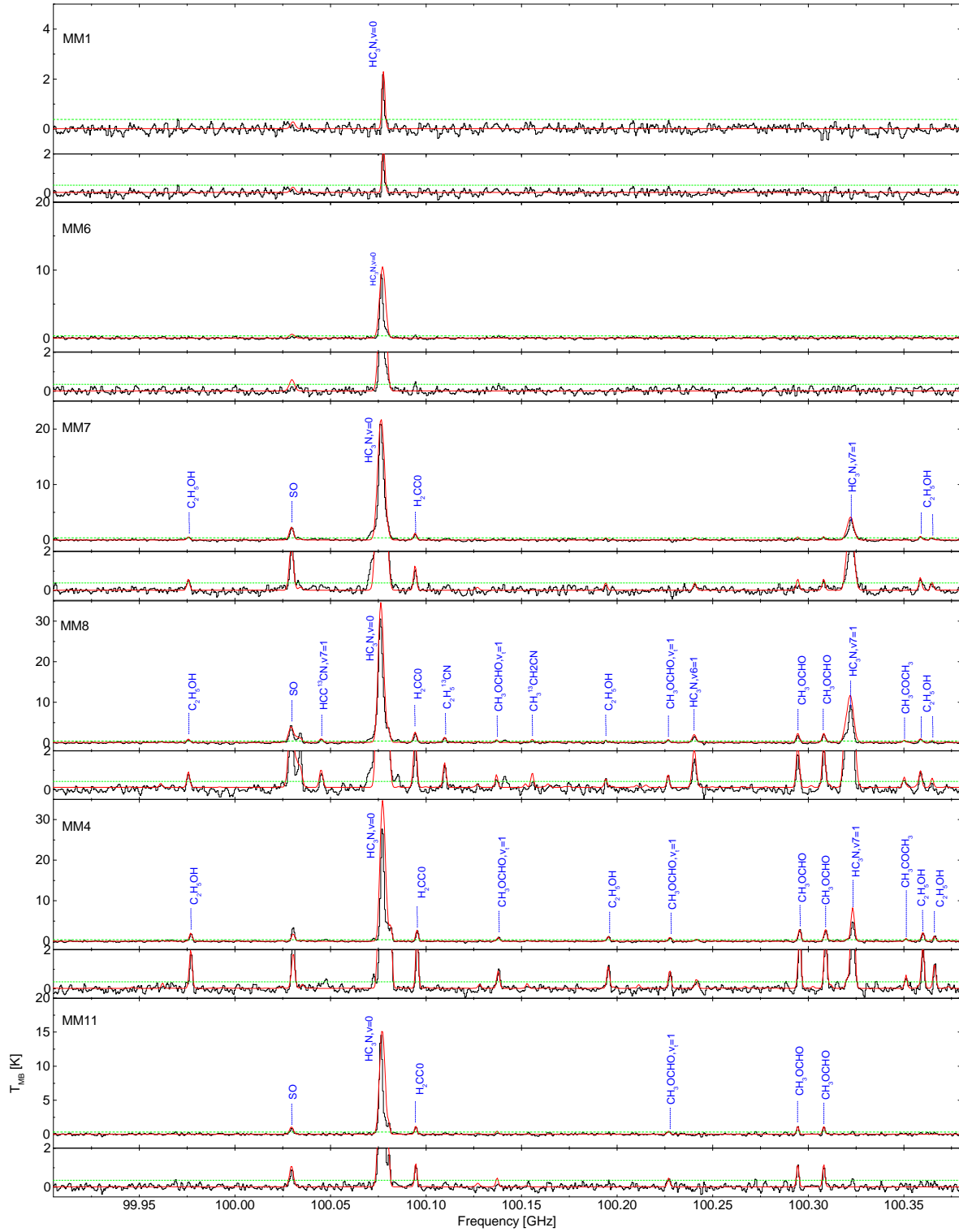
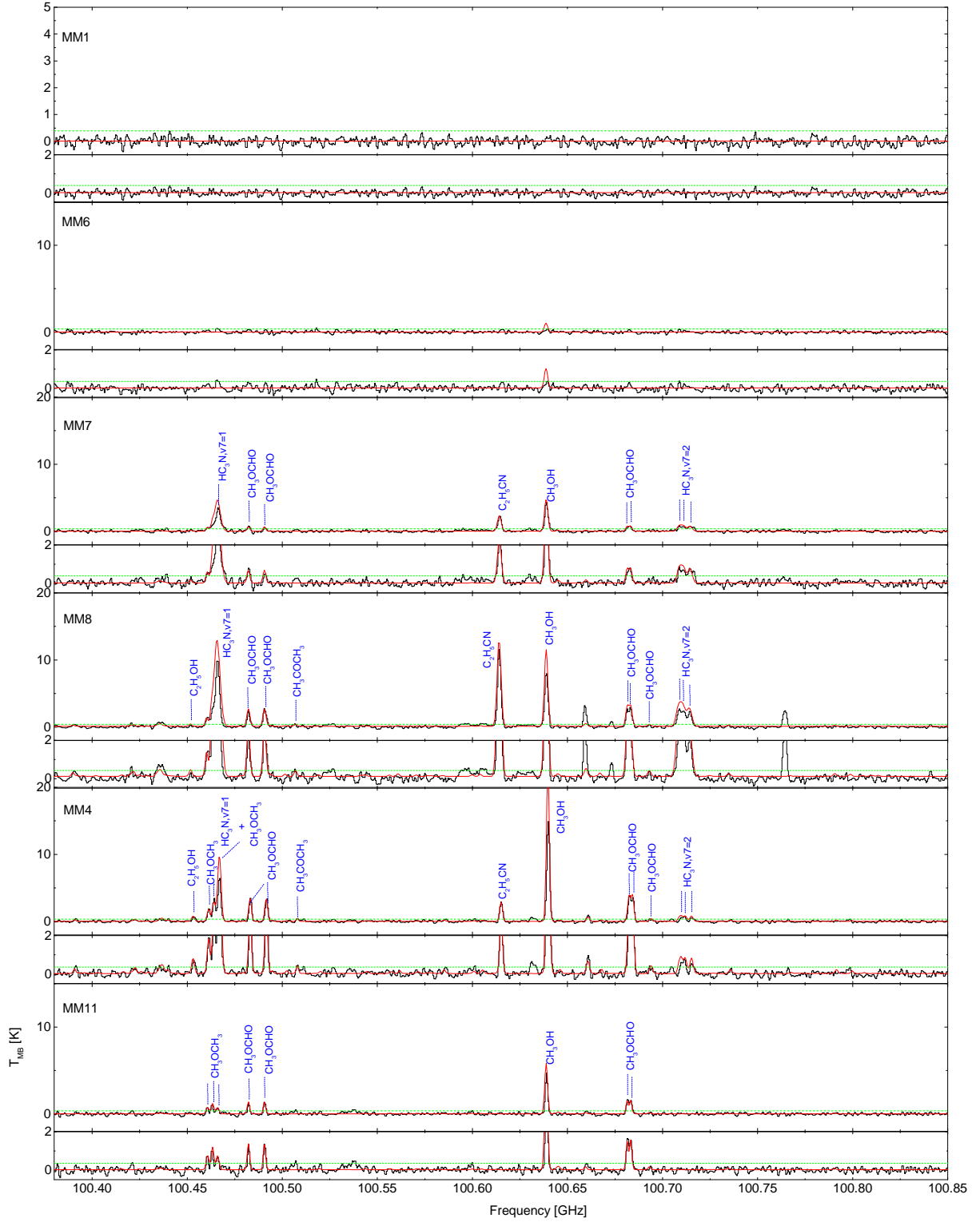


Figure B1. Continued. Frequency range from 99.905 to 100.38 GHz.

**Figure B1.** Continued. Frequency range from 100.38 to 100.85 GHz.

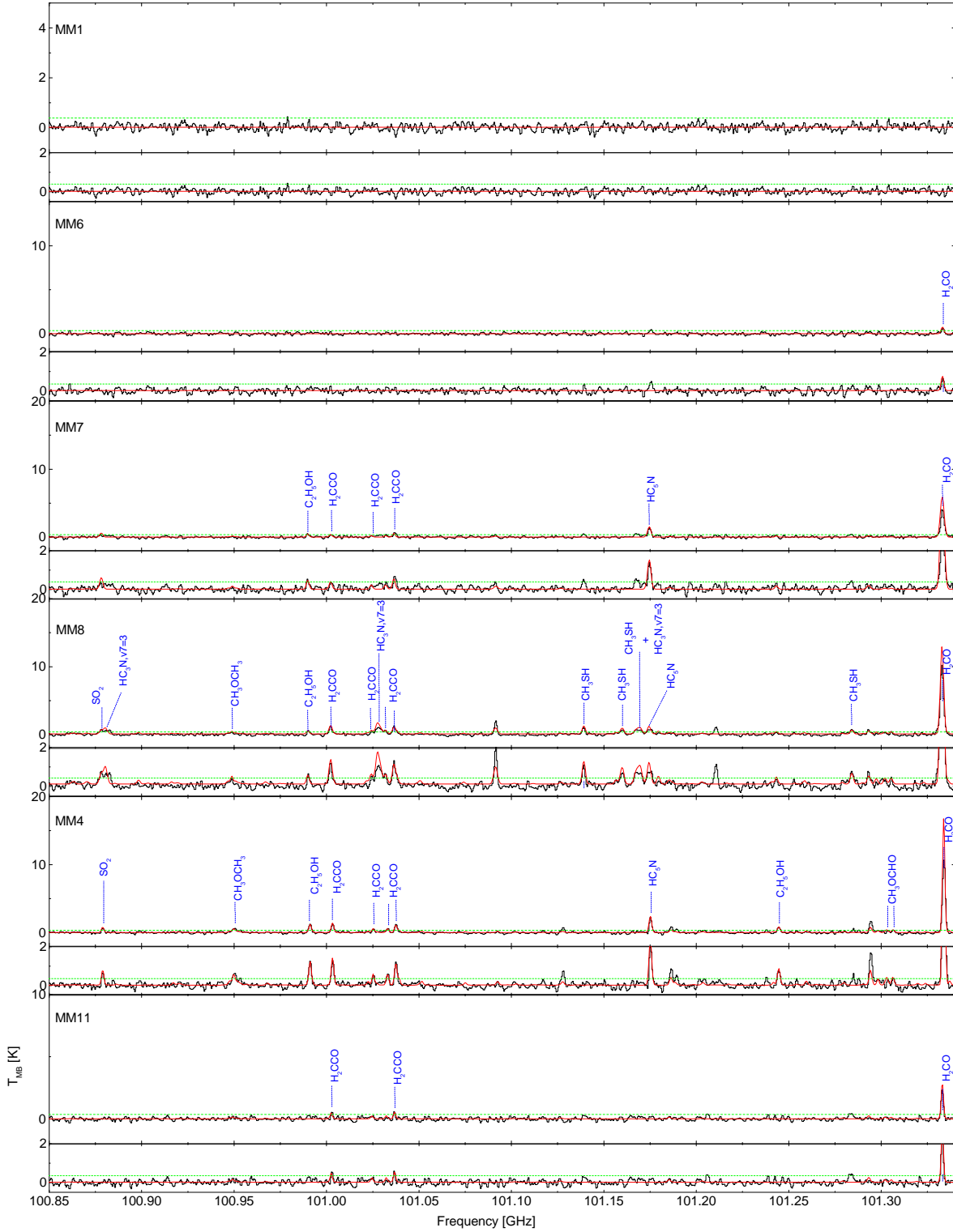


Figure B1. Continued. Frequency range from 100.85 to 101.34 GHz.

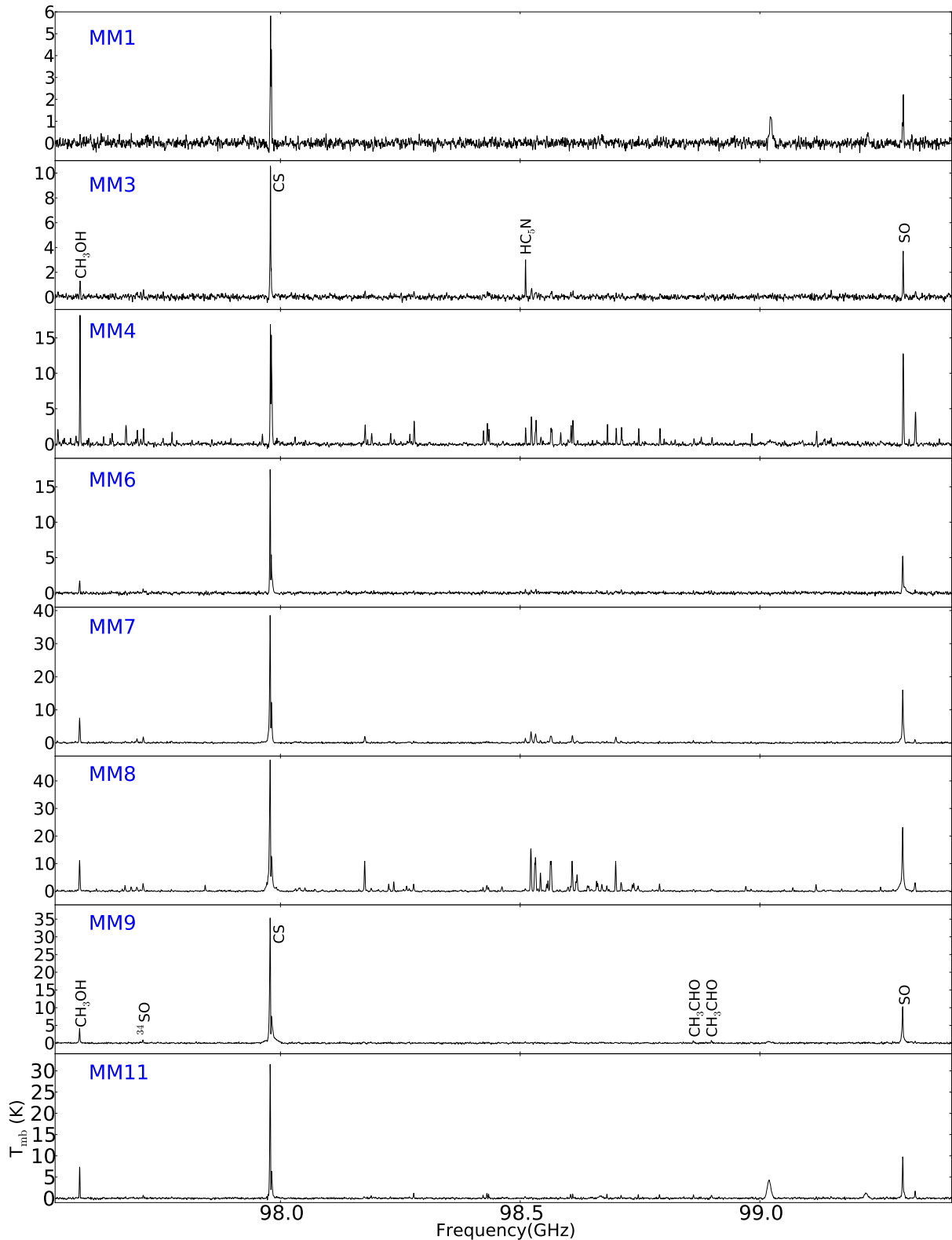


Figure C1. Beam-averaged spectra toward the MM1, MM3, MM4, MM6, MM7, MM8, MM9, and MM11. This segment covers frequency range from 97.53 to 99.40 GHz.

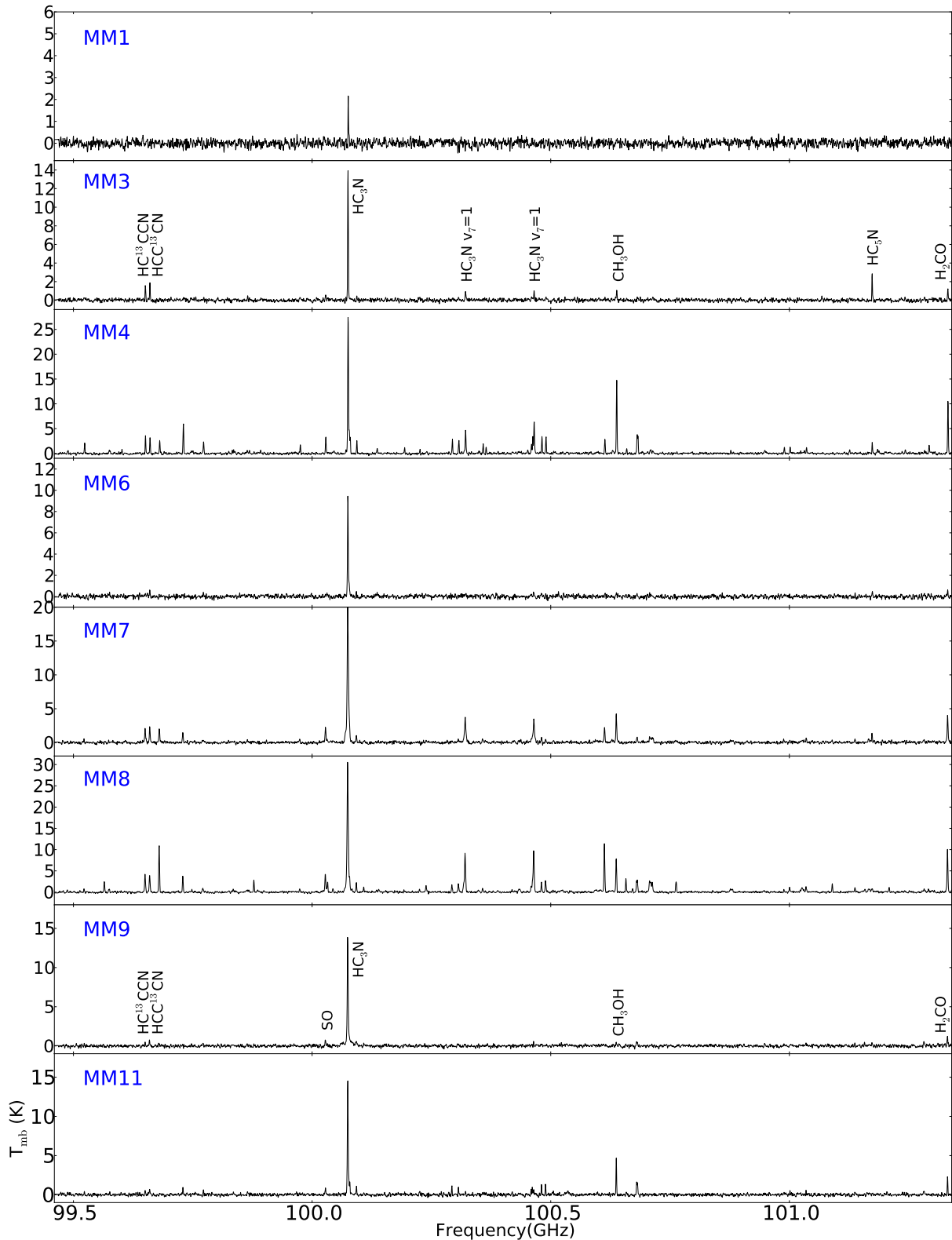


Figure C1. Continued. This segment covers frequency range from 99.46 to 101.34 GHz.

Author affiliations:

- ¹ College of Science, Yunnan Agricultural University, Kunming 650201, People's Republic of China
- ² Department of Astronomy, and Key Laboratory of Astroparticle Physics of Yunnan Province, Yunnan University, Kunming 650091, People's Republic of China
- ³ Shanghai Astronomical Observatory, Chinese Academy of Sciences, 80 Nandan Road, Shanghai 200030, People's Republic of China
- ⁴ S. N. Bose National Centre for Basic Sciences, Block-JD, Sector-III, Salt Lake, Kolkata 700106, India
- ⁵ Kavli Institute for Astronomy and Astrophysics, Peking University, 5 Yiheyuan Road, Haidian District, Beijing 100871, People's Republic of China
- ⁶ Departamento de Astronomía, Universidad de Chile, Las Condes, 7591245 Santiago, Chile
- ⁷ Institute of Astronomy and Astrophysics, Anqing Normal University, Anqing 246133, People's Republic of China
- ⁸ National Astronomical Observatories, Chinese Academy of Sciences, Beijing 100101, China
- ⁹ Korea Astronomy and Space Science Institute, 776 Daedeokdaero, Yuseong-gu, Daejeon 34055, Republic of Korea
- ¹⁰ University of Science and Technology, Korea (UST), 217 Gajeong-ro, Yuseong-gu, Daejeon 34113, Republic of Korea
- ¹¹ Department of Physics, University of Helsinki, PO Box 64, FI-00014 Helsinki, Finland
- ¹² Xinjiang Astronomical Observatory, Chinese Academy of Sciences, 830011 Urumqi, People's Republic of China
- ¹³ Nobeyama Radio Observatory, National Astronomical Observatory of Japan, National Institutes of Natural Sciences, 462-2 Nobeyama, Minamimaki, Minamisaku, Nagano 384-1305, Japan
- ¹⁴ School of Space Research, Kyung Hee University, Yongin-Si, Gyeonggi-Do 17104, Republic of Korea
- ¹⁵ School of Astronomy and Space Science, Nanjing University, Nanjing 210093, People's Republic of China
- ¹⁶ Physical Research Laboratory, Navrangpura, Ahmedabad 380009, India
- ¹⁷ Department of Astronomy, Peking University, 100871 Beijing, People's Republic of China
- ¹⁸ Chinese Academy of Sciences South America Center for Astronomy, National Astronomical Observatories, Chinese Academy of Sciences, Beijing 100012, China
- ¹⁹ Institute of Astrophysics, School of Physics and Electronical Science, Chuxiong Normal University, Chuxiong 675000, China
- ²⁰ School of Physics and Astronomy, Sun Yat-sen University, 2 Daxue Road, Zhuhai, Guangdong 519082, China
- ²¹ CSST Science Center for the Guangdong-Hongkong-Macau Greater Bay Area, Sun Yat-Sen University, Guangdong Province, China
- ²² Laboratory for Space Research, The University of Hong Kong, Hong Kong, China
- ²³ Purple Mountain Observatory and Key Laboratory of Radio Astronomy, Chinese Academy of Sciences, 10 Yuanhua Road, 210023 Nanjing, PR China

This paper has been typeset from a $\text{\TeX}/\text{\LaTeX}$ file prepared by the author.